

# An improved understanding of the roles of atomic processes and power balance in divertor target ion current loss during detachment

K. Verhaegh<sup>1,2</sup>, B. Lipschultz<sup>1</sup>, B.P. Duval<sup>2</sup>, O. Février<sup>2</sup>, A. Fil<sup>1,3</sup>, C. Theiler<sup>2</sup>, M. Wensing<sup>2</sup>, C. Bowman<sup>1,3</sup>, D.S. Gahle<sup>4,3</sup>, J.R. Harrison<sup>3</sup>, B. Labit<sup>2</sup>, C. Marini<sup>2</sup>, R. Maurizio<sup>2</sup>, H. de Oliveira<sup>2</sup>, H. Reimerdes<sup>2</sup>, U. Sheikh<sup>2</sup>, C.K. Tsui<sup>5,2</sup>, N. Vianello<sup>6</sup>, W.A.J. Vijvers<sup>7</sup>, the TCV team<sup>8</sup> and the EUROfusion MST1 team<sup>9</sup>

<sup>1</sup> York Plasma Institute, University of York, United Kingdom

<sup>2</sup> Ecole Polytechnique Fédérale de Lausanne (EPFL), Swiss Plasma Center (SPC), CH-1015 Lausanne, Switzerland

<sup>3</sup> Culham Centre for Fusion Energy, Culham Science Centre, OX14 3DB, UK

<sup>4</sup> Department of Physics SUPA, University of Strathclyde, Glasgow, G4 0NG, UK

<sup>5</sup> University of California San Diego (UCSD), San Diego, United States

<sup>6</sup> Consorzio RFX, Padova, Italy

<sup>7</sup> DIFFER, Eindhoven, The Netherlands

<sup>8</sup> See the author list of S. Coda et al. 2017 Nucl. Fusion 57 102011

<sup>9</sup> See the author list of H. Meyer et al. 2017 Nucl. Fusion 57 102014

## Abstract

The process of divertor detachment, whereby heat and particle fluxes to divertor surfaces are strongly reduced, is required to reduce heat loading and erosion in a magnetic fusion reactor. In this paper the physics leading to the decrease of the divertor ion current ( $I_t$ ), or ‘roll-over’, is experimentally explored on the TCV tokamak through characterization of the location, magnitude and role of the various divertor ion sinks and sources including a complete measure of particle and power balance. These first measurements of the profiles of divertor ionisation and hydrogenic radiation along the divertor leg are enabled through novel spectroscopic techniques which are introduced.

Over a range in TCV plasma conditions (plasma current, impurity-seeding, density) the  $I_t$  roll-over is caused by a drop in the divertor ion source; recombination remains either small or negligible until later in the detachment process. In agreement with simple analytical predictions, this ion source reduction is driven by a reduction in the power available for ionization,  $P_{\text{recl}}$ , sometimes characterised as ‘power starvation’. The concurrent increase in the energy required per ionisation,  $E_{\text{ion}}$ , further reduces the number of ionizations. The detachment threshold is found experimentally (in agreement with analytic model predictions) to be  $\sim P_{\text{recl}}/I_t E_{\text{ion}} \sim 2$ , which corresponds to the target electron temperature,  $T_t \sim E_{\text{ion}}/\gamma$  where  $\gamma$  is the sheath transmission coefficient. The loss in target pressure, required for target ion current loss, is driven not by just volumetric momentum loss as typically assumed but also due to a drop of upstream pressure.

The measured divertor profile evolution through detachment of the various ion sources/sinks as well as power losses and charge exchange are quantitatively reproduced through full 2D SOLPS modelling of a ramp of core plasma density through the detachment process.

## 1. Introduction

Divertor detachment is predicted to be of paramount importance in handling the power exhaust of future fusion devices such as ITER [1]. Aside from target power deposition due to radiation and

neutrals, the plasma heat flux ( $q_t$  in  $W/m^2$ ) is dependent on the divertor target ion flux density ( $\Gamma_t$  in ions/ $m^2$ ) and electron temperature ( $T_t$  in eV):

$$q_t = \Gamma_t(\gamma T_t + \epsilon) \quad (1)$$

where  $\gamma$  is the sheath transmission coefficient ( $\gamma \sim 7$ ) and  $\epsilon$  is the potential energy deposited on the target (13.6 eV for deuterium ion recombination into an atom), with the kinetic energy deposited being  $\Gamma_t \gamma T_t$ . Here, the energy recombination into molecules ( $\sim 2.2$  eV dissociation potential) is ignored [1, 2] and we use ‘kinetic’ to mean ‘kinetic and thermal’. Detachment provides the reduction of target heat flux by reducing both  $T_t$  and  $\Gamma_t$  lowering both the potential and kinetic contributions. The processes involved were identified early on as including particle, energy and momentum loss [3-7]. Equation 2 serves as the basis for discussion of the required drop in  $\Gamma_t$ :

$$\Gamma_t \propto n_t C_s \propto p_t / T_t^{1/2} \quad (2)$$

where  $C_s$ ,  $T_t$  and  $p_t$  are the target ion sound speed, temperature and pressure respectively assuming a target Mach number of 1.

Detachment is preceded by the heat flux along the field being conduction limited, which allows a temperature (density) gradient to form along the field lines *while the total pressure remains roughly constant*. Therefore, as the target temperature drops for such attached conditions ( $p_t$  constant) – both due to conduction and radiative dissipation lowering the kinetic heat flow reaching the target - there is a strong rise in  $\Gamma_t$  (Eq. 2). Although the kinetic energy deposited at the target is dropping proportional to  $T_t^{1/2}$ , the potential energy reaching the target rises, proportional to  $1/T_t^{1/2}$ . Radiative dissipation and heat conduction thus cannot simultaneously reduce  $T_t$  and  $\Gamma_t$ , required to lower both the thermal energy deposited at the target ( $\Gamma_t \gamma T_t$ ) and the potential energy reaching the target ( $\Gamma_t \epsilon$ ).

Detachment can achieve this goal through a simultaneous reduction of  $T_t$  and  $\Gamma_t$  which is inextricably linked to a reduction of target pressure, equation 2. In fact,  $p_t$  must drop faster than  $T_t^{1/2}$  for  $\Gamma_t$  to drop. Note that the drop in  $p_t$  does not necessitate any momentum loss along the field lines. In the absence of momentum losses, the upstream pressure,  $p_u$ , would need to drop during the ion current roll-over. One could imagine, for instance, a case where the upstream pressure is constant along a flux tube, but due to changes in the core plasma the pressure all along the flux tube is reduced. Such a degradation of the upstream pressure can influence the core plasma [4] and is thus to be avoided for a reactor-relevant divertor solution. This requires  $p_u \gg p_t$  and thus necessitates volumetric momentum loss to reduce  $p_t$ .

Target-current rollover is often taken to be the definition of detachment (although sometimes it is simply defined as  $T_t$  being less than some specified value, e.g. [8]). Therefore, in addition to playing a central role in the control of target heat flux,  $\Gamma_t$  (or the integrated  $\Gamma_t$  along the divertor target, which is  $I_t$  in ion/s) is experimentally important as a marker for the occurrence of detachment; it is the most accurately and easily measured detachment indicator in most tokamaks (using Langmuir probes) compared to others like  $p_t$  and  $T_t$ . Experimentally studying the role of the various processes of momentum, power and particle loss leading to the drop in  $\Gamma_t$  during detachment is thus an important area of research. More detailed information from experiments will provide a better basis for (in)validation of our current models of divertor plasma characteristics.

The loss of  $\Gamma_t$  during detachment is often described from a viewpoint that emphasises pressure drop along the field lines [3, 4, 8]. Assuming a fixed  $p_u$ , such a pressure drop can be correlated with a  $\Gamma_t$  reduction eqn. (2). Pressure drop is usually attributed to the dominance of ion-neutral reactions (e.g.

charge exchange and ion-molecule) over ionisation reactions at low temperatures ( $T_e \lesssim 5-10$  eV [4, 8]). Such studies note that the simultaneous reduction of  $\Gamma_t$  and  $T_t$  requires both parallel power loss as well as pressure loss.

Some researchers have also described the loss of  $\Gamma_t$  from a viewpoint that emphasises power and particle balance [7, 9-12]. In such models the divertor region is assumed to be ‘self-contained’ in the sense that the target ion flux is dominated by the sum of ion sources in the divertor (ionisation) minus the sum of ion sinks (recombination) [7, 9, 10]. We define this as high recycling conditions [9, 13]. This simplification ignores the ion flux into the divertor from upstream along a flux tube and any cross-field transport of particles (and momentum). Both the decrease in divertor ion source and increase in ion sink can play an important role. Those studies maintain that momentum loss, for instance through ion-neutral collisions, does not directly lead to a loss of  $\Gamma_t$  [9-11] but is a consequence of a reduction in power flow to the target lowering  $T_t$  and creating the conditions for momentum loss.

While viewing target ion current roll-over during detachment alternatively through the viewpoints of pressure loss or as a competition between ion sources (ionisation) and sinks (recombination) may appear to describe detachment differently, they are, in fact, not mutually exclusive and all cited processes can/will occur [4, 8, 9]. In this paper we show that both power loss (in fact power-limitation of the ion source) and volumetric momentum loss are both required to describe the TCV detachment observations.

Volumetric recombination is generally predicted to play a central role in target ion flux reduction [14-19]. The existence of volumetric recombination has been confirmed experimentally [7, 20-24] and is often found, through quantitative analysis, to be significant in the reduction of the ion target flux [7, 21-25]. However, in previous work on TCV [26], the volumetric recombination rate was shown to be only a small fraction of the reduction of ion flux, which is in agreement with recent TCV simulations [27], but in contrast with earlier TCV simulations [19]. Earlier studies of detachment in C-Mod [7, 22, 25] and ASDEX-Upgrade [23] (both higher density than TCV) show a range of contributions of recombination to target ion current loss from important to small (e.g.  $N_2$ -seeded discharges in C-Mod [6]).

The ion target flux  $\Gamma_t$ , which in steady-state equals the ionization rate ( $\Gamma_i$ ) if recombination is negligible, must be compatible/consistent with the power entering the recycling region, the power used in the ionisation process and the power reaching the target. Each ionization in the recycling region ‘costs’ a certain amount of energy per ionisation, which we define as  $E_{ion}$ , is comprised of two parts: a) the 13.6 eV ( $\varepsilon$  of eq. 1) required to take a bound electron to the continuum, and b) the amount of energy radiated arising from excitation collisions preceding ionisation. The power flux entering the recycling region (here termed  $q_{recl}$ ) supplies that ionization cost ( $\Gamma_t E_{ion}$ ), and thus  $\Gamma_t$ , as well as the power corresponding to the kinetic and thermal energy of the plasma arriving at the target,  $\Gamma_t \gamma T_{e,t}$ . Using power balance (in the absence of recombination), equation 3 must then hold [7, 9, 10, 13, 17]. Note that  $q_{recl}$  is larger than what reaches the target (eq. 1) due to excitation energy loss in  $E_{ion}$ . Therefore, as an alternative to reducing  $\Gamma_t$  through volumetric recombination, the ion source in the divertor itself can be reduced through a lack of sufficient power flowing into the ionisation region: a form of ‘power limitation’ (sometimes referred to as ‘power starvation’ [9, 13]).

$$\Gamma_t = \frac{q_{recl}}{E_{ion} + \gamma T_t} \quad (3)$$

Such power limitation has been quantitatively identified in experiments [7] and SOLPS simulations [10, 28, 29] as well as simple model predictions [7, 9, 10, 13, 17]. Such a reduction of  $\Gamma_t$  also requires target pressure loss (eq. 2), which requires either an upstream pressure drop, volumetric momentum losses or a mix. References [4,8] show more explicitly that in the case that  $p_u$  is held constant (volumetric) momentum-pressure loss, which becomes increasingly stronger at lower temperatures, (Figure 24 of [8]) is required for the target ion current to drop. A reduction in the  $q_{recl}$  could be realised through either increasing impurity radiation *inside* the divertor (shown in this paper) or by reducing the power flowing into the SOL [30]. Power limiting the ion source can be as important as recombination in target ion current loss, if not the primary process [7, 9, 10, 28]. Although experimental indications for such a process are available (either from inferred ion sources [7], or from qualitative spectroscopic ‘indicators’ based on  $D_\alpha$  [31]), one weakness of previous results is that this hypothesized reduction of the ion source during detachment has not been measured quantitatively. However, recent studies aim to provide quantitative information on ionisation during divertor detachment [32, 33].

In this work, we have improved the analysis of the Balmer series (section 3) to enable directly estimating a) the ionization source/recombination sink and their profiles throughout the outer divertor leg; and b) the total energy ‘cost’ per ionization,  $E_{ion}$  per ionisation event. This information is shown in section 4 and is compared with reduced analytical models [4, 7-9, 17], accounting for a minimum number of physical processes necessary to describe the observed detachment dynamics (section 5). Assuming knowledge of the target temperature, one only needs to consider power and particle balance to predict the target ion flux rollover (Eq 3). However, including momentum balance is necessary to predict  $T_t$  (and thus the magnitude and trend in the target ion current) while molecular reactions need to be included to explain our  $D_\alpha$  observations.

Our results (section 3) quantitatively verify that, at least for the TCV cases shown, the loss of target ion current is primarily due to an ionization source loss. Recombination, as an ion sink, has a lesser effect. This loss of ion source coincides with the power entering the recycling region approaching the power required for ionisation. The experimentally-determined profiles of ionization, recombination, electron density, impurity radiation along the divertor leg together with their variation in time are compared with SOLPS and show both qualitative and quantitative agreement.

In section 5 we show that our measurements confirm predictions by analytical models for the detachment onset [4, 8, 9]. We find that the ion current starts decreasing relative to the value predicted based on upstream boundary conditions when the power available for ionization,  $P_{recl}$ , drops to approximately twice the power,  $P_{ion}$ , required to produce the measured *total* target ion current,  $I_t$  (Eq. 4a). That threshold is equivalent to both a threshold based on the target temperature ( $T_t$ ) (Eq. 4c) and a threshold based on the ratio of upstream pressure ( $p_u$ ) and power flux into the recycling region ( $q_{recl}$ ), which depends on the target sound speed  $C_s$  given  $T_t \sim E_{ion}/\gamma$  (Eq. 4c). Our measurements also are consistent with those predictions. These thresholds are identified from analytic models as the point at which target pressure loss needs to start to occur as the increase of  $\Gamma_t$  with a reduction  $T_t$  (Eq. 3) the drop in  $T_t^{1/2}$  (Eq 2), also identified in literature as a detachment threshold [9, 13].

$$P_{recl,crit} \sim 2E_{ion}I_t \quad (4a)$$

$$\left(\frac{p_u}{q_{recl}}\right)_{crit} \sim \frac{1}{\gamma C_s \left(T_t = \frac{E_{ion}}{\gamma}\right)} \quad (4b)$$

$$T_t \sim E_{ion}/\gamma \quad (4c)$$

The picture that emerges from our TCV studies is that power limitation starts the detachment process through stopping/slowing the linear growth in TCV target ion current with upstream density predicted using a Two-point Model [4] which includes recycling energy losses (appendix A.4). At the same time  $T_t$  accesses a temperature range conveniently conducive to momentum loss ( $T_t < E_{ion}/\gamma$ ). Power limitation dominates the loss of ion source throughout the detached ( $I_t$  roll-over) phase. As  $P_{recl}$  continues to approach  $P_{ion}$  the target temperature reaches values conducive to recombination, resulting in a strong rise of the recombination rate. We feel that the above picture is applicable to various approaches to detachment – density scans,  $P_{SOL}$  reductions and impurity seeding. It also applies to higher density experiments where the effect of recombination, while larger than for TCV, must still await the drop in the  $T_t$  to low enough values driven by power limitation.

## 2. Experimental setup

Discharge number	$I_p$ (kA)	Greenwald fraction	
56567 (and repeats)	340	0.3 – 0.6	Density ramp
54868	240	0.25 – 0.6	Density ramp
52158	340	0.4	$N_2$ seeding ramp
57912	340	0.25 – 0.6	Density ramp

Table 1: Overview of discharges used in this work, together with their shot numbers, plasma current and Greenwald fraction.

All the research discussed involved L-mode Ohmic density/impurity ramp discharges made in the medium-sized tokamak, TCV ( $R = 0.89$  m,  $a = 0.25$  m,  $B_t = 1.4$  T)[34]. The characteristics of the various discharges utilised, as well as their equilibria, are shown in table 1 and Figure 1a, respectively.

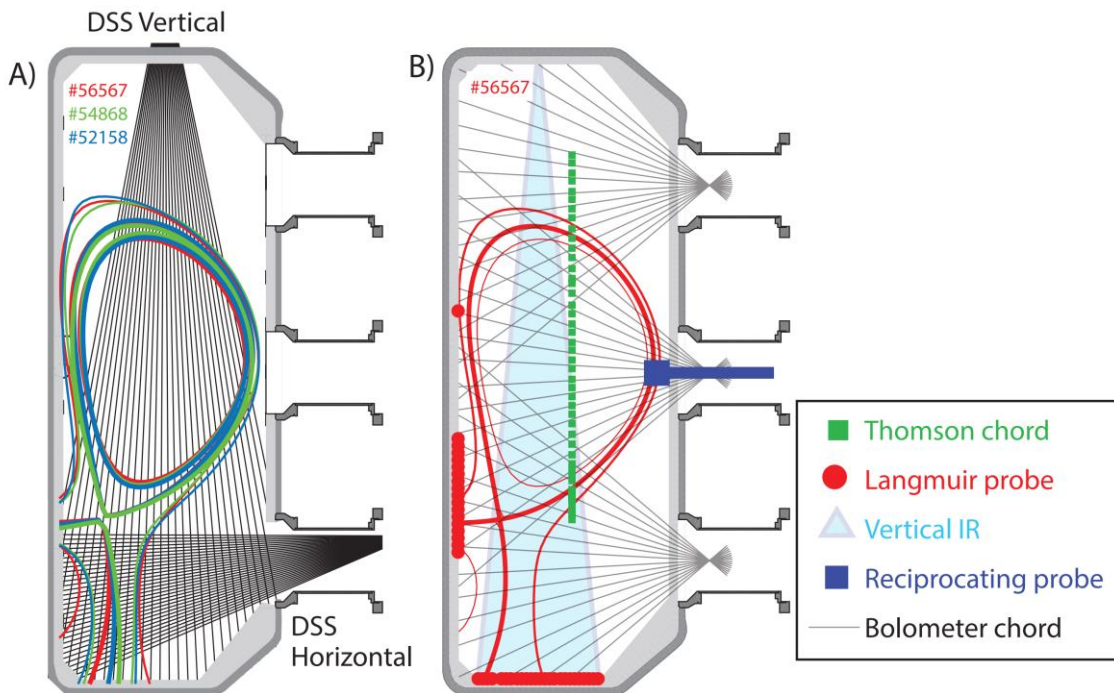


Figure 1. a): Lines of sight of the horizontal and vertical DSS systems. Divertor geometries for #56567 (red), #54868 (green), #52158 (blue) are shown. b) Lines of sight and locations of other diagnostics (Thomson/Langmuir probes/Vertical IR/Reciprocating probe/Bolometry) together with the divertor geometry of #56567.

To obtain ionisation sources and sinks, we utilised the newly developed TCV divertor spectroscopy system (DSS) [26]. The DSS consists of vertical and horizontal viewing systems, each employing 32 lines of sight (Figure 1a). *Our analysis is based on the horizontal system*, which provides full coverage for the divertor shapes studied in this work, intersecting the outer divertor leg with a spatial resolution of  $\sim 13$  mm. The spectrometer (Princeton Instruments Isoplan SCT 320) contains a triple grating turret which can be turned to change the grating used and to change the wavelength region covered (e.g. to enable measuring different Balmer lines). Each grating setting has corresponding absolute intensity calibrations and an instrumental function calibration over the entire camera.

A high resolution setting (0.06 nm spectral resolution with a 19 nm spectral range using a 1800 l/mm grating at a central wavelength of 404 nm) has been used to cover the line shape of the  $7 \rightarrow 2$  Balmer line to determine the local density using simplified Stark models presented in [26, 35, 36]. Those models have been verified against a more complete Stark model utilizing computer simulation techniques to determine the Stark line shape [37] as shown in [38] using TCV divertor spectra. The Stark-broadened width (the full-width-half-maximum) is small in the relatively low-density TCV plasmas compared to both the instrumental function width and the effect of the ion temperature (Gaussian FWHM of a  $T_i$  3-5 eV Maxwellian ion velocity distribution [26]. However, the Stark width and thus  $n_e$ , can still be extracted from the wings of the spectral shape, which corresponds to the Lorentzian-like Stark profile, provided a sufficient signal to noise ratio is available. To achieve this, the spectra is dynamically averaged over multiple frames to achieve a peak to noise level of higher than 30 for the Stark fitting. Comparison of the inferred Stark density is consistent across different Balmer lines fit ( $n=6,7,9,10,11,12,13$ ), indicating that the influence of the Doppler line shape and any non-Maxwellian distribution [38] is negligible in the Stark density inference. The main contributors to the Stark density uncertainty are instrumental function uncertainties and, when the spectra is dynamically averaged to improve S/N ratio, an uncertainty of  $\sim 10^{19} \text{ m}^{-3}$  is estimated.

Other diagnostics used for portions of the work presented are gold foil bolometers, target Langmuir probes [39], an upgraded Thomson scattering system [40], a reciprocating probe [41] and infrared imaging [42]. The locations of these different diagnostics are shown in Figure 1b.

We have divided the radiated power into core radiation (above the x-point) and divertor radiation (below the x-point). This is accomplished by utilising the brightness from poloidal bolometric chords over the appropriate region, while removing chords which intersect the inner divertor (to prevent contamination from inner divertor radiation). Such an analysis of bolometric chordal brightnesses has been used in place of the tomographic reconstruction of the radiated power emissivity across the entire plasma which can have significant uncertainties [43]. We note that due to the reflection of low energy photons from the gold foil of the bolometers, the estimated radiated power is assumed to be underestimated by at least 15% [44]. When considering other uncertainties, the overall underestimate of the radiated power ranges from 10% - 20%, which we correct for in our power balance analysis.

### 3. Spectroscopic analysis methodology

We describe the techniques utilized for our studies of the ion sources and sinks during detachment and start with a brief review of our techniques and nomenclature for describing the recombination sink [26] as well as the organization of the analysis flow that is undertaken.

The brightness of a hydrogen Balmer line ( $B_{n \rightarrow 2}$  in  $\text{ph/m}^2 \text{ s}$ ) with upper quantum number  $n$  can be described (See Eq. 5) along a path length  $\Delta L$  as function of electron density ( $n_e$ ), neutral density ( $n_o$ )

and temperature ( $T_e$ ) using the Photon Emissivity Coefficients ( $PEC_{n \rightarrow 2}^{rec}$ ) for recombination and excitation ( $PEC_{n \rightarrow 2}^{exc}$ ), obtained from the Open-ADAS database [45, 46].

$$B_{n \rightarrow 2} = \frac{\Delta L n_e^2 PEC_{n \rightarrow 2}^{rec}(n_e, T_e)}{B_{n \rightarrow 2}^{rec}} + \frac{\Delta L n_e n_o PEC_{n \rightarrow 2}^{exc}(n_e, T_e)}{B_{n \rightarrow 2}^{exc}} \quad (5)$$

Here it is assumed that: a) molecular reaction contributions to the Balmer line emission are negligible (this will be addressed in the section 5.3); b) the Balmer line emission originates from a plasma slab with spatially constant parameters (OD model) with a chord intersection length of  $\Delta L$ ; c) the hydrogen ion density equals the electron density (e.g.  $Z_{eff} = 1$ ) – which introduces insignificant errors on the analysis shown below [26].

Figure 2 illustrates the various steps in the analysis process, eventually resulting in estimates of both local plasma characteristics (weighted over the Balmer line emission profile along each viewing chord) and line integrated plasma parameters. The analysis starts with the Balmer line ratio and analysis of the Balmer line shape (Stark-broadened) to extract the density. These allow the determination of the fraction of the Balmer line brightness due to recombination and excitation (equations 6a and b).

$$F_{rec}(n) = \frac{B_{n \rightarrow 2}^{rec}}{B_{n \rightarrow 2}} \quad (6a)$$

$$F_{exc}(n) = \frac{B_{n \rightarrow 2}^{exc}}{B_{n \rightarrow 2}} = 1 - F_{rec}(n) \quad (6b)$$

$F_{rec}(n)$  and  $F_{exc}(n)$  are then combined with the absolute Balmer line intensity  $B_{n \rightarrow 2}$  to obtain the absolute Balmer line emission due to recombination and excitation ( $B_{n \rightarrow 2}^{rec}$ ,  $B_{n \rightarrow 2}^{exc}$ ) (section 3.1). These are then used to obtain the recombination ( $R_L$  in rec/m<sup>2</sup>s) and ionization ( $I_L$  in ion/m<sup>2</sup>s) rates (respectively), as well as the radiative power loss due to excitation and recombination ( $P_{rad,L}^{exc}$ ,  $P_{rad,L}^{rec}$  in W/m<sup>2</sup>, respectively) integrated along each chordal line of sight using the methodology first presented in [11], which is described in sections 3.2 and 3.3.

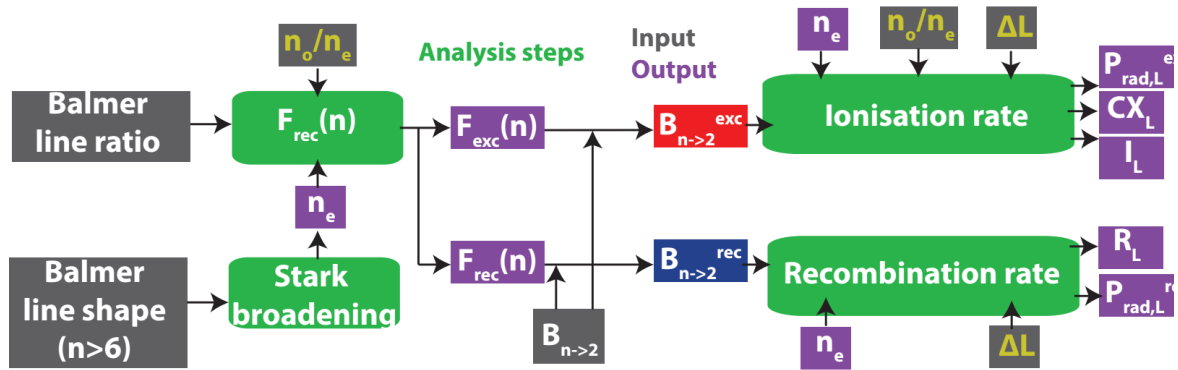


Figure 2: Schematic overview of recombination and ionisation rate analysis methodology. Inputs are shaded in grey, assumed inputs have yellow symbols, outputs in purple, analysis steps in green.

As shown in the flowchart, several input parameters (e.g.  $n_o/n_e$ ,  $\Delta L$ ) are required and assumptions must be made to characterize them, described in sections 3.1-3.3. The assumed uncertainty can be larger than 100% for some of those parameters. The effect is that a Taylor-expansion based error analysis is insufficient to accurately estimate uncertainties of the inferred output parameters. We thus developed and used a Monte-Carlo based probabilistic analysis to estimate output quantities and their uncertainties (section 3.4).

In the following we briefly review the method for separating recombination and excitation contributions to Balmer line intensities used to describe and calculate the excitation/ionization rates.

### 3.1 Separating excitation and recombination contributions of $B_{n \rightarrow 2}$

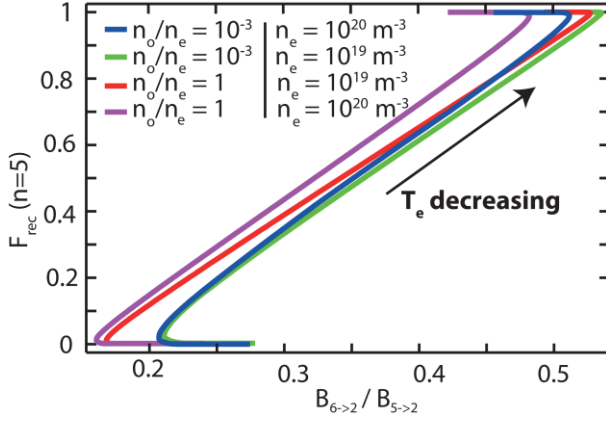


Figure 3:  $F_{rec}(n=5)$  as function of  $B_{6 \rightarrow 2}/B_{5 \rightarrow 2}$  for various electron densities and neutral fractions.

which the electron temperature varies, as shown in Figure 3 for the  $B_{6 \rightarrow 2}/B_{5 \rightarrow 2}$  ratio (similar for other line ratios). We note that a unique solution for  $F_{rec}(n)$  from the measured ratio of two Balmer lines is only obtained when  $F_{rec}(n)$  is in between  $\sim 0.15$  and  $\sim 0.85$ .

It is clear from Figure 3 that the  $F_{rec}(n)$  obtained is relatively insensitive to the electron density and neutral fraction making it strongly insensitive to line integration effects, which will be further discussed in appendix A.1. The characteristic uncertainty of  $F_{rec}(n)$  is  $\sim \pm 0.1$ , which was determined through a probabilistic analysis presented in section 3.4.

It is important to note that this analysis relies on the assumption that the neutral fraction is constant as function of temperature. Although the neutral fraction in a transport-less plasma changes strongly as function of temperature, the hydrogen neutral fraction in the divertor is dominated by transport, which leads to much smaller deviations in the neutral fraction. SOLPS-Eirene modelling results included in this work and the observed trends of the Balmer line ratio (which rises from values

Excitation and recombination contributions to the Balmer line emission along a viewing chord can be separated quantitatively using Balmer line ratios [26], enabling the determination of the recombination and ionisation rates.

For a given electron density and neutral fraction, both the line ratio between two Balmer lines ( $B_{n_2 \rightarrow 2} / B_{n_1 \rightarrow 2}$ ) and the fraction of emission due to recombination of a certain Balmer line ( $F_{rec}(n)$ ) become functions of only the electron temperature. This provides a relation between  $B_{n_2 \rightarrow 2} / B_{n_1 \rightarrow 2}$  and  $F_{rec}(n)$  over

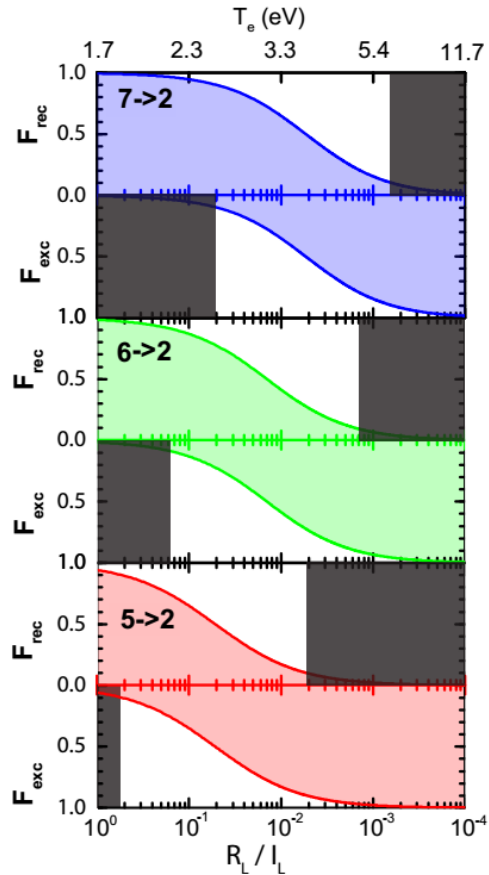


Figure 4:  $F_{rec}$  and  $F_{exc}$  as function of the ionisation to recombination ratio and  $T_e$  for the  $n=5,6,7$  Balmer lines, assuming  $n_e = 5 \cdot 10^{19} \text{ m}^{-3}$  and  $n_o / n_e = 0.05$ . Regions where  $F_{rec}/F_{exc} < 0.1$  are shaded.



corresponding to  $F_{\text{rec}} \sim 0$  towards values corresponding to  $F_{\text{rec}} \sim 1$  when the plasma is continuously cooled) support this conclusion. The Balmer lines used for each analysis must be chosen appropriately based on one's goal. This is illustrated in Figure 4 where, for a fixed electron density and neutral fraction, the variation of  $F_{\text{rec}}$  and  $F_{\text{exc}} = 1 - F_{\text{rec}}$  is given for three Balmer lines as a function of temperature. For the assumed fixed density and neutral fraction, decreasing temperature is accompanied by an increase in the recombination ionisation ratio ( $R_L/I_L$ ), which is also shown in Figure 4. When values of  $F_{\text{rec}}$  ( $F_{\text{exc}}$ ) are less than 0.1 the uncertainties in determining the recombination (ionization) rate are too large. Thus, inferring both the ionisation and recombination rate simultaneously can only be performed for a range, or window, of plasma conditions. These are different for each Balmer line; as the  $n$  level is decreased, the window in  $R_L/I_L$  ( $T_e$ ) shifts higher (lower). The regions where the line ratio is no longer sufficient to determine  $F_{\text{rec}}$  or  $F_{\text{exc}}$  for a given Balmer line, in terms of  $T_e$  and  $R_L / I_L$ , for a fixed  $n_e$  and  $n_o$ , are illustrated by the shaded regions in Figure 4.

The electron density strongly influences the range of  $R_L/I_L$  for which  $F_{\text{rec}}$  (or  $F_{\text{exc}}$ ) is around  $\sim 0.1$ , as shown in table 2. Essentially, the curves shown in Figure 4 would be shifted towards higher  $R_L/I_L$  with higher  $n_e$ , making it easier to detect recombination but harder to extract ionisation in the presence

	$n_e = 10^{19} \text{ m}^{-3}$		$n_e = 10^{20} \text{ m}^{-3}$	
	$F_{\text{exc}} = 0.1$	$F_{\text{rec}} = 0.1$	$F_{\text{exc}} = 0.1$	$F_{\text{rec}} = 0.1$
N=5	270	2	30	0.3
N=6	54	0.6	7	0.09
N=7	16	0.2	3	0.03

Table 2:  $R_L / I_L$  (in %) corresponding to  $F_{\text{rec}} (n \rightarrow 2)$  ( $F_{\text{exc}} (n \rightarrow 2)$ ) = 0.1

of recombination. Therefore, the Balmer line pair used in the analysis must be chosen appropriately for obtaining ionisation/recombination rate estimates depending on the expected dominance of recombination ( $R_L/I_L$ ) and the expected divertor densities. In practice, this means that using the  $n=6,7$  Balmer lines suffices for extracting densities, ionisation rates and recombination rates for typical TCV divertor conditions ( $n_e < 5.10^{19} \text{ m}^{-3}$ ,  $R_L / I_L < 0.1$ ). However, for a relatively dense TCV divertor ( $> 10^{20} \text{ m}^{-3}$ ), which can be achieved during L-mode density ramps with  $I_p \geq 340 \text{ kA}$ ,  $R_L/I_L > 5\%$  yields  $F_{\text{exc}} (n=6,7) < 0.1$  and thus a lower- $n$  Balmer line ( $n=5$ ), which has a larger  $F_{\text{exc}}$ , is required for ionisation inferences. Since high spectral-resolution data of the  $n=7$  Balmer line is still required for electron density estimations through Stark broadening, obtaining high spectral-resolution measurements for both the  $n=5,7$  Balmer line with the single available TCV DSS spectrometer required a repeat of discharges with different spectrometer wavelength ranges. Using the  $n=5$  Balmer line, as opposed to higher- $n$  Balmer lines, does mean that the sensitivity to detecting recombination becomes weaker, but recombination remains detectable when it increases above  $\sim 2\%$  of the ionisation rate.

Moving to using lower  $n$  Balmer transitions for determining the ionization rate as the divertor density increases has a limit: molecular reactions [22] will likely contribute significantly to the lowest- $n$  Balmer line intensities ( $n=3,4$ :  $D_\alpha$ ,  $D_\beta$ ) [9, 47] and, since this analysis neglects molecular processes, it is only suitable for  $n=5$  or higher Balmer lines – so one cannot move to just any lower  $n$  Balmer lines. Our analysis of the  $D_\alpha$  emission which is given in this paper (section 5.3) indicates a strong contribution ( $\sim 50\%$  or higher) of molecular reactions to the  $D_\alpha$  emission throughout a density ramp discharge, covering both the attached and detached phase (where  $D_\alpha$  appears to be strongly influenced by molecular reactions), for all lines of sight.

Inferring the ionisation rate using the highlighted technique and  $n=5$  may not be applicable at high densities as  $F_{\text{exc}} (n \geq 5) < 0.1$  may be reached (table 2). To address this, we have developed numerical algorithms (Appendix A.3) that can exploit that the temperature continuously decreases in the

divertor during a core density/seeding ramp to choose the appropriate solution where the solutions in Fig. 3 become double-valued at a given line-ratio.

The above discussion has implications for the common use of line ratio techniques to indicate the ‘dominance’ of recombination [4, 20, 48-51]. For such an analysis, the line ratios used to quantify this recombination “dominance” correspond to  $F_{rec} \sim 1$  in Figure 4. However, as shown in Figure 4 and table 2, the “dominance” of higher-n Balmer line emission ( $F_{rec} (n=6,7) > 0.9$ ) commences at recombination to ionisation rate ratios of 1-10% (depending on the density). Therefore, even if higher-n Balmer line emission is dominated by recombination, the ionisation rate can still be much higher than the recombination rate! Although line ratio techniques can be employed to gauge whether recombination is present and whether the Balmer line emission of a particular transition is dominated by recombination, they, by themselves, do not provide direct information on the magnitude of volumetric recombination and on the value of the recombination to ionisation ratio. Instead, quantitative calculations must be performed to infer both the magnitude of the ionisation and recombination rates.

### 3.2 Inferring ionisation and recombination rates

Once  $B_{n \rightarrow 2}^{rec}$  is obtained, the recombination rate integrated along a spectroscopic line of sight,  $R_L$  [rec/m<sup>2</sup> s] can be obtained from the inferred Stark density and the assumed path length  $\Delta L$  as highlighted in [26] and as shown in Figure 5a. Using an analogous approach, the ionisation rate integrated along a spectroscopic line of sight [ion/m<sup>2</sup> s] can be obtained from the inferred Stark density and an estimate of the combined parameter,  $\Delta L n_o / n_e$  (which represents a path length scaled neutral concentration in m), as illustrated in Figure 5b. For these techniques, the recombination and ionisation rates are modelled using the so called effective recombination coefficients (ACD), and effective ionisation coefficients (SCD) from the Open-ADAS tables [45, 46], which are functions of electron density and temperature. Figures 5a and b show  $I_L$  is considerably more sensitive to its defining input parameters than  $R_L$ . It is important to note that uncertainties of both the combined parameter  $\Delta L n_o / n_e$  (which has an order of magnitude larger uncertainty than just  $\Delta L$  on which the  $R_L$  determination depends) and  $n_e$  play a major influence in the uncertainty of  $I_L$ . This is another reason why we use a probabilistic analysis to robustly provide an estimate for both  $I_L$  and its uncertainty. This probabilistic analysis is used for all output parameters shown in Figure 2, except the inferred Stark density.

Line integration effects (appendix A.1) lead to differences between the inferred ionisation rate and the ‘true’ ionisation rate. Although these differences are larger for ionisation rate than for inferred recombination rates, for both cases the uncertainty introduced by line integration effects remains smaller than the characteristic uncertainty of the quantities themselves. To minimize the uncertainty in  $I_L$ , the lowest n Balmer line used for determining  $F_{rec}(n)$  is used to determine  $I_L$ , whereas the highest-n Balmer line is used to determine  $R_L$ . The results agree within uncertainty when either line in the Balmer line pair used to determine  $F_{rec}(n)$  is used to determine  $R_L$  and/or  $I_L$ . The results also agree when other (appropriate) Balmer lines are used which were not used to determine  $F_{rec}$ .

Determining  $I_L$  and  $R_L$  for all spectroscopic chords yields a profile of the line-integrated ionization and recombination rates (ion, rec / m<sup>2</sup> s) along the outer divertor leg. By integrating this profile toroidally and poloidally ( $I_i = \int 2 \pi r_i I_L(r_i, z_i) dz_i$  – similarly to [22]), the total volumetric ionisation ( $I_i$ ) and recombination rates ( $I_r$ ) are obtained (ion, rec / s) with uncertainties estimated from the probabilistic analysis. For this integral, the locations ( $r_i, z_i$ ) of the profiles along the outer divertor leg are ascribed to the intersections of the lines of sight with the separatrix (Figure 6a). With the extensive DSS

coverage of the outer divertor leg (Figure 1a) most of the ionisation and recombination in the outer divertor leg is covered by integrating over these profiles.

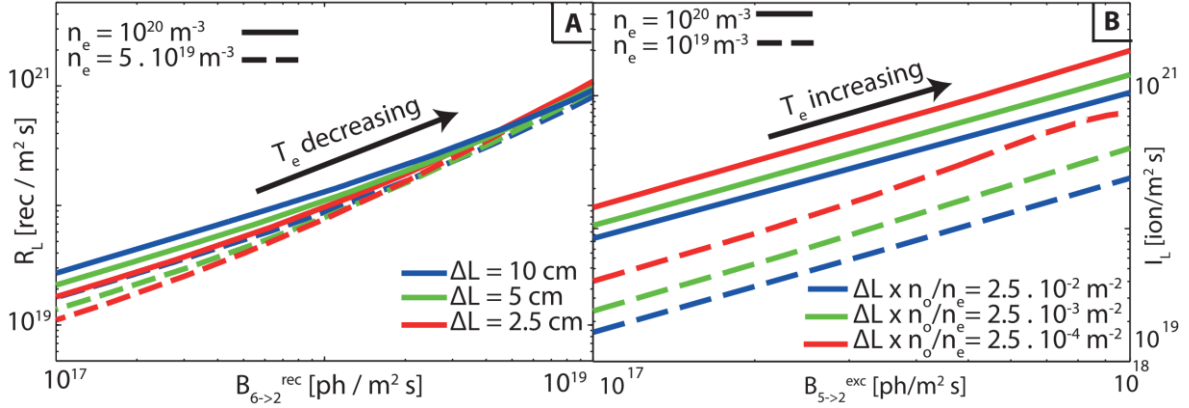


Figure 5: a) The recombination rate  $R_L$  along a spectroscopic line of sight as a function of  $B_{6 \rightarrow 2}^{rec}$  for various  $n_e$  and  $\Delta L$ . b) The ionisation rate  $I_L$  along a spectroscopic line of sight as function of  $B_{5 \rightarrow 2}^{exc}$  for various  $n_e$  and  $\Delta L \times n_o/n_e$ .

As described above, an estimate of the path length,  $\Delta L$ , through the region of strongest contribution to the measured brightnesses, is required. We assume that  $\Delta L$  (at the target) corresponds to the full-width-half-maximum of the ion target flux profile measured by Langmuir probes and its two corresponding flux surfaces (see Figure 6a). The  $\Delta L$  for points along the divertor leg is then calculated as the distance between the intersection of the spectroscopic lines of sight with these mapped flux surfaces (see Figure 6a). Since the  $J_{sat}$  SOL width increases during a core density ramp [52], the defined  $\Delta L$  is determined as function of time (Figure 6b). Comparing the estimated value of  $\Delta L$  using a synthetic diagnostic with the Balmer line emission profile along the line of sight obtained from SOLPS simulations (Appendix A.1), shows that the estimated  $\Delta L$  corresponds to a region where at least 70% of the Balmer line emission occurs.

This above process of determining ionisation and recombination rates leads to an estimate of the ‘characteristic’ temperature of the excitation ( $T_e^E$ ) and recombination ( $T_e^R$ ) regions along the chordal path length. Considering how  $I_L$  and  $R_L$  are determined, these temperatures are defined as the necessary temperature required for the OD plasma slab model of fixed quantities ( $\Delta L, n_e, n_o$ ) to match the experimental  $B_{exc}^{n \rightarrow 2}$  and  $B_{rec}^{n \rightarrow 2}$ . It has been verified that this way of obtaining  $T_e^R$  yields similar results to the temperature obtained by fitting the  $n > 9$  Balmer lines with a Saha-Boltzmann functional dependence on  $T_e^R$  (e.g., see tokamak applications [7, 21, 22]). Physically,  $T_e^E$  and  $T_e^R$  approximate a ‘chord-averaged’ temperature, weighted by the excitation and recombination emissivities respectively, along the line of sight.

The inference of both excitation and recombination rate temperatures is achieved through separate analyses and are usually different.  $T_e^E$  inferred from our measurements ranges from  $\sim 3$  eV to  $\sim 20$  eV, whereas  $T_e^R$  ranges from  $\sim 0.5$  to  $\sim 4$  eV. This temperature difference is due to the occurrence of recombination and excitation in different locations as confirmed with SOLPS-Eirene modelling (section A.1); excitation primarily occurs in higher temperature regions than recombination. From this, we can make two statements: 1) separating the excitation and recombinative emission makes the analysis more robust to line integration effects as it reduces the deviation in plasma parameters along the respective emission regions of the chordal integral; 2) by making  $T_e^E$  and  $T_e^R$  two separate

entities, line integration effects are partially compensated, and thus makes the analysis more robust to profile related effects (section A.1).

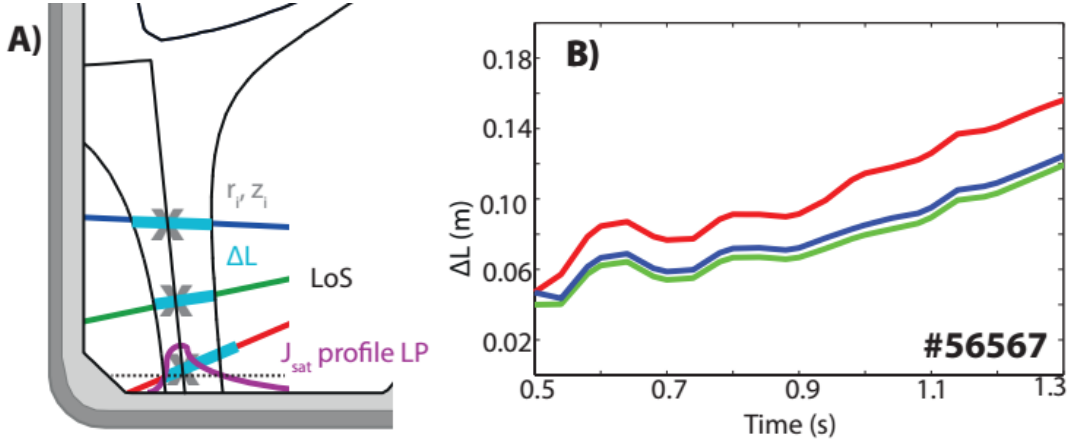


Figure 6: a) Cartoon illustrating how pathlength ( $\Delta L$ ) is determined using the FWHM of the  $J_{sat}$  profile, together with the profile locations ( $r_v, z_i$ ); which are the intersections of the lines of sight with the separatrix (X); of DSS inferences along the outer divertor leg. b) Example of  $\Delta L$  as function of time for three lines of sight.

For simplicity, in the earlier  $F_{rec}(n)$  calculation, the excitation and recombination temperatures are assumed to be equal. However, when  $T_e^R$  and  $T_e^E$  are each directly used to determine  $F_{rec}$  the  $F_{rec}$  obtained is consistent with the initial  $F_{rec}$  within 2%.

Using a similar approach to determining  $I_L$  using  $B_{n \rightarrow 2}^{exc}$ , the charge exchange rate to ionisation rate ratio can be estimated using ADAS values [45, 46] of the charge exchange rate, ionisation rate and excitation PECs. This is identical to using the Stark density together with the ‘characteristic’ temperature of the excitation region to directly obtain the charge exchange rate to ionisation rate ratio from ADAS.

We note that the above analysis only includes recombinations/ionisations due to atomic processes. We do not currently have a technique, of relatively similar difficulty to that described above for atomic processes, to easily determine the molecular-activated recombination (MAR) and ionization (MAI) rates which may be significant. However, the observed  $D\alpha$  (and accompanying analysis) is indicative of the presence of MAR during detachment (section 5.3.2).

### 3.3 Estimating hydrogenic radiative power losses

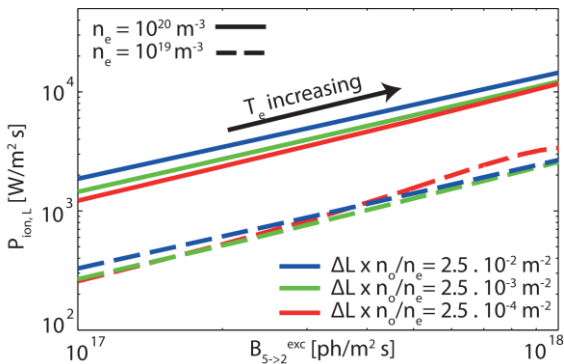


Figure 7: Power required for ionisation along a line of sight as function of the emission due to excitation ( $n \rightarrow 5$ ) for various levels of electron density (solid vs dashed) and  $\Delta L \times n_o/n_e$ .

The amount of energy expended per ionization is central to our analysis of the role of power balance in the ionization process. To obtain this, first we obtain the total power loss due to ionisation over a chordal integral,  $P_{ion,L}$  (W/m<sup>2</sup>). This is modelled in Eq. 7a using the OD plasma slab model with spatially constant parameters as function of  $T_e^E$ ,  $n_o$ ,  $\Delta L$  and  $n_e$  using ADAS [45, 46] tables for excitation and recombination driven radiative power losses (PLT and SCD), which are both functions of electron temperature and electron density. The first part of  $P_{ion,L}$ , represents the radiative losses associated

with ionisation ( $P_{\text{rad,L}}^{\text{exc}}$ ), which occur during the several, to multiple, excitation collisions where energy is lost due to line radiation as the atom deexcites before finally ionizing.  $P_{\text{rad,L}}^{\text{exc}}$ , the first term in eq. 7, is modelled using the PLT table, which represents the radiated power ( $\text{W m}^{-3}$ ), obtained through ADAS by integrating over the full excitation spectra modelled using ADAS [45, 46]. The second contribution to  $P_{\text{ion,L}}$  is the energy removed from the plasma and stored as the potential energy of a new ion -  $\epsilon = 13.6 \text{ eV}$  [1, 2] (where as mentioned previously, the molecular dissociation is ignored), which is obtained by multiplying the ionisation rate  $I_L$  with  $\epsilon$ , resulting in  $P_{\text{ion,L}}^{\text{pot}}$  in Eq 7.

One important parameter we will use later is the energy ‘cost’ per ionisation (averaged along a chord, weighted by the ionisation profile along the chord), which is obtained by dividing  $P_{\text{ion,L}}$  with  $I_L$ , resulting in equation 7b.

The experimental estimation of the power loss due to ionisation is analogous to the ionisation rate inference in section 3.2 (Figure 6b); by using the excitation brightness, Stark density and by using an estimate of  $\Delta L \times n_o/n_e$ . The results, shown in Figure 7, are identical to using Eq. 7 in combination with the temperature of the excitation region obtained previously during the ionisation rate inference.

$$P_{\text{ion,L}} = \underbrace{\Delta L n_e n_o \text{PLT}(n_e, T_e)}_{P_{\text{rad,L}}^{\text{exc}}} + \underbrace{\Delta L n_e n_o \epsilon \text{SCD}(n_e, T_e)}_{P_{\text{ion,L}}^{\text{pot}}} \quad (7a)$$

$$E_{\text{ion}} = \frac{\text{PLT}(n_e, T_e)}{\text{SCD}(n_e, T_e)} + \epsilon \quad (7b)$$

Examination of the energy cost per ionization (equation 7b) reveals that the radiated energy per single ionisation event (and thus  $E_{\text{ion}}$ ) increases strongly at low electron temperatures (see, for example, [4, 53]). According to our analysis results in section 5.1.3,  $\sim 25 \text{ eV}$  per ionisation is needed during periods of the attached phases of the discharges studied, increasing to  $\sim 40 \text{ eV}$  in the detached case while rising above  $80 \text{ eV}$  in colder regions below the peak ionisation region where few ionisations occur.

Using a similar approach, the Open-ADAS PRB parameter [45, 46] can be used to estimate the radiated energy losses due to recombination per recombination reaction. The PRB parameter combines both radiated power due to recombination (three-body and two-body recombination; including both line emission and continuum emission) and bremsstrahlung (electron - hydrogen ion collisions). Since we are only interested in radiative losses due to recombination, the Bremsstrahlung component (whose contribution is negligible for recombination-relevant temperatures) is subtracted from the PRB coefficient by modelling the radiated power due to Bremsstrahlung as listed in [54]. The radiative losses due to recombination are found to be  $12.5\text{-}14.5 \text{ eV}$  per recombination reaction (see section 5.1.3), which are very similar to  $\epsilon$ . The influence of recombination on the divertor power balance is further discussed in sections 4.3 and 5.1.3.

### 3.4 Probabilistic analysis

Given the complicated set of analyses together with multiple input parameters shown in Figure 2, we have developed a Monte Carlo based probabilistic analysis to more accurately characterize the analysis outputs (recombination and ionization rates, hydrogenic radiative losses, charge exchange rates) and their uncertainties in the form of probability density functions (PDFs). This analysis also makes the result less prone to errors in the input parameters. An important part of this process is that the functional form for the uncertainty of each input parameter must be properly characterized – ranging from Gaussian (e.g.  $B_{n \rightarrow 2}$ ) to asymmetric Gaussian (e.g.  $\Delta L$ ) to flat (e.g.  $n_o/n_e$ ); PDFs for all input parameters are shown in appendix A.2, where further details on the probabilistic analysis

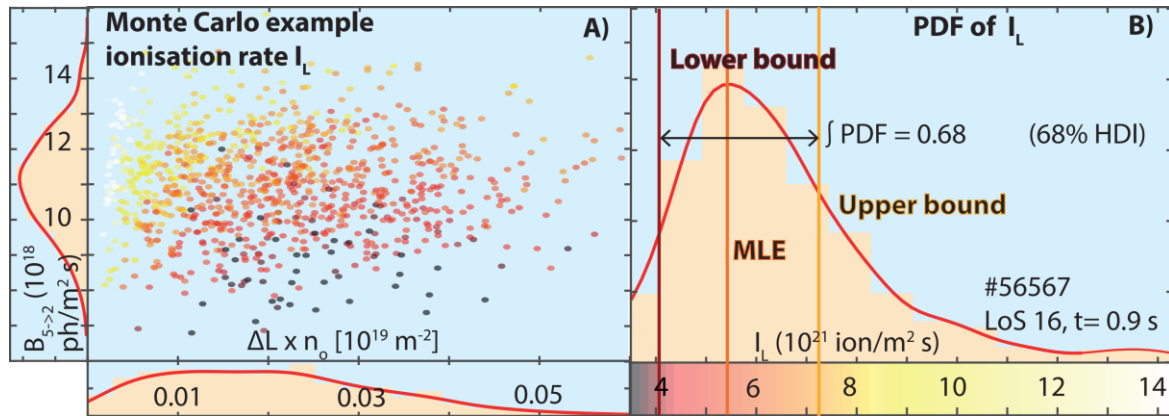


Figure 8: Example of probabilistic analysis which shows in a) a scatter plot of the randomly chosen values for the brightness and  $\Delta L \times n_o$ , whose colour coding corresponds to the value of the ionisation rate shown below b) the PDF of the ionisation rate, together with the estimate of the parameter (Maximum Likelihood Estimate (MLE)) and with its 68% Highest Density uncertainty Interval (HDI).

are provided. Since the neutral fraction is only known within a large range from modelling [27, 29, 51], a flat, as opposed to peaked, distribution of  $n_o/n_e = [10^{-3} - 0.05]$  is used. In the SOLPS simulation of discharges presented later (section 4.1.2), the Balmer line emission-weighted ( $n=5,6$ )  $n_o/n_e$  along the DSS divertor chords remains between 0.01 – 0.03 throughout the entire density ramp simulated.

An example of the probabilistic analysis is shown in Figure 8 for the line integrated ionisation rate  $I_L$  (result for a single chord, at a given time). The main parameters driving the  $I_L$  uncertainty in this particular case are the uncertainties in the brightness as well as  $\Delta L \times n_o/n_e$  shown in Figure 8a. Other uncertainties, such as the uncertainty in the line ratio and electron density also contribute, but to a lesser extent. The scatter plot of Figure 8a shows the randomly sampled values of the distributions of  $\Delta L \times n_o/n_e$  and  $B_{5 \rightarrow 2}$  from their uncertainty PDFs which are shown as histograms to the sides of each Figure. A ‘kernel density estimate’ (a statistical non-parametric technique for providing smooth estimates for probability density functions) is employed to convert the analysis outputs into a PDF using an adaptive kernel density estimation algorithm [55]. The colour of each point in the scatter plot (Figure 8a) corresponds to an ionization rate given in the colour bar below the resultant PDF of the ionisation rate of Figure 7b.

We apply analysis techniques adopted from Bayesian analysis [56] to extract information from the PDFs. The uncertainty of the estimate is given by the shortest interval whose integral corresponds to the requested uncertainty range; commonly referred to in literature [57] as the “Highest Density Interval (HDI)”; which provide the upper and lower uncertainties for our estimates. For unimodal PDFs, which is generally true for the PDFs resulting from our analysis (see Figure 8b and Appendix A.2, where a plot of all the characteristic PDFs in the analysis are shown), this interval also contains the maximum likelihood (peak) of the PDF, which we use as an estimate for the resulting parameter since it has the highest probability to occur.

The uncertainty margin for  $I_L$  can be strongly asymmetric as shown by the asymmetric tail of the PDF. Based on a comparison of this high  $I_L$  asymmetric tail to the Monte Carlo scatter plot result of Figure 8a, we can conclude that low values for the neutral fraction lead to higher ionisation rates. Lower neutral fraction corresponds to higher  $T_e^E$  which is needed to match the measured excitation emission as the number of ionisations per emitted excitation photons increases at higher temperatures.

### 3.5 Reproducibility of repeat discharges

As mentioned in section 3.2, there are cases where both low- and high-n Balmer lines are needed to infer the excitation and ionisation rates. A case in point is TCV pulse #56567 (shown later) where lower-n Balmer lines ( $n=5,6$ ) are used for line ratios and hence  $F_{\text{rec}}$  ( $F_{\text{exc}}$ ) while  $n=7$  is utilized for Stark density inferences, which requires diagnostic repeats (section 3.1). To demonstrate such reproducibility we show, in Figure 9, the variation of the brightness and Stark density measurements for a

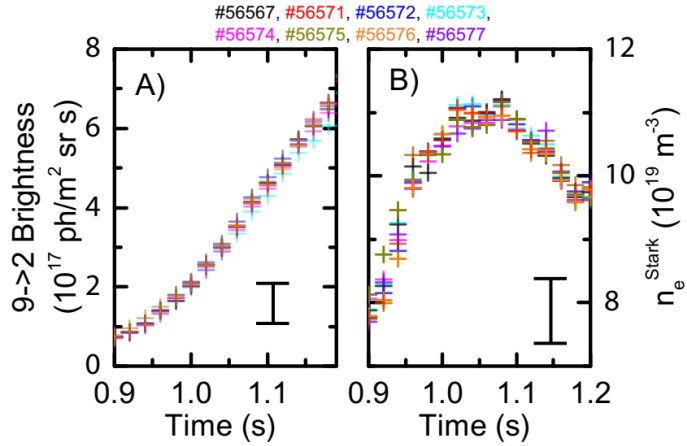


Figure 9: a) 9->2 Balmer line brightness and b) inferred Stark density from the 9->2 Balmer line obtained from the vertical system using the line of sight closest to the strike point location. Each colour indicates a different discharge. Characteristic uncertainties are shown in the

set of 8 identical discharges (#56567 is part of that sequence). The time dependencies of Balmer  $n=9$  line intensity (Figure 9a) and the derived chordal averaged (weighted by the  $n=9$  (recombinative) emission profile) density (Figure 9b) are the same within uncertainty from discharge to discharge. In addition, results from other diagnostics (bolometry and Langmuir probes – not shown) also agree within uncertainty for the repeated discharges, indicating a sufficient reproducibility for our central measurements of the divertor plasma characteristics.

## 4. Results

Analysis of three discharges, including two core density ramps (at two different plasma currents) and a nitrogen seeding ramp, show that the ionization source is the primary process that determines the target ion current and its reduction at detachment in TCV, whereas the role of recombination as an ion sink remains secondary. The magnetic geometries for the three cases are shown in Figure 1a and table 1 gives their key parameters. All discharges are in L-mode without additional heating and are performed in reversed field (e.g.  $\nabla B$  in the unfavourable direction) to stay out of H-mode.

Analyses of just the power balance, utilizing hydrogenic and total radiation estimates, show that the power reaching the recycling region,  $P_{\text{rec}}$ , is reduced during a density ramp discharge due to increasing impurity radiation. This power can also be taken as the maximum power ‘available for ionisation’ [13, 17]. In contrast, the power ‘required for ionization’,  $P_{\text{ion}}$ , increases during the pulse until  $P_{\text{ion}} \sim P_{\text{rec}}$  to within experimental uncertainties, which approximately correlates with the roll-over point for the target ion current; this suggests that the ion source is limited by the available power. The role of pressure and momentum loss will be covered in section 5.

### 4.1 Detachment characteristics on TCV

First, it is important to characterize the ion target current loss during detachment. Secondly we investigate the dynamics of the high density, ionisation, recombination, etc. regions during detachment experimentally, which are compared with SOLPS simulations. Previous studies have provided complementary descriptions of the development of detachment in TCV [19, 26, 51, 58, 59] and are thus useful for further details.

#### 4.1.1 Characterization of target ion loss

Density ramp experiments use feedback control of the  $D_2$  fuelling is used to obtain a linear increase of the line averaged core density,  $\bar{n}_e$ , measured by a vertical FIR interferometer chord.  $\bar{n}_e$  is increased until the plasma disrupts at  $t=1.25$  s, achieving a maximum Greenwald fractions of  $\sim 0.65$ . Both the total ion target flux integrated across the divertor target,  $I_t$  in ion/s, and the target ion flux density at the separatrix ( $\Gamma_t$  in ion/m<sup>2</sup> s) (Figure 10b), initially increase linearly with both the line-averaged and separatrix density,  $n_{e,u}$  (Figure 10a). At  $\sim 0.85$  s,  $\Gamma_t$  starts to roll-over while  $I_t$  starts to deviate from its linear trend; we use that deviation to define the onset of the process of detachment. Later (section 4.1.2), we will show that this time is in accordance with detachment onset predictions (section 5.2) and corresponds to when the ionisation profile peak lifts off the target (section 4.1.2). Note that the  $I_t$  roll-over (negative slope in  $I_t$ ) can occur after the point where  $I_t$  starts to deviate from its linear trend. The separation between the deviation and rollover times (see Figure 13d-f) can vary from one discharge to another.

The linear scaling of  $I_t$  and  $\Gamma_t$  with the upstream/core density for attached plasmas was observed for all the density ramp studies at TCV

[58]. This contrasts the  $\Gamma_t \propto n_{e,u}^2$  scaling observed in other tokamaks [6, 48]. Further analysis in section 5.2.1 will show this linear increase of  $I_t$  and  $\Gamma_t$  is expected when considering the reduction of upstream temperature and the increase in divertor radiation throughout the discharge. To quantify the loss of target ion current for this study we determine a linear, in upstream density and thus time, fit to the ion target current during the attached phase and extrapolate into the detached phase. The ' $I_t$  loss' is then the difference from this to the measured ion target current,  $I_t$  (see Figure 10b).

Although spectroscopic signatures of recombination start to appear just before the ion target flux roll-over, the  $I_t$  loss is significantly larger than the total recombination sink integrated over the entire outer leg (Figure 10b), indicating recombination alone is insufficient (at least by a factor three) to fully explain the  $I_t$  roll-over. This observation is general on TCV ([26] and section 4.2) and has also been observed under higher density conditions in Alcator C-Mod [7] as well as under  $N_2$  seeded conditions [33].

4.1.2 Experimentally observed TCV detachment dynamics with a comparison to SOLPS results  
During the periods before, during and after the target ion current roll over ( $\sim 1$  s) the poloidal profiles of several plasma parameters along the outer divertor leg vary. These are shown in Figure 11c, e, g, i at the times indicated by the vertical lines of Figure 11a. In Figure 11d, f, h, j we display the plasma profiles for a series of SOLPS simulations [27] that are representative of a density ramp obtained by performing multiple simulations for a range of upstream densities, which are reached by varying the gas puffing in the code for this particular run.

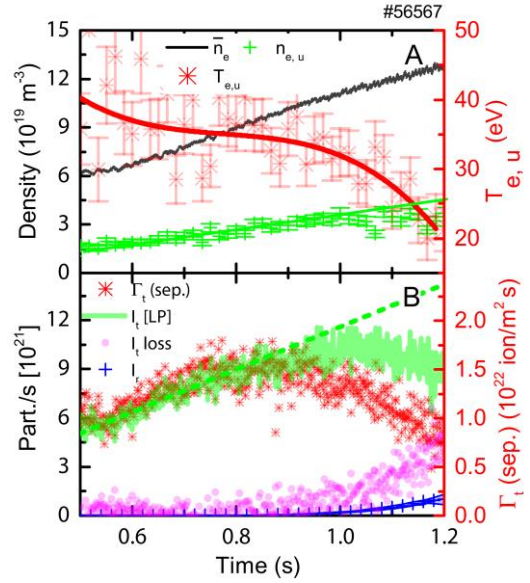


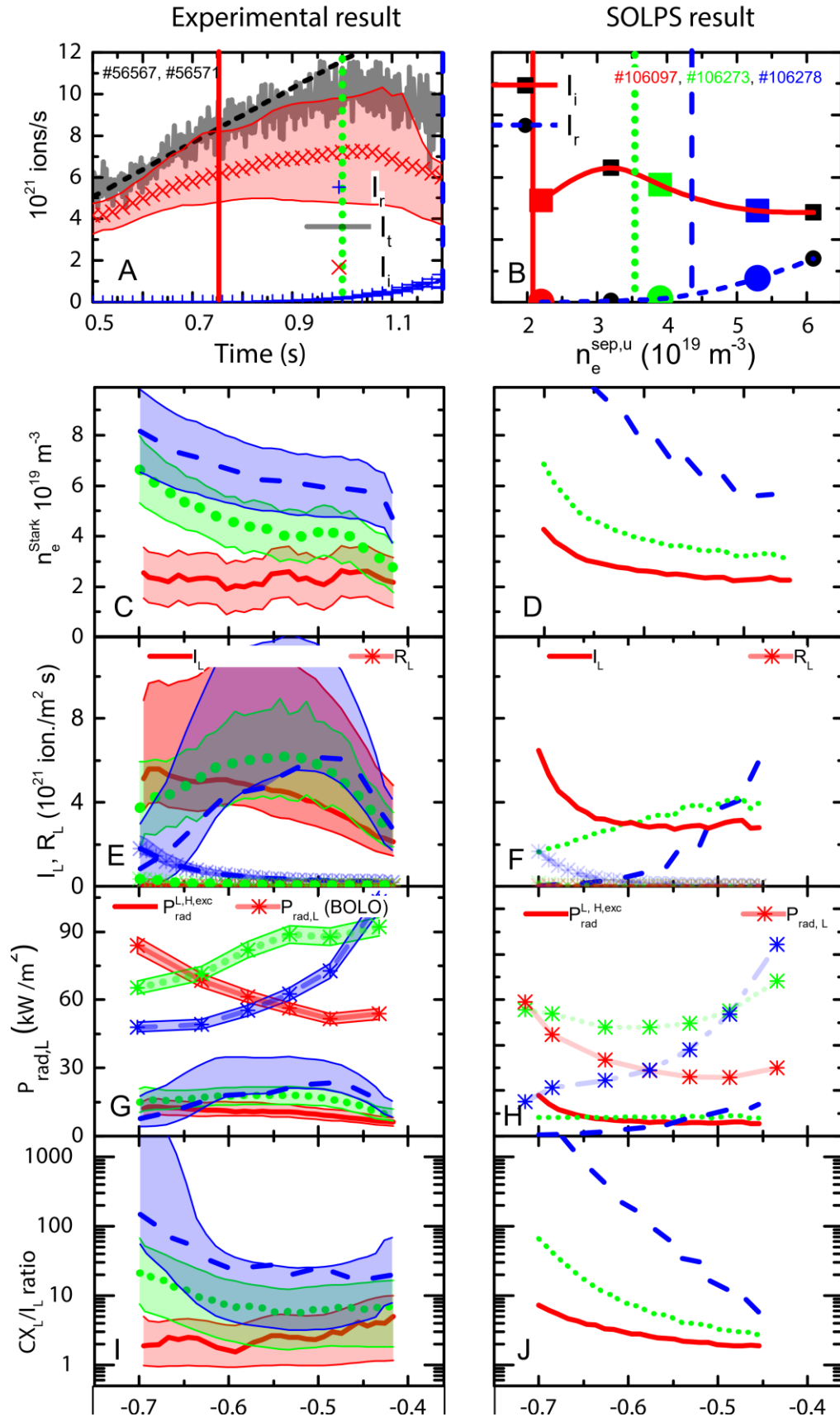
Figure 10: Overview of detachment based on a high  $I_p$ , density ramp discharge (#56567). a) Line averaged,  $\bar{n}_e$ , upstream density,  $n_{e,u}$  and upstream temperature,  $T_{e,u}$  as function of time. b) Total Ion target flux ( $I_t$ ), ion target flux density at the separatrix ( $\Gamma_t$ ), recombination rate ( $I_r$ ) and  $I_t$  loss as



Before detachment, the density along the divertor leg (Figure 11c), the radiated power (Figure 11g –  $P_{rad,L}$ ) and recombination rate (Figure 11e –  $R_L$ ) all peak near the target. Further increases in  $\bar{n}_e$  and  $n_{e,u}$  generate a gradual shift in the radiated power peak towards the x-point, followed by a displacement of the peak in the ionization region (Figure 11e –  $I_L$ ). The process of detachment starts to occur when the ionization peak lifts off the target, corresponding to a flattening of the measured ion target current ( $\sim 0.83s$  Figure 11a). As the ionization moves away from the target a region where charge exchange dominates over ionisation is left behind (Figure 11i), eventually extending over a region up to  $\sim 20$  cm from the target. During the entire detached phase, both the Stark density and recombination rate continue to increase across the entire divertor leg whilst their peaks remain near the target (Figure 11c and 11e) where the lowest DSS measurement chord is  $\sim 5$  cm above the target surface. At the highest core density, recombination dominates over ionisation only over a small region ( $<10$  cm) close to the target (Figure 11e). The general development of detachment on TCV is illustrated by the profiles in Figure 11.

All of the above observations are in excellent qualitative (and in most cases even quantitative) agreement with the SOLPS simulation results (Figure 11a vs b; Figure 11c vs d; Figure 11e vs f; Figure 11g vs h; Figure 11i vs j). The upstream density corresponding to the times indicated by the vertical lines in Figure 11a are shown in Figure 11b. This simulation does not reproduce the experimental result that the upstream density saturates upon detachment as is shown in the experiment. As such, a linear trend of the upstream density has been used to match the chosen times to the appropriate  $n_{e,u}$ . The three simulations used to compare the SOLPS profiles to experimental profiles are indicated by the enlarged symbols in Fig. 11b, where their colours correspond to the vertical lines at which the experimental data is taken, shown in Figure 11a. The SOLPS profile results (Figure 11f, h, j) are obtained by integrating through the 2D SOLPS profiles of ionisation, recombination, etc.) along the DSS and bolometric chords (Figure 11h -  $P_{rad,L}$ ), enabling a closer comparison between experiment and simulation. The SOLPS integrated results (Figure 11f) are obtained by integrating the ionisation source/recombination sink over the region covered by the entire horizontal DSS horizontal viewing chord fan (figure 1a). The SOLPS ‘Stark density’ result (Figure 11d) is obtained from a synthetic DSS diagnostic. Further details of how the synthetic measurements created from SOLPS output are provided in appendix A1.

*Figure 11: Left hand side: Experimentally (spectroscopic inferences + bolometry) determined quantities along the outer divertor leg. Right hand side: Results obtained directly from SOLPS simulation utilizing synthetic diagnostic measurements. a) Total ion target flux, outer divertor integrated ion source and recombination rate ( $I_i$ ,  $I_r$ ), together with the linear scaling of the ion target flux as function of time and vertical lines corresponding to the times at which the profiles are shown in the figures below. b) Analogous ion source/sink plot (outer divertor integrated) obtained from SOLPS where the ionisation source and recombination sinks are shown as function of upstream density. c, e) Stark density profiles (c – obtained from a synthetic diagnostic – see Appendix A.1). e, f) Chordal integrated recombination ( $R_L$ ) /ionisation rate ( $I_L$ ) profiles. g, h) Chordal integrated total radiation profiles through bolometry –  $P_{rad,L}$ ; and radiation due to hydrogenic excitation –  $P_{rad,L}^{H,exc}$ . i, j) Line integrated charge exchange ( $CX_L$ ) to ionisation ratio ( $I_i$ ) profiles.*



#### 4.1.3 The dynamics of the electron density in the divertor during detachment

The three time points in the general plasma characteristic profiles along the divertor leg (Figure 11c, f, g, h) provide a coarse temporal resolution and therefore do not fully convey the dynamics of the electron density near the target, which we expect, based on previous work [2, 24, 35], to drop as the low pressure/density regions expand from the target towards the x-point during detachment.

Stark density measurements from the 7 horizontal DSS viewing chords closest to the target are shown in Figure 12a together with the viewing geometry (Figure 12b). This discharge is similar to the one discussed in 4.1.1 and 4.1.2, but with a magnetic geometry optimised for DSS strike point coverage. At approximately the time of the total ion target current roll-over ( $\sim 0.87$ s), which coincides with the time where the ion target flux deviates from its linear trend (not shown), the measured Stark density for the viewing chord nearest to the target rises above the peak density measured by Langmuir probes at the target (Figure 12a). Afterwards, when the core density is further increased, the Stark density (within  $\sim 5$  cm from the target) peaks after which it rolls-over, which happens after the ion target current roll-over and after the target density peak (Langmuir probes, Figure 12a) starts dropping. This data is consistent with observations from the vertical DSS system indicating a reduction in line averaged (9- $\rightarrow$ 2 Balmer line, thus recombination emission weighted) density throughout the divertor leg (Figure 9b). Since the density peak must have started at the target before detachment, the strong decreasing trend of the lowest viewing chord density would be consistent with the density peak *starting to move up* along the leg.

There is a concern that the Langmuir probe measurement of the target density is incorrectly low. Since the Langmuir probe density inferences uses the Langmuir probe temperature inference ( $J_{sat} \propto n_e^{LP} \sqrt{T_e^{LP}}$ ), the density would be underestimated when  $T_e^{LP}$  is overestimated – which generally

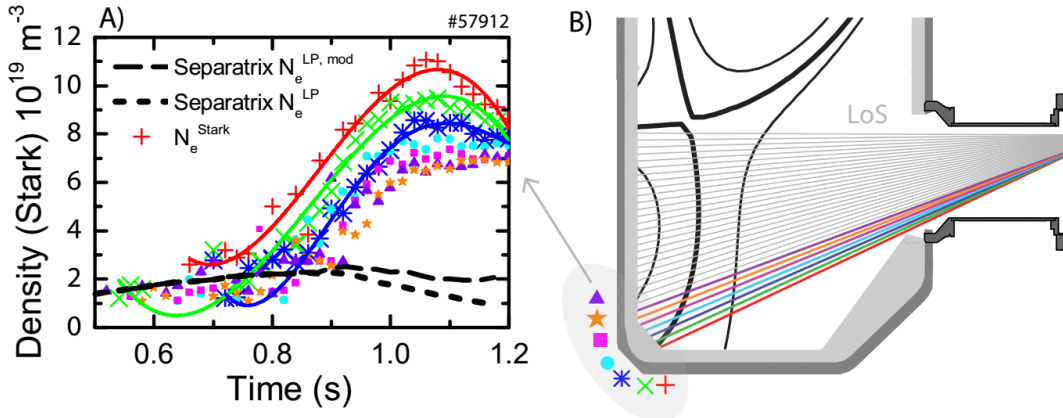


Figure 12: A) Electron density (characteristic uncertainty  $\sim 10^{19} \text{ m}^{-3}$ ) traces density from target Langmuir probes and DSS chords near the target (#57912) for a density ramp experiment. B) Divertor geometry and line of sights corresponding to the DSS measurements.

occurs in cold divertor conditions [39, 60, 61]. As such, following a similar approach as in [26], we calculated a modified  $n_e^{LP,mod} = n_e^{LP} \sqrt{\frac{T_e^E}{T_e^{LP}}}$  using a spectroscopically inferred  $T_e^E$  (section 5.1.1) from the excitation emission of the chord closest to the target (Figure 12a).  $n_e^{LP,mod}$  remains significantly smaller than the observed Stark density upon detachment. Some combination of the width of the poloidal viewing chord (1-2 cm) and the weighting of the Stark density towards the higher densities (and thus higher emissivities) along the cone describing the target line of sight is driving this difference. This discrepancy thus suggests that the electron density strongly decreases in a narrow

region (< 2 cm) close to the target. The Stark electron densities in low temperature conditions could be overestimated (for the case presented by up to  $2 \cdot 10^{19} \text{ m}^{-3}$  at the end of the discharge), according to certain Stark models [37] due to the electron temperature dependence of the Stark width [62]. A decay of the electron density in such a narrow region during detachment is also observed in the SOLPS simulations [27], although the amount the electron density decays ( $1-2 \cdot 10^{19} \text{ m}^{-3}$ ) appears to be smaller.

4.2 Characterization of the loss of ion source and its effect on the ion target flux  
 In the survey of discharge characteristics (Figure 11), the inferred ionization source magnitude and time dependence appears to determine the current reaching the target. The following discussions are based on particle balance over the entire divertor and not just a particular flux tube. The balance of sources and sinks *within* the divertor can be written:

$$I_t \approx I_i - I_r \quad (8)$$

where the target ion flux (the sink for ions at the target),  $I_t$ , is the sum over the divertor target surface while both the ionization source,  $I_i$ , and the volumetric recombination sink,  $I_r$ , are integrated over the entire outer divertor leg. Equation 8 assumes the divertor to be a closed, self-contained, system where the total divertor ion target current is dominated by divertor ion sources, ignoring sources of ions outside the divertor (core or SOL ionization) which flow from upstream towards the target; an approach used previously [7, 9, 10] and we will discuss it further in section 4.3. In this paper we define the divertor to be ‘high recycling’ when this condition (Eq. 8) is valid.

#### 4.2.1 Characterization of ion sinks and sources in density ramp discharges

We show examples of the equivalence of the divertor ionization source and target ion current in the first two columns of Figure 13 for density ramp discharges at two different plasma currents. The ionisation source (Figure 13b & e),  $I_i$ , tracks the increasing target flux,  $I_t$ , (within uncertainties) during the attached phase for both density ramp cases while recombination,  $I_r$ , is either negligible (Figure 13b) or small (Figure 13e). We conclude that the majority of ion target flux derives from ionisation within the divertor, in agreement with the self-contained divertor approximation (Eq. 8), which shows that TCV is operating under ‘high recycling’ conditions. These measurements also indicate that the additional source from ion flux into the divertor from the SOL should be either relatively small or balanced by the ion flux flowing from the outer divertor towards the inner target.

High recycling divertor operation has been illustrated as a narrow ionisation region in front of the target [4]. This contrasts with our TCV observation. The difference in ionisation layer size is likely due to the large mean free path of ionisation on TCV (5-10 cm). This indicates that having a narrow ionisation region may not be necessarily a requirement for cases where Eq. 8 applies.

The various ion losses for the density ramp cases can be compared quantitatively by assuming that both the ion target flux and  $I_i$  should increase linearly with time for the density ramp discharges (red dashed lines Figure 13b, e). The losses are then calculated by subtracting the measured  $I_t$  and  $I_i$  from these respective linear scalings. The measured target ion current loss and the ionization source loss track well within uncertainties for both density ramp cases (Figures 13c, f). The recombination ion sink is only significant at the end of the high plasma current discharge; it only starts to develop to significant levels after the ion target flux roll-over and long after the deviation of the measured  $I_t$  from its linear (attached) scaling and it remains more than a factor 4 lower than the loss of target ion current or loss of ionization source.

There is a clear difference in the role volumetric recombination plays between the low and high current cases. This is an interesting observation, as it suggests that (for the same core Greenwald

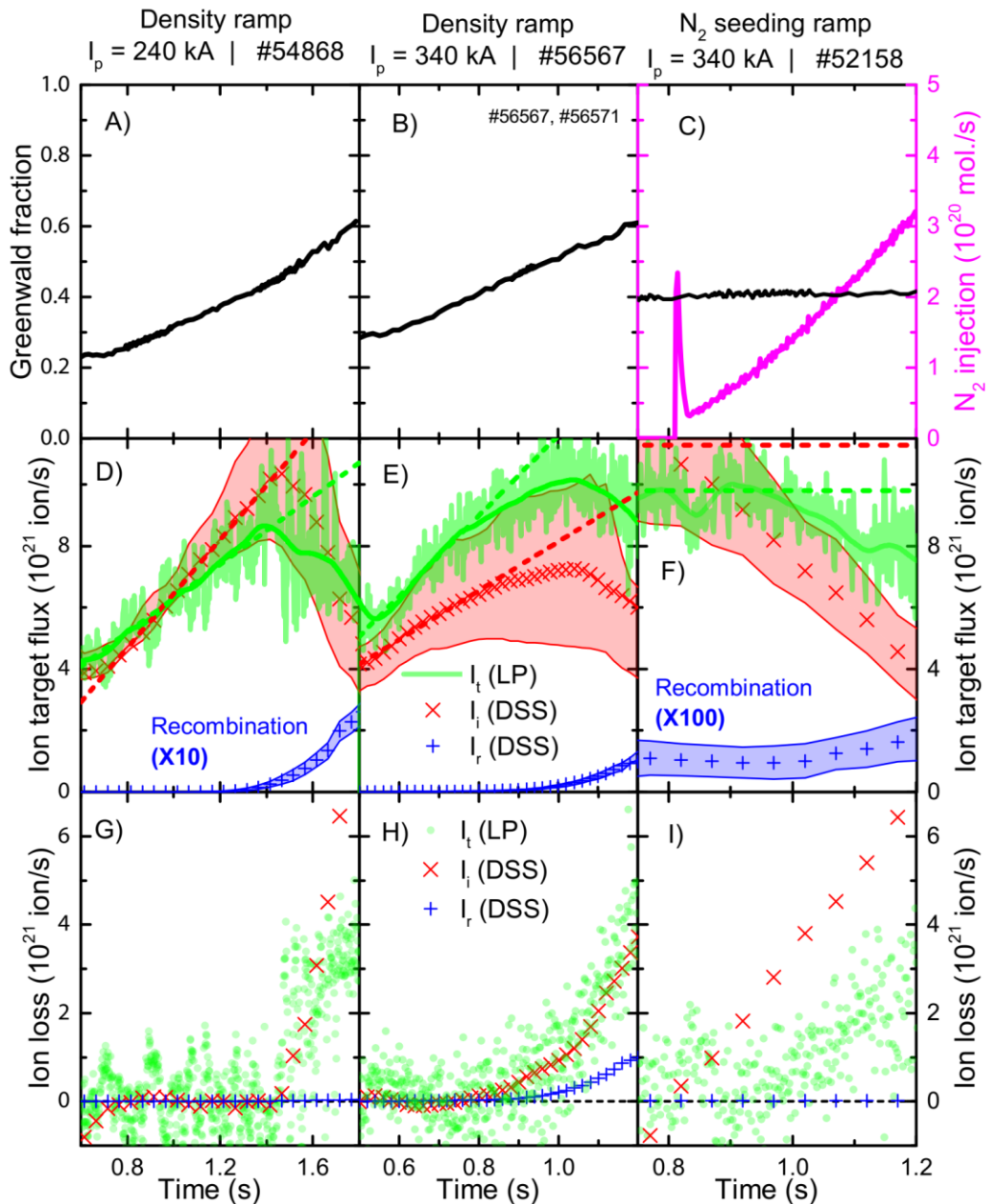


Figure 13 – First two columns correspond to core density ramps at two different plasma currents: Core Greenwald fraction (a,b); divertor ion sources/sinks and ion target flux (d, e) as well as the loss of ion target current, recombination sink and loss of ionization (g, h). The last column corresponds to a  $N_2$  seeding ramp at constant core density (c): divertor ion source/sink and ion target flux (f) as well as the loss of ion target current, recombination sink and loss of ionization (i).

fraction) the plasma current is a ‘control knob’ for the influence of recombination on the ion target flux. The recombination rate in the high current case is 5-10 times higher at the same core Greenwald fraction, whereas the ion target flux is only  $\sim 25\%$  higher. One explanation for the higher recombination rates is that the  $\sim 1.5$  x higher  $n_{eu}$  leads to higher divertor densities. These are observed (Stark density) to be  $\sim 3$  x higher for the high current case, which agrees with the expected strong dependence of the divertor density on  $n_{eu}$  (cubic, based on the two point model [4]).

Assuming identical divertor temperatures between the two cases, this would result in  $x \sim 10$  times higher recombination rates (estimated from ADAS tables [45, 46]).

#### 4.2.2 Characterization of ion sinks and sources in $N_2$ -seeded discharges

$N_2$  seeded discharges develop significantly differently than the core density ramp discharges discussed previously. The line averaged density for this pulse (Figure 13g) is held constant over the  $N_2$ -seeding ramp at a Greenwald fraction of  $\sim 0.4$ . This is just below the core density at which the ion target flux roll-over occurred in the equivalent high current, density ramp discharge (pulse #56567; Figure 13 d-f). The ion target loss is quantified as previously using the pre- $N_2$  seeding scaling as a reference. This likely underestimates the actual value of the ion target loss as in attached conditions the ion target flux is expected to increase if impurity radiation in the divertor is altered while other divertor parameters are kept constant (equation A.8). The magnitude of the ion source loss, including the range of uncertainty, was larger than that needed to explain the magnitude of the ion target flux.

We can only speculate as to why the particle balance between sinks and sources is not as consistent for the case of  $N_2$ -seeding. One possible explanation is that a significant fraction of the target ion current was carried by nitrogen ions, thus contributing a significant fraction of the ion target current. To explain the mismatch between the ion target flux and the ionisation source prediction, a nitrogen concentration of 10 - 25% would suffice assuming an average nitrogen ion charge of 2. A crude analysis, using Open-ADAS photon emission coefficients together with the NII (399.6 nm) line brightness measured by the DSS and  $(T_e^E, n_e, \Delta L)$  obtained from the Balmer line analysis, indicates the ratio between the  $N^+$  density and  $n_e$  is larger than 4%. The total nitrogen concentration is likely significantly higher than the  $N^+$  concentration: to illustrate, for a transport-less plasma – which is not valid here – one would expect a fractional abundance of  $N^+$  smaller than 0.1 for the values for  $T_e^E$  obtained). This crude analysis is consistent with the explanation of a significant portion of the ion target current being due to nitrogen ions, but does not constitute a proof. A proof would require a more quantitative and complicated analysis as in [63].

#### 4.3 Power balance in the divertor and relationship to ionization

We have now described all the elements in divertor particle balance using our estimations of the ionization source in combination with the ion sinks at the target and in the plasma. The divertor ion source is approximately equal to the target ion current; this suggests that the divertor ion source,  $I_i$ , is the main determinant of the ion target flux from a particle balance point of view (remembering that  $p_t$  must also drop). We have not addressed the question as to what causes the ionization source to decrease. It has been suggested previously, both experimentally [7] and theoretically [9, 10, 29] that the ion source can be limited by the amount of power available for ionization in the divertor. To pursue this question, we now develop a power balance analysis and apply it to the outer divertor for one of the discharges shown in Figure 13, #56567.

The power entering the divertor,  $P_{div}$ , is lost partially due to radiation,  $P_{rad}$ , after which the remaining power ends up at the target ( $P_{target}$ ), both in the form of potential energy,  $P_{target}^{pot} = I_t \epsilon$  and kinetic energy,  $P_{target}^{kin} = I_t \gamma T_t$ , where  $\gamma \sim 7$  is the sheath transmission factor. This is shown in Eq. 9, where  $\epsilon = 13.6$  eV is the potential energy and again the molecular dissociation potential of 2.2 eV [1] is neglected.

$$P_{div} - P_{rad} = P_{target} = I_t(\gamma T_t + \epsilon) \quad (9)$$

The radiated power highlighted in Eq. 8 can be split into different portions: hydrogenic radiation and impurity radiation. Hydrogenic radiation has both an excitation ( $P_{rad}^{H,exc}$ ) and a recombination ( $P_{rad}^{H,rec}$ ) contribution. The split of radiated power is

$$P_{div} - P_{rad}^{H,exc} - P_{rad}^{H,rec} - P_{rad}^{imp} = I_t(\gamma T_t + \epsilon) \quad (10)$$

To obtain further insight into the power loss processes, we can re-arrange Eq. 10 by bringing the potential energy of the ions reaching the target to the other side of the equation and utilising the closed box approximation (Eq. 8):

$$(P_{div} - P_{rad}^{imp}) - (P_{rad}^{H,exc} + \epsilon I_i) - (P_{rad}^{H,rec} - \epsilon I_r) = I_t \gamma T_t \quad (11)$$

We have already grouped several terms for explaining the processes in divertor power balance, which are schematically shown in Figure 14. Note that the different regions in Figure 14 spatially overlap as shown in section 4.1.2 (Figure 11). This analysis, however, does not rely on such a separation and the regions shown in Figure 14 are only intended to serve as a visualisation aid.

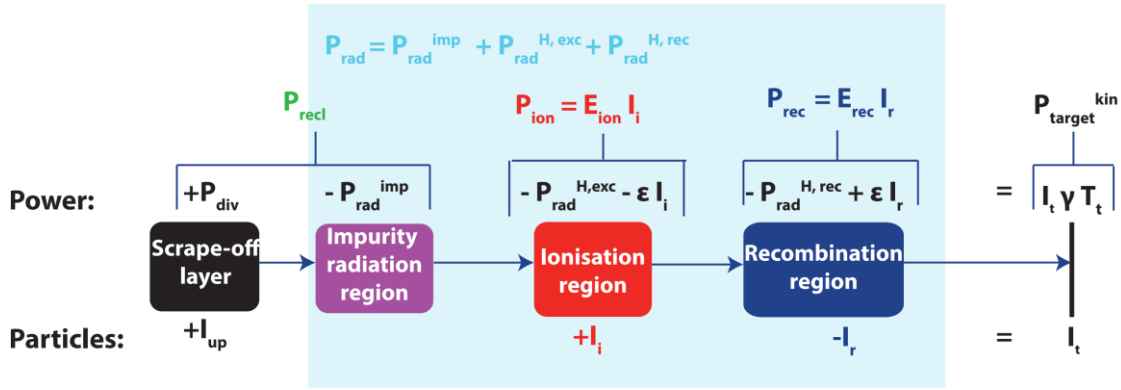


Figure 14: Schematic overview of power and particle balance in the outer divertor. The blue shaded region represents the divertor. The top line describes power balance in terms of power entering the divertor ( $P_{div}$ ), impurity radiation ( $P_{rad}^{imp}$ ), power reaching the recycling/ionisation region ( $P_{recl}$ ), ionisation power cost ( $P_{ion}$ ) and recombination power cost ( $P_{rec}$ ), eventually resulting in kinetic power reaching the target ( $P_{target}^{kin}$ ). The bottom line in the figure describes particles (ion) balance in terms of an ion flow from upstream ( $I_{up}$ ), ions generated in the ionisation region ( $I_i$ ) and ions being removed in the recombination region ( $I_r$ ), eventually leading to  $I_t$  ions reaching the target.

The power flow into the divertor,  $P_{div}$ , is first reduced through divertor impurity radiation by an amount  $P_{rad}^{imp}$ . We define  $P_{recl}$  as the power which enters the recycling region (Eq. 12).

$$P_{recl} = P_{div} - P_{rad}^{imp} \quad (12)$$

While we include the effects of ionization in the power balance of the recycling region we ignore, for simplicity, energy losses due to charge exchange (CX). While the CX energy losses have been estimated per ionisation event ( $\sim 3-5$  eV [9]), higher estimates for TCV parameters (5-15 eV [64]) are obtained by [13, 64]. In either case, as a sink or source of energy, the CX effect is difficult to quantify for a simple model and we do not include it in the following. However, preliminary results from SOLPS simulations [27] indicate that CX related power losses are secondary to impurity and hydrogenic radiation.

As explained previously in section 3.3, power is lost in the ionisation region due to excitation collisions preceding ionisation, leading to radiation losses ( $P_{rad}^{H,exc}$ ) as well as to the potential energy conversion  $\epsilon$  required for ionisation. The total ionization power loss is then provided by Eq. 13. Dividing the total ionisation power loss by the total ionisation source leads to an effective ionisation

energy loss,  $E_{ion}$  (Eq. 14), which is an important parameter in modelling the ion target current dynamics as will be discussed in section 5.1 and 5.2.

$$P_{ion} = P_{rad}^{H,exc} + \epsilon I_i \quad (13)$$

$$E_{ion} = \frac{P_{ion}}{I_i} = \frac{P_{rad}^{H,exc}}{I_i} + \epsilon \quad (14)$$

There are both energy gains and losses in the recombination process. Recombining ions can release their potential energy ( $\epsilon = 13.6$  eV) back to the plasma. But, in addition, recombination leads to radiation losses,  $P_{rad}^{H,rec}$ , which takes all forms of recombination (radiative and three-body) into account. The total power ‘cost’ of the recombination region ( $P_{rec}$ ) is thus given by Eq. 15, which is similar to how the power loss/gain due to recombination in [65] was determined.

$$P_{rec} = P_{rad}^{H,rec} - \epsilon I_r \quad (15)$$

Note that if  $\epsilon I_r > P_{rad}^{H,rec}$ ,  $P_{rec}$  will be negative and recombination will lead to a net plasma heating. Generally, recombinative plasma heating will occur when a significant portion of recombination is three-body recombination [4], which is more likely at higher electron densities and lower electron temperatures. In any case, the value of  $P_{rec}$  on TCV is small, whether slightly positive or negative (see section 5.1.3).

We now rewrite Eq. 11 using the definitions of Eqs. 12-15, to better visualise power balance in the recycling region and what reaches the target:

$$P_{recl} - P_{ion} - P_{rec} = P_{target}^{kin} \quad (16)$$

As  $P_{recl}$  is lowered through impurity radiation (while keeping  $P_{div}$  constant), a point can be reached where  $P_{recl}$  limits the power needed for ionization,  $P_{ion}$ . The ionization source,  $I_i$ , would then be reduced, sometimes called a form of ‘power starvation’. A reduction of the ion source leads to less ions entering the recombination region (where more losses can occur) and thus a reduced target current,  $I_t$ . As part of this process the temperature near the target drops, making that region conducive to recombination and ion-neutral collisions which are related to momentum loss processes. One could imagine that the target ion current controls the upstream ion source as neutrals created at the target are needed for ionization upstream [9, 10, 13]. However, if  $P_{recl}$  is not large enough to ionize all those neutrals then they would accumulate. This appears to be the case as the target ion current is strongly reduced in detachment. The divertor neutral pressure stays high and even increases while the ion source is decreasing [66, 67]. This is observed during TCV detachment using baratron neutral pressure measurements [58] of the discharges discussed and is supported by SOLPS simulations [27], which indicate that the averaged neutral density over the DSS chords (weighted by the excitation emission profile), as well as neutral pressures obtained in the simulation, increase during detachment while the neutral fraction remains roughly constant.

To utilize the divertor power balance structure described above we also need to explain how the various parameters are obtained experimentally. First, we start with determining the power flowing into the Scrape-Off Layer (SOL) from the core plasma,  $P_{SOL}$ . Since the discharges included in this study are Ohmically heated ( $P_{Ohm}$ ),  $P_{SOL}$  is obtained by subtracting the core radiated power ( $P_{rad}^{core}$ ), measured by foil-bolometer arrays (see section 2), from  $P_{Ohm}$ . The power flowing to the outer divertor is  $P_{div} = \alpha P_{SOL}$ , where  $\alpha$  denotes the fraction of  $P_{SOL}$  flowing to the outer divertor. We follow a previous study [26] which found  $\alpha \sim 0.5$  for the plasma conditions (flux expansion; plasma current) of #56567.

$$P_{div} = \alpha(P_{Ohm} - P_{rad}^{core}) \quad (17)$$



To obtain  $P_{recl}$ , first we need to estimate  $P_{rad}^{imp}$ , which requires separating out the impurity radiation from the hydrogenic radiation. Using Eq. 10, this can be done by obtaining the divertor radiation,  $P_{rad}$ , from bolometry while estimating both the hydrogenic radiation ( $P_{rad}^{H,exc}$ ,  $P_{rad}^{H,rec}$ ) and  $P_{ion}$ ,  $P_{rec}$  through spectroscopic means (section 3.3).

$$P_{rad}^{imp} = P_{rad} - P_{rad}^{H,exc} - P_{rad}^{H,rec} \quad (18)$$

Figure 15 displays the result of our derivation of the various power channels for #56567; similar qualitative trends are found for the other two discharges presented in section 4.2. We include again the measurements of the target ion flux and the ionisation source (Figure 15a) along with the various divertor-integrated, power losses (Figure 15b). Impurity radiation is dominant (x 4) over  $P_{rad}^{H,exc}$  with recombination radiative losses essentially ignorable.

During the ramped increase of the core and edge density  $P_{recl}$  (Figure 15c) steadily drops while the power into the outer divertor,  $P_{div}$ , remains roughly constant. This suggests that, even in non-seeded density ramp discharges, impurity radiation due to intrinsic impurities (carbon in the case of TCV) plays a key role in reducing the power reaching the recycling region in TCV, hence enabling detachment. Near the time when the ion target flux slope in time becomes negative (roll-over,  $\sim 1.05s$ ),  $P_{recl}$  has dropped to roughly the amount of power expended for ionization,  $P_{ion}$ . This quantitative information suggests that the ion source is being limited by the power available,  $P_{recl}$ . When  $P_{recl}$  has dropped to roughly  $P_{ion}$ ,  $P_{target}^{kin} \ll P_{recl}$  – implying that low target temperatures are achieved as is expected from detachment and is observed (section 5.1.1). We note that  $P_{recl}$  is larger than  $P_{ion}$  when the target ion current deviates from the linear trend. This makes sense as some power, beyond ionization, is required to maintain a target temperature.

Figure 15d includes a check of the overall divertor power balance. The sum of the total radiated power and the power reaching the target,  $P_{rad} + P_{target}^{IR}$  (the latter term from IR measurements), is compared with the power flowing to the outer divertor region,  $P_{div}$ , and the two match within uncertainties, giving

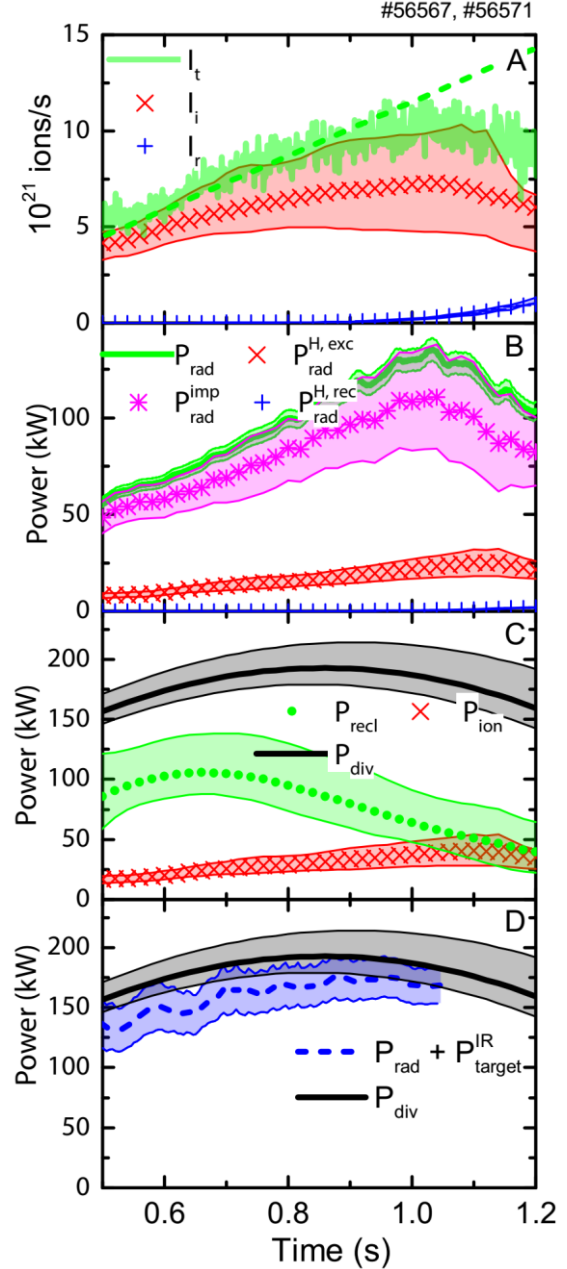


Figure 15: Power balance investigation for the outer divertor for pulse #56567 a) ion target flux, ionisation rate and recombination rate; b) break-down of total radiation and its contributors; c) comparison between power entering outer divertor leg,  $P_{div}$ , the power entering the recycling region,  $P_{recl}$ , and the power needed for ionisation,  $P_{ion}$ ; d) comparison between  $P_{div}$  and the outer divertor leg radiative losses plus the measured power deposited on the target by the IR for consistency.

confidence in the  $P_{div}$  determination. Note that  $P_{rad} + P_{target}^{IR}$  is no longer shown after 1.05 s due to failures in the IR background subtraction algorithm.

## 5. Discussion

The results shown in section 4 of this paper show a strong particle balance correlation, in magnitude and time dependence, between the ionization source and the target ion current. This implies the ion current roll-over occurs due to an ion source reduction as opposed to an ion sink. In section 4.3 we also calculate that the power required to supply the measured ionisation source is approximately equal to the power flowing into the recycling region ( $P_{recl}$ ); power limitation of the ionization source is occurring.  $P_{recl}$  is reduced through intrinsic impurity radiation in the divertor while the power entering the divertor remains roughly constant;

In the following discussion we utilize reduced analytic models to predict the target ion current (ion source) behaviour during detachment and the detachment threshold. These predictions are compared with observations and are used to investigate the relation between the target ion current and upstream parameters. Such reduced analytical models take the minimum number of necessary physical processes into account to model various detachment characteristics. In addition, the existence of other ion sources/sinks, apart from the ones treated in section 4, is also considered.

### 5.1 Investigating the ion target flux trends in the framework of power and particle balance

We now investigate the influence of ‘power limitation’ on the ion source more quantitatively by predicting the target ion source through its dependence on power and target temperature using power and particle balance [7,9] through the processes highlighted in Figure 14 & 15.

The target ion current,  $I_t$ , is calculated using Eq. 19, where  $P_{recl}$  and  $T_t$  are the independent, measured, variables. Eq. 19 is derived by combining the different power sinks presented in section 4.3 (Eqs. 11, 14) with the closed box approximation (Eq. 8). Though recombination is accounted for in particle balance, it is assumed that it is neither an energy sink nor an energy source (e.g.  $P_{rec} \sim 0$  in Eq. 14), which agrees with spectroscopic estimates (section 5.1.3). The predicted  $I_t$ , in this form, applies to the entire outer divertor, although this model is also applicable along a single flux tube (neglecting cross-field transport of particles and heat). Therefore  $T_t$ , the target temperature, in Eqs. 19, 20 is an effective averaged (weighted by the heat flux) target temperature [6], which is not necessarily representative of the peak temperature at the target.

$$I_t = \frac{P_{recl} - E_{ion} I_r}{E_{ion} + \gamma T_t} = \left( \frac{P_{recl}}{E_{ion}} - I_r \right) \times f_{ion}(T_t^*) \quad (19)$$

$$f_{ion}(T_t^*) = \frac{1}{1 + T_t^*} \quad (20)$$

$\frac{P_{recl}}{E_{ion}}$  represents the maximum ion source which could be achieved if all power entering the recycling region is spent on ionisation. In the absence of recombination<sup>2</sup>,  $f_{ion}(T_t^*)$  (Eq. 20) represents the

---

<sup>2</sup> Eq. 19 can be re-written  $I_t = \beta \times \frac{P_{recl}}{E_{ion}} \times \frac{1}{1 + T_t^{**}}$  in which  $\beta = \frac{I_t}{I_r}$  represents the fraction of ionised particles reaching the target and  $\frac{1}{1 + T_t^{**}}$  represents the fraction of  $P_{recl}$  spent on ionisation even if recombination is present, in which  $T_t^{**} = \beta \frac{\gamma T_t}{E_{ion}}$  represents the ratio between the kinetic power reaching the target and the power required for ionisation. For the case discussed,  $\beta > 0.85$  and hence can be neglected.

fraction of  $P_{recl}$  spent on ionisation, in which  $T_t^* = \frac{\gamma T_t}{E_{ion}}$  represents the ratio between kinetic power leaving the ionisation region (reaching the target) and power used for ionisation ( $\frac{\Gamma_t \gamma T_t}{\Gamma_t E_{ion}}$ ).

It should be clearly noted that since equation 19 requires  $T_t$  as an *input* (from a measurement): it does not take explicitly into account that changing the power entering the recycling region also influences the target temperature.

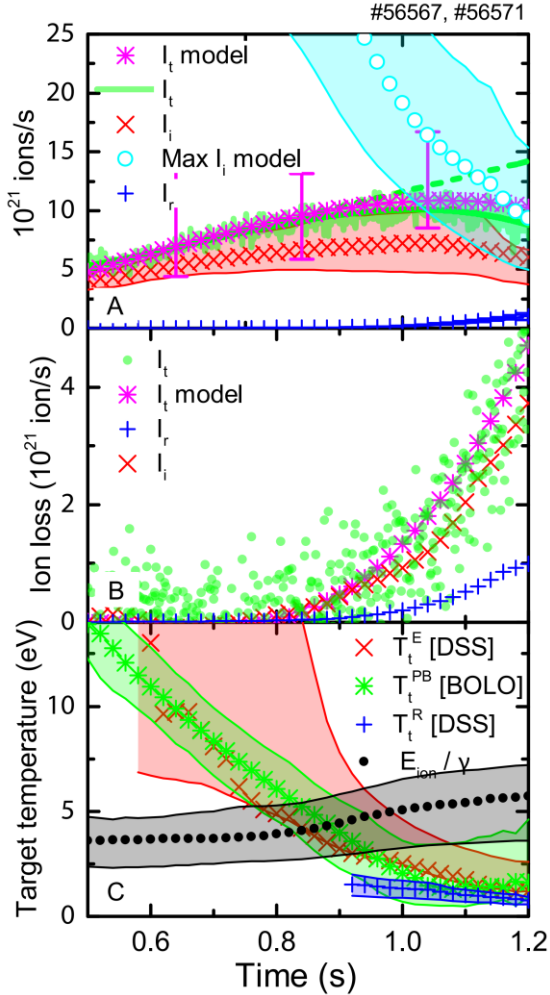


Figure 16: a) Predicted ion target flux based on power balance compared with measured ion target flux as function of time. b) Ion loss (similarly defined as in section 4.1) as function of time for the ion target flux prediction, ion source and the measured ion target flux. c) Target temperature as function of time. Pulse #56567.

### 5.1.1 Target temperature estimates

The ion target flux predictions, obtained using Eq. 19, require an estimate of the target temperature, or more specifically  $T_t^*$ . However, obtaining the target temperature during detached conditions is challenging as  $T_e$  measured by Langmuir probes (LP) is concluded to be often overestimated in detached low  $T_e$  conditions [39, 60, 61].

An estimate of  $T_t$  can be obtained spectroscopically from the line of sight closest to the target, which yields two different target temperatures (section 3.2): one target temperature characteristic for the recombinative region ( $T_t^R$ ) along the chordal integral and one target temperature characteristic for the excitation region ( $T_t^E$ ) along the chordal integral. Those are both likely an upper limit with respect to the actual target temperatures as the chord views the separatrix region at  $\sim 5$  cm above the target. As a consistency check, these spectroscopically-derived target temperatures are compared with a target temperature derived from power balance ( $T_t^{PB}$  – Eq. 21), which is obtained from Eq. 10. Since  $T_t^{PB}$  is obtained from the kinetic power reaching the target,  $T_t^{PB}$  can be regarded as a heat flux averaged target temperature.

$$T_t^{PB} = \frac{P_{div} - P_{rad}}{\gamma I_t} - \frac{\epsilon}{\gamma} \quad (21)$$

All three target temperature estimates show a decreasing trend as function of time, reaching target temperatures of 1-2 eV at the end of the discharge (Figure 16c).  $T_t^E$  and  $T_t^{PB}$  agree within uncertainty, whereas  $T_t^R$  (shown from 0.9 s onwards, since recombinative signatures are large enough to observe at this time) starts lower and decreases less strongly as function of time.  $T_t^R$  is likely lower as recombination-dominated emission increases strongly at low temperatures and is thus dominated by contributions from lower-temperature parts of the plasma along the line of sight. We utilize  $T_t^E$  in the following prediction of the target ion flux roll-over (equation 20). This is

appropriate as the excitation emission weighted temperature,  $T_t$ , is likely similar to the heat flux averaged temperature, as most excitation near the target occurs at the highest heat fluxes.

### 5.1.2 Comparing the measured and predicted ion target flux

Power and particle balances, as included in Eq. 19, provide a quantitative prediction of the target ion current behaviour through the attached and detached periods for pulse #56567, discussed earlier in section 4.2. This requires four input parameters:  $P_{recl}$  derived from subtracting impurity radiation losses from the power entering the outer divertor (Eq. 16, section 4.3),  $E_{ion}$  (Eq. 14, section 4.3),  $T_t$ , and  $I_r$  (section 4.1 - 4.2). All four are determined using spectroscopic inferences (section 3.2-3.3). The predicted ion target flux is in good agreement (in magnitude, trend and roll-over point) with experimental measurements of  $I_t$  (Figure 16a, b). This shows that the ion target flux can be described fully in terms of the maximum possible ion source,  $\frac{P_{recl}}{E_{ion}}$ , and the recombination sink,  $I_R$  once  $T_t^*$  is known.

The maximum ion source,  $\frac{P_{recl}}{E_{ion}}$ , is of order 2x the ion source,  $I_i$ , at detachment (e.g. deviation of ion current trend from its linear reference which coincides with the roll-over of the separatrix ion target current), which corresponds to  $f_{ion} \sim 0.5$ . This critical point  $f_{ion} = 0.5$  can also be written in terms of the target temperature (Eq. 20):  $T_t^* = 1 \rightarrow T_t = \frac{E_{ion}}{y}$ , which occurs when the black trend crosses the red trend in Figure 16c. This is consistent with the empirical detachment threshold found in section 4.3, figure 15.

In section 5.2 and A.4 we will introduce reduced analytical modelling based on the Two Point model [4, 8, 9] where hydrogenic recycling energy losses are included. In that more sophisticated formulation  $T_t$  is predicted and  $f_{ion} \sim 0.5$  is found to be a critical point, which represents a validity limit of the 2PMR without momentum loss terms [4, 8], which is interpreted by as a detachment threshold by Krasheninnikov [9, 10, 13]. More information on this point is provided in section 5.2 and A.4.

The dynamics of the target ion current described by Eq. 19 is a competition between two competing terms -  $\left(\frac{P_{recl}}{E_{ion}} - I_r\right)$  and  $f_{ion} \cdot \left(\frac{P_{recl}}{E_{ion}} - I_r\right)$  decreases during a density ramp while  $f_{ion}$  increases, driven

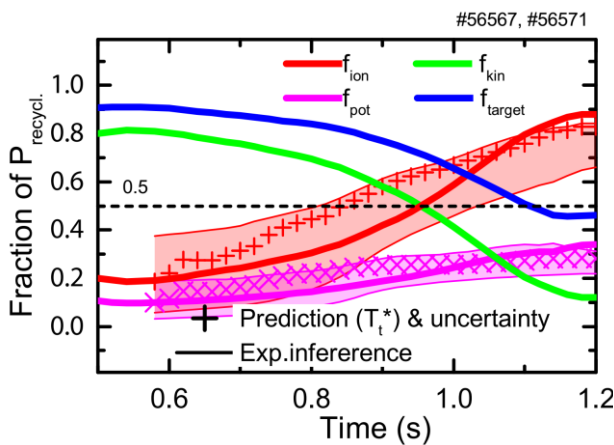


Figure 17: Break-down of the fraction of  $P_{recl}$  spent on ionisation; reaching the target; reaching the target in the form of potential energy and reaching the target in the form of kinetic energy. Both model predicted fractions (based on  $T_t^*$ ; Eqs. 19, 21, 22) and direct experimentally inferred fractions from power balance are compared.

by both the drop in  $T_t$  and increase in  $E_{ion}$ . The increase in  $f_{ion}$  is stronger in the period up to  $f_{ion} \sim 0.5$ , leading to a net increase in the target ion current before detachment. After detachment starts ( $f_{ion} > 0.5$ ), the increases in  $f_{ion}$ , which are small for  $T_t < 1$ , become insufficient to fully compensate the drop of  $\frac{P_{recl}}{E_{ion}}$  resulting in a flattening of  $I_t$ . As  $f_{ion} \sim 1$  is approached, the drop in  $P_{recl}$ , along with any recombination and increase in  $E_{ion}$ , results in an ion current roll-over as  $I_t \sim \left(\frac{P_{recl}}{E_{ion}} - I_r\right)$  (Eq. 19). This observation is *operationally sufficient* to state that the ion source is becoming limited by the amount of power flowing into the recycling region.

The trend in  $f_{ion}$  can be further

investigated for additional physical insight into the power dynamics of the recycling region. First, as shown in Eq. 20,  $f_{ion}$  can be predicted based on  $T_t^*$ .  $f_{ion}$  can also be inferred *directly* from the experimental spectroscopic observations and power balance as  $f_{ion} = P_{ion} / P_{recl}$ . The experimental inference (solid lines) agrees with the predicted  $f_{ion}$  (symbols) within uncertainty (Figure 17). Since  $f_{ion}$  is the fraction of  $P_{recl}$  spent on ionisation, we can also calculate the fraction of  $P_{recl}$  left after passing the ionisation region in the form of kinetic energy (Eq. 14), which drops from near 0.5 at the detachment onset, approaching 0 as  $f_{ion}$  increases, consistent with a temperature drop (Eq. 22).

$$f_{kin} = \frac{\gamma T_t}{\gamma T_t + E_{ion}} = 1 - f_{ion} = \frac{T_t^*}{T_t^* + 1} \quad (22)$$

The other fraction of  $P_{recl}$  which reaches the target is the potential energy spent on neutral  $\rightarrow$  ion conversion (ionization) in the recycling region ( $\epsilon I_i$ ). This power is stored and later released as either volumetric recombination (which also leads to radiation losses, similar to  $\epsilon$  per recombination event – section 5.1.3) or surface recombination at the target. Assuming volumetric recombination is negligible, the fraction of  $P_{recl}$  reaching the target through surface recombination is provided by Eq.

23. Again, this modelled  $f_{pot}$  can be compared with the directly estimated  $f_{pot} = \frac{P_{target}^{pot}}{P_{recl}} = \frac{I_t \epsilon}{P_{recl}}$ , see Figure 17.

$$f_{pot} = \frac{\epsilon / E_{ion}}{1 + T_t^*} \quad (23)$$

The fraction of  $P_{recl}$  deposited at the target is the sum of the kinetic and potential terms:  $f_{target} = f_{kin} + f_{pot}$ , which decreases as function of time (Figure 17) from 90% to 40% (Figure 17);  $f_{target}$  is never 1 due to the radiative power losses associated with excitation/ionization in the recycling region ( $P_{rad}^{H,exc}$ ). When  $f_{kin}$  approaches 0,  $f_{pot}$  becomes the lower limit for  $f_{target}$ , and thus the power reaching the target, can attain: for  $T_t^* \rightarrow 0$  and  $E_{ion} \sim 40$  eV,  $f_{target} \approx f_{pot} \sim 0.35$ . Volume recombination is required for a further reduction of  $f_{target}$ . Although a deviation of the target ion flux from the linear increase starts once  $f_{ion}$  becomes larger than 0.5, the target integrated ion current roll-over appears to start at higher  $f_{ion}$  where  $f_{pot}$  and  $f_{kin}$  are similar (Figure 17,  $\sim 1.05$ s); the kinetic energy of the ions reaching the target is comparable to the potential energy released at the target. That corresponds to a target temperature,  $T_t = \frac{\epsilon}{\gamma} \approx 2$  eV, based on Eq. 1.

### 5.1.3 The variation of $E_{ion}$ in detachment

In simple modelling, the amount of energy spent per ionisation,  $E_{ion}$ , is often assumed to be constant [4, 7, 9]. The excitation radiation component ( $\frac{P_{rad}^{H,exc}}{I_i}$ ) in  $E_{ion}$  (Eq. 14) is, however, strongly temperature dependant; as  $T_t$  is reduced, more excitations occur before an ionization happens. During the density ramp, the effective temperature in the ionisation region drops, leading to a factor of two rise in  $\frac{P_{rad}^{H,exc}}{I_i} = E_{ion} - \epsilon$ , the radiation cost of ionization (see Eq. 14 and Figure 18b), which results in a 50% increase in the divertor leg averaged  $E_{ion}$  (weighted by the ionisation rate).

The maximum ion source ( $\frac{P_{recl}}{E_{ion}}$ ) decreases  $\sim 30\%$  between  $t=1.0$  and  $t=1.25$  s, due to a  $\sim 10\%$  decrease in  $P_{recl}$  and a  $\sim 25\%$  increase in  $E_{ion}$ . Hence, arguably, even for the conditions shown, where the divertor radiation is dominated by impurity radiation, the increase in hydrogenic radiation leads to an increase in  $E_{ion}$  through a drop in the ionization region temperature. Thus, the increase in  $E_{ion}$  can play a significant role in limiting the number of ionizations (e.g. it further reduces the maximum ion source during the  $I_t$  roll-over).

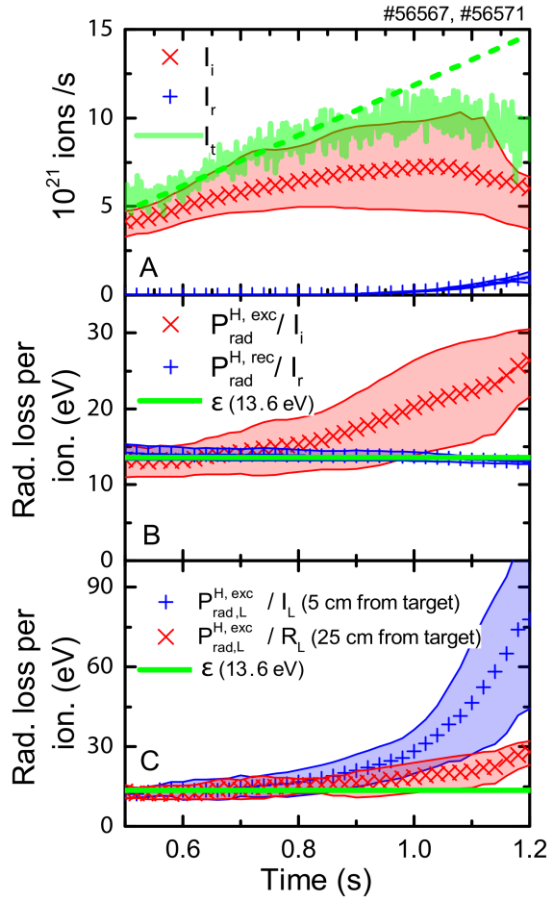


Figure 18: a) Target ion flux as function of time together with ionisation rate and recombination rate. b) Effective radiative energy cost per ionisation/recombination. c) Radiative energy cost per ionisation along a certain chord

recombination [8, 65]; as the plasma temperature and density vary the relative strength of two- and three-body recombination varies as well as the level of recombinative emission. For the TCV conditions investigated we find that the effective radiated energy loss per recombination event ( $\frac{P_{rad,L}^{H,rec}}{I_R}$  Figure 18b) is roughly equal to the potential energy. That is not surprising, considering the modest TCV densities: ADAS calculations indicate an effective heating of 0 – 1 eV per recombination reaction at  $T_e = 1$  eV for  $n_e$  in between  $10^{18} - 10^{20} \text{ m}^{-3}$ , using a similar calculation as done in [65] (e.g.  $P_{rec}$  in eq. 15 divided by  $R_L$ ). Hence, volumetric recombination does not lead to significant plasma heating or cooling for the TCV conditions presented.

## 5.2 Investigating the target ion flux trends in the framework of momentum balance

In the previous section we have investigated the target ion flux trend in the framework of power and particle balance of the entire SOL. In this section, we add momentum (pressure) balance [4, 8] to the power/particle balance analysis of section 5.1 such that the target temperature is now *predicted* instead of *set* by measurements. This enables a single flux tube comparison of the observed detachment dynamics and onset with additional predictions from simplified analytical theory; the preceding work has all been for the *entire* outer divertor. In this discussion, only the electron

We also investigate the divertor profile of the excitation cost of ionization ( $E_{ion} - \epsilon$ ) along different viewing chords,  $\frac{P_{rad,L}^{H,exc}}{I_L}$ . Since the number of excitation events required per ionization rises strongly at low temperatures ( $\sim 2$  eV), poloidal temperature gradients lead to strong variations of  $\frac{P_{rad,L}^{H,exc}}{I_L}$  along the divertor leg as shown in Figure 18C. In the region close to the target  $\frac{P_{rad,L}^{H,exc}}{I_L}$  increases up to 80 eV. In hotter regions of the divertor leg (chords further away from the target), where most of the ionisations take place (Figure 18b, c), the excitation radiation cost per ionization is 15-30 eV. Thus, variations in geometry (e.g. closed vs open divertor, vertical- vs horizontal-target), which lead to variations in recycling and neutral penetration, could influence the location of the ionisation region and thus could affect the dynamics of the target ion current loss through a change of  $E_{ion}$ , amongst other changes.

Whether recombination can heat or cool the divertor plasma is determined by the competition between the energy loss due to recombinative radiation and the potential energy released back to the plasma upon

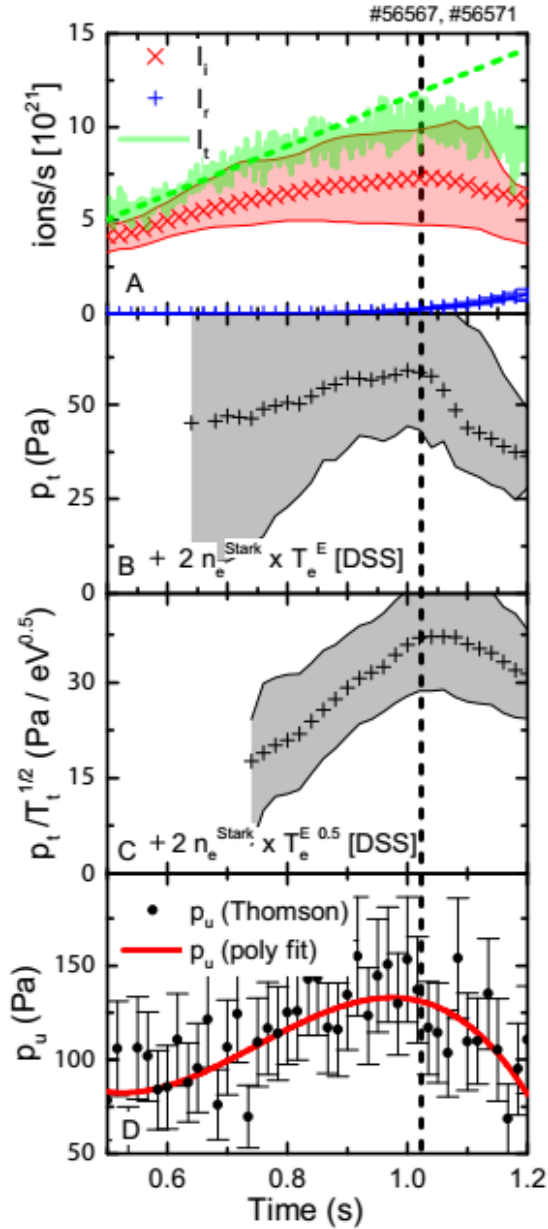


Figure 19: Comparison of target pressure and upstream pressure. a) reference total current to the target, total ionization source and recombination sink; b-c) Target separatrix pressure ( $p_t$ ) and ( $p_t / T_t^{1/2}$ ) ratio based on spectroscopic measurements (Stark broadening + excitation temperature of the chord closes to the target); d) Upstream separatrix pressure from Thomson scattering.

extensively in [8]. See appendix A.4 for a full derivation and in A.5 we demonstrate how we apply and evaluate the 2PMR. Our first goal of the application of the 2PMR is to verify the *expected* ion target flux trend in *attached* conditions. For this, pressure constancy along a flux tube is assumed and since  $p_u$  is a set *input* to the 2PMR, the target pressure  $p_t$  is fixed as well. Under such conditions the 2PMR provides two possible solutions: one stable and one unstable. We assume in the following (section 5.2.1, 5.2.2) that the unstable solution *cannot* occur.

pressure is considered and the mentioned target pressure  $p_t$  is the total target pressure (e.g. twice the kinetic target pressure).

Trends in target ( $p_t$ ) and upstream ( $p_u$ ) electron pressure are compared in Figure 19. By assuming  $p_t \sim p_u$  before detachment,  $p_t$  appears to be significantly underestimated by  $\sim \times 2$ . Synthetic diagnostics through SOLPS (appendix A1) indicate that this difference is due to chordal-average nature of the spectroscopically estimated target pressure. Both the upstream and target pressure are observed to roll-over at the target ion flux roll-over (Figure 19b, d). The upstream density saturates simultaneous with a roll-over in the upstream pressure, while the upstream temperature drops (Figure 10). As discussed in the Introduction (Eq. 2), at any point during the discharge, the target ion flux scaling can be written as  $\Gamma_t \propto p_t / T_t^{0.5}$ , i.e. the target plasma pressure must drop faster than  $T_t^{0.5}$  at the target ion flux roll-over. This is approximately observed (Figure 19 c). Following the discussion in section 5.1 (eqs. 19, 20), the target ion flux scaling (eq. 2) links the trend in the ionisation source (eq. 19) to the trend in the target pressure (eq. 2) and is thus crucial for understanding the complex interplay between momentum balance and ionisation balance.

### 5.2.1 Modelling total target ion current behaviour with both power and momentum balance

We utilise a ‘two point’ divertor model [4], which accounts for hydrogen recycling energy losses, to model the total target ion current. We refer to this as the ‘2PMR’, discussed previously in literature [4, 9] and more

The 2PMR yields a relation for the target temperature (Appendix A.4 Eq. A.5) as a function of  $E_{ion}$  and  $\frac{p_u}{q_{recl}}$  [4, 8, 9]. We obtain the flux tube specific  $q_{recl}$  from  $P_{recl}$  (which is for the entire outer divertor) by using the IR heat flux profile (see appendix A.5). The 2PMR-predicted  $T_t$  can be used to predict the target ion flux density ( $\Gamma_t$  in ion/s m<sup>2</sup>) on a *single* flux tube, as shown in Eq. 24 (Appendix A.4 Eq. A.8). It is important to note that the 2PMR  $\Gamma_t$  relation (Eq. 24a) is *identical* to the flux surface equivalent of Eq. 18 (while using the 2PMR predicted  $T_t$ ) (Appendix A.4), which is shown in equation 24b as a reference to the reader. The 2PMR thus connects the standard two-point divertor model with the power/particle balance model discussed in section 5.1. Here  $f_{ion}\left(T_t(E_{ion}, \frac{p_u}{q_{recl}})\right)$  denotes that  $f_{ion}$  (or  $f_{kin}$ ) is a function of  $T_t$ , which is a function of  $E_{ion}$  and  $p_u/q_{recl}$  (assuming pressure balance) – as discussed in appendix A.4.

$$\Gamma_t = \frac{\gamma p_u^2}{2 m_i q_{recl} f_{kin}\left(T_t(E_{ion}, \frac{p_u}{q_{recl}})\right)} \quad (24a)$$

$$\Gamma_t = \frac{q_{recl}}{E_{ion}} \times f_{ion}\left(T_t(E_{ion}, \frac{p_u}{q_{recl}})\right) \quad (24b)$$

To compare the experimental measurement of the *total* target ion current  $I_t$  (as opposed to  $\Gamma_t$ ) to the 2PMR, we integrate  $\Gamma_t$  across the SOL.  $I_t$  can then be modelled using  $\frac{p_u^2}{P_{recl}}$ ,  $f_{kin}(T_t)$  (eq. 14) and  $f_p$  (parametrising the geometric dependence of SOL profiles, which describes the influence of upstream pressure/target heat flux profiles on  $I_t$ ; see appendix A.5 Eq. A.21), based on  $T_t$  predicted by the 2PMR (eq. A.10 of appendix A.4). More information is provided in appendix A.5.

$$I_t \propto \frac{f_p}{f_{kin}\left(T_t(E_{ion}, \frac{p_u}{q_{recl}})\right)} \frac{p_u^2}{P_{recl}} \quad (25)$$

The predicted target ion flux trend described by Eq. 25 is similar to the measured target flux in the attached phase as shown in Figure 20a, showing a clear linear increase as function of time (and thus upstream density – section 4.1.1). Hence, simply using  $I_t \propto n_{e,u}^2$ , on which the ‘‘Degree of Detachment’’ [6], a parameter often used to investigate the ‘depth’ of detachment [19, 58], is based, is not appropriate for the TCV density ramp discharges studied, and should generally be used more carefully. In fact, from a 2PMR point of view, if  $T_u$ ,  $q_{recl}$ ,  $E_{ion}$  are held constant and only the upstream density is increased, a different scaling than  $\Gamma_t \propto n_{e,u}^2$  is expected (Eq. 23) as higher upstream densities will decrease the target temperature which will increase the power flux fraction required for ionisation, reducing  $q_t = q_{recl} f_{kin}$  in the process. In Eq. 24, the main influence on  $I_t$  is  $\frac{p_u^2}{P_{recl}}$  (see Figure 20b for all the terms). This basic scaling (or  $\Gamma_t \propto \frac{p_u^2}{q_{recl}}$ ) scaling not only arises from the 2PMR, but can also be obtained from pressure balance ( $n_u T_u = 2n_t T_t$ ), the sheath target equation ( $q_t \propto n_t T_t^{3/2}$ ) and an equation for the target heat flux ( $q_t = \Gamma_t T_t$ ). This results in  $\Gamma_t \propto \frac{n_u^2 T_u^2}{q_t}$  (equivalent to equation 5.13 in [4] of the basic two point model), providing an identical relation for the target ion flux as equation 24a. Additionally, the  $\Gamma_t \propto \frac{n_u^2 T_u^2}{q_t}$  scaling is also equivalent to the relation used in [6] for defining the degree of detachment originally (which is obtained by using equations 3,4,8 in [6]).

Since  $I_t \propto \frac{p_u^2}{P_{recl}}$  increases linearly as  $n_u$ ,  $\frac{T_u^2}{P_{recl}}$  must decrease roughly as  $1/n_u$ . Given that  $P_{recl}$  decreases during the density ramp (section 5.3),  $T_u$  (Figure 10a, section 4.1) must decrease more strongly to give this scaling. As  $P_{div}$  is roughly constant throughout the discharge (Figure 15) a decrease of  $T_u$



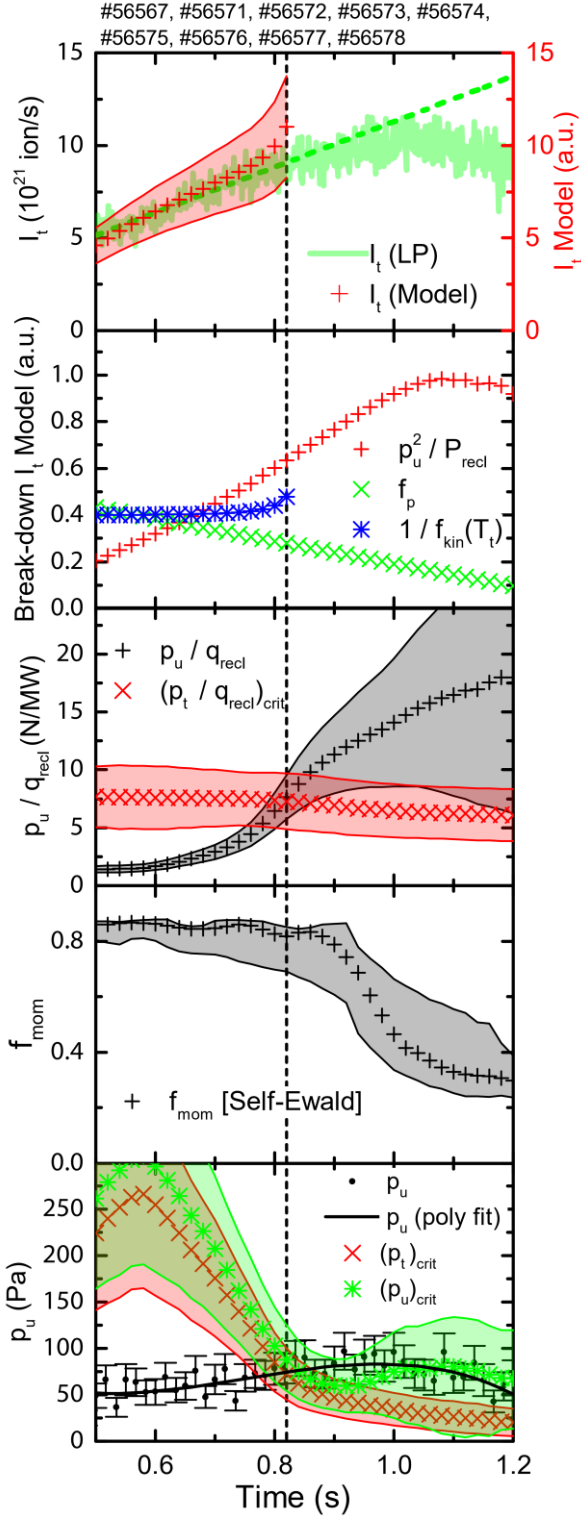


Figure 20: a) Measured and predicted target ion flux trend. b) Break-down of the contributors to the predicted ion flux. c) Measured  $p_{up} / q_{recycl}$  compared to the critical predicted level. d) Inferred momentum losses from spectroscopic estimates. e) Measured upstream pressure compared to critical pressure level with and without momentum losses.

could result from SOL broadening (which is measured by IR thermography to increase [42] by over a factor 3 until detachment is reached for the discharge shown). Alternatively, the decrease of  $T_u$  could be due to an increase in convective over conduction parallel heat transport [4].

A previous TCV study concluded that the observed linear trend of  $I_t$  with  $\bar{n}_e$  on TCV indicated that the divertor plasma was in a low-recycling operation [30]. However, given our measurements that the target ion current agrees with the ionisation source (section 4.2) and that  $I_t$  is properly predicted by the 2PMR (which assumes that all target ion current is due to divertor ionisation) is more consistent with characterizing the divertor as high-recycling.

### 5.2.2 Detachment thresholds and implications for momentum/pressure losses along a flux tube (separatrix)

As shown in Figure 20a, the 2PMR (which assumes both constant pressure along the field line and a prescribed upstream pressure), the  $I_t$  estimate can only be made until 0.8 s, at which time the 2PMR, under these assumptions, reaches a ‘hard’ critical limit (appendix A.4 Eqs. A5-A6) before the ion target flux roll-over.,

It is evident from Eq. 2 that the ion current roll-over, together with a fixed/decreasing target temperature, *must* be accompanied by *target pressure loss* ( $p_t \propto \Gamma_t T_t^{1/2}$ ). The power and particle balance model discussed in section 5.1 (eqs 19,20), indicates that  $\Gamma_t$  is a function of  $T_t$  as there is a trade-off using power for ionisation and the power flowing to the target denoted by  $f_{ion}$  – eq. 20. This has two implications: 1) the target pressure cannot be increased indefinitely, and a maximum exists ( $p_{t,crit} = \frac{q_{recl}}{2\gamma c_s(T_t = \frac{E_{ion}}{\gamma})}$ ), 2) this

maximum is reached at a certain threshold ( $T_t < \frac{E_{ion}}{\gamma}$ ) where further decreases in  $T_t$  lead to a

smaller increase in  $\Gamma_t$  as the decrease in  $T_t^{1/2}$ . That critical maximum target pressure (or threshold) is reached at 0.8 s, after which the target pressure must reduce as  $\Gamma_t$  rises slower than  $T_t^{1/2}$  drops, corresponding to the deviation of the ion current from its linear (attached) trend. Going beyond this point is not allowed by the model assumptions of a fixed  $p_u$  and constant pressure along the field lines. It is thus not surprising that the 2PMR, under these assumptions, cannot model the ion current roll-over and thus only applies to *attached* conditions.

This above threshold of the 2PMR model where the target pressure is maximised and target pressure loss is necessary as  $\Gamma_t$  ( $T_t$ ) starts to rise slower than  $T_t^{1/2}$  (Eq. 19,20) has been suggested by Krasheninnikov [9, 13] to be a ‘detachment onset criterium’: for target temperatures below this limit insufficient power is transferred beyond the ionisation region to sustain a sufficiently high target temperature for the target pressure (which is collapsing) to match the upstream pressure. Stangeby, although not calling the above limits a detachment threshold, argues properly that to reach  $T_t < E_{ion}/\gamma$ , processes which continuously lower the target pressure as the target temperature becomes lower (e.g. the target pressure must be a specific function of the target temperature) is required [4, 8]. This can be achieved by volumetric momentum losses (as shown explicitly in [8]) and/or by assuming  $p_u$  drops as function of  $T_t$ . See appendix A.4.1 and [62] for more information.

These ‘detachment thresholds’ can be written in three different forms, given by Eq. 27. We have found thresholds 27b,c experimentally (section 4.3, 5.1, figures 15,16) to be empirical thresholds for detachment. A third (equivalent) threshold (eq. 27a) can be derived from the 2PMR (Appendix A4.1) [9] providing a critical maximum target pressure  $p_{t,crit} = \frac{q_{recl}}{2\gamma c_s(T_t = \frac{E_{ion}}{\gamma})}$ . Under the assumption of pressure balance, this is commonly written [4, 9] as a critical threshold for  $p_u / q_{recl}$ , above which  $p_u / q_{recl}$  cannot rise (Eq. 26a - assuming  $p_t = p_u$ ), where  $c_s$  is the target sound speed at  $T_t = \frac{E_{ion}}{\gamma}$ . ( $p_t / q_{recl}$ )<sub>crit</sub>, which applies to a flux tube – not the average over the divertor, is compared to the experimentally inferred  $p_u/q_{recl}$  in Figure 20c. The increase in  $p_u/q_{recl}$  is mostly ascribable to a drop in  $q_{recl}$  during the pulse.

$$\left(\frac{p_t}{q_{recl}}\right)_{crit} = \frac{1}{\gamma c_s(T_t = \frac{E_{ion}}{\gamma})} \quad (27a)$$

$$T_{t,crit} = \frac{E_{ion}}{\gamma} \quad (27b)$$

$$f_{ion} = \frac{1}{2} \quad (27c)$$

This third critical limit (27a), evaluated at the separatrix, is also reached at  $\sim 0.8$ s (Figure 20c), similar to the other detachment criteria ( $f_{ion} = 0.5$  (Figure 17),  $T_t = \frac{E_{ion}}{\gamma}$  (Figure 16c)) and when the integrated target ion current starts to flatten (deviate from the linearly increasing trend), the detachment process starts (Figure 10b). As discussed earlier, 0.8s also corresponds to where the separatrix current density starts to roll-over (Figure 10b); the relative roll-over times for the total and separatrix currents is not fixed – sometimes similar but, more often, the total current roll-over time is later [58].

### 5.2.3 The 2PMR and pressure losses

We see, however, that the observed  $p_u/q_{recl}$  rises above the  $(p_t/q_{recl})_{crit}$  threshold, which could be ascribed to volumetric momentum losses causing a bifurcation between  $p_u$  and  $p_t$ . Defining momentum loss by  $p_u f_{mom} \equiv p_t$ , this would increase the effective  $p_u/q_{recl}$  limit by  $1/f_{mom}$  (eq. 28). Here we implicitly assumed that  $f_{mom}$  is a *fixed, given* value (for instance through measurements), instead of assuming a particular  $f_{mom}(T_t)$  dependence (see A.4 for more information). Introducing

momentum losses in this way does not enable  $T_t < \frac{E_{ion}}{\gamma}$ , but does enable an ion current roll-over. More details are provided in section A.4.

$$\left(\frac{p_u}{q_{recl}}\right)_{crit} = \frac{1}{f_{mom}} \left(\frac{p_t}{q_{recl}}\right)_{crit} = \frac{1}{f_{mom}\gamma c_s \left(T_t = \frac{E_{ion}}{\gamma}\right)} \quad (28)$$

From Eq. 28 we find that  $f_{mom}$  would need to start to decrease from 1 at the detachment criterion to  $\sim 0.4$  at the end of the discharge to match the measured  $p_u/q_{recl}$  (Figure 20c) to  $(p_u/q_{recl})_{crit}$  in the detached phase using eq. 28. Such momentum losses in the TCV divertor during similar experiments have been determined directly from upstream and target pressure measurements [68], implying momentum losses greater than 50%.

An independent estimate of the onset and magnitude of momentum losses based solely on the dominance of charge exchange over ionisation can be made using the well-documented Self-Ewald model [3, 69] (Eq. 18) which has been used in several other studies [3, 13, 69] where some supportive evidence was shown. Such an estimate assumes that the charge exchange rate equals the momentum loss rate: *e.g. each CX reaction leads to a complete loss of that ion's momentum*, almost certainly overestimating the CX momentum loss. Molecular-ion collisions are not included in the Self-Ewald model [69, 70], but are likely supplying the over-estimated CX momentum losses. Although the level of momentum loss due to molecules is unknown for TCV, we do know that molecules are present and undergoing reactions in the volume of TCV (section 5.3.2). Momentum loss can also occur due to recombination. From a simple SOL model [71] we have evaluated the reduction of  $f_{mom}$  due to recombination for the case studied and found it negligible (smaller than 1.5% – in agreement with results from [7]). With this caveat we integrate the spectroscopically-determined profile of charge-exchange and ionisation rates along the outer divertor leg (Figure 11e) to calculate the Self-Ewald  $f_{mom}$  as a function of time, Figure 20c. As shown in Figure 11e, charge exchange to ionisation ratios are higher near the target during detachment than elsewhere in the divertor which, in the Self-Ewald model, results in larger inferred momentum losses. Note that we use the local temperature (excitation), charge exchange and ionisation rate estimates obtained spectroscopically for each chord, instead of the target temperature (used in other studies) which we feel more accurately represents what is occurring; using the target temperature would have led to larger inferred momentum losses.

$$f_{mom} = 2 \left(\frac{\alpha}{\alpha+1}\right)^{\frac{\alpha+1}{2}} \quad (28)$$

$$\alpha = \frac{1}{1 + \frac{\int 2\pi r_i CX_L(r_i, z_i) dz}{\int 2\pi r_i I_L(r_i, z_i) dz}}$$

We utilise this approach as the relation between momentum loss and the target temperature is unknown for TCV, as opposed to a prescribed function  $f_{mom}(T_t)$  as used in [4, 8, 72]. Furthermore, SOLPS simulations for TCV indicate that volumetric pressure loss can occur in the volume of the divertor [27]; not just in front of the target as observed in simulations [72] for other machines, which may invalidate making  $f_{mom}$  a function of the target temperature.

Our estimate of  $f_{mom}$ , using the Self-Ewald model, drops from  $\sim 0.9$  to  $\sim 0.3$  ([0.2 – 0.4] with uncertainty) is shown in Figure 20c, in agreement with the momentum losses obtained experimentally [68] and with the  $f_{mom}$  required to explain the increase of  $p_u/q_{recl}$  beyond the  $p_t/q_{recl}$  limit discussed above. This may be a coincidence – as mentioned above, the reality of CX collisions

not carrying away 100% of the ion momentum may be compensated by ion-molecule collisions (not included) carrying that momentum away [70, 72].

#### 5.2.4 The case for divertor processes reducing the upstream pressure and density

The results of the previous section show that the rise of  $p_u/q_{recl}$  beyond its critical  $p_t/q_{recl}$  limit can be attributed, at least partially, to momentum losses. However,  $p_u$  also drops during the detached phase, which will be investigated here further together with the role it plays in matching  $p_u/q_{recl}$  to its critical threshold (Eq. 27). The question of what leads to the drop in upstream pressure (and density) during detachment has been discussed by several authors of analytic and modelling studies [9, 10, 12].

Recombination has been predicted to lead to saturation of the upstream density when its rate approaches the ionization rate in a flux tube through a feedback loop [73]: as  $n_u$  increases, the divertor cools further, hence augmenting the recombination sink and moving the recombination region further towards the x-point, potentially impeding a rise in  $n_u$  [73]. This is not the case for these TCV discharges as recombination remains low and can be negligible. In addition, the recombination region peak does not move far off the target (section 4.1, 4.2, [26]).

Krasheninnikov [9] offers another explanation for saturation of the upstream density. During detachment, insufficient momentum losses along flux tubes can constrain, or pull down the upstream pressure. It is important to reiterate that, although an  $I_t$  roll-over requires a *target pressure* drop which increases faster than  $T_t^{1/2}$  (eq. 2), analytically (from the viewpoint of the 2PMR) this can be provided by *either* volumetric momentum loss *or* a reduction of upstream pressure (Appendix 4), or some combination.

The 2PMR predicts that there is a critical maximum target pressure  $p_{t,crit} = \frac{q_{recl}}{2\gamma c_s (T_t = \frac{E_{ion}}{\gamma})}$ . As  $f_{mom}$  is estimated as function of time using the Self-Ewald model, that also implies, we can predict a corresponding critical maximum upstream pressure ( $p_{u,crit} = p_{t,crit} / f_{mom}$ ). Using Eq. 28, we make a direct comparison between the measured (Thomson scattering)  $p_u$ , the maximum upstream pressure limit  $p_{u,crit}$  and  $p_{t,crit}$  (which, in the case of no momentum loss –  $f_{mom} = 1$ , equals  $p_{u,crit}$ ) as a function of time (Figure 20e). The measured upstream pressure rises during the density ramp, while  $p_{u,crit}$  and  $p_{t,crit}$  drop due to a decrease in  $q_{recl}$  and  $p_u$  crosses  $p_{t,crit}$  and  $p_{u,crit}$  at  $\sim 0.8$  s, the detachment threshold. After that time the target pressure limit decreases further while volumetric momentum losses start to result in a bifurcation between the upstream/target critical pressures. Despite this bifurcation,  $p_{u,crit}$  flattens and eventually rolls over, while  $p_u$  continues to track  $p_{u,crit}$ . This indicates that, even when considering the amount of observed momentum loss, the observed saturation/roll-over of the upstream pressure is *consistent* with the model.

That observation leads to three points. First it shows that the observation is consistent with the predicted maximum pressure limits by analytic theory (2PMR). Secondly, it shows that more momentum losses with a fixed  $q_{recl}$  and  $E_{ion}$ , which result in a larger bifurcation between the upstream/target pressure limits, would either enable higher upstream pressures or lower target pressures (which possibly could give access to lower temperatures  $T_t < \frac{E_{ion}}{\gamma}$  if it would enable  $p_t$  to drop faster as the temperature reduces – see A.4 and [62]). Thirdly – the most important point – it shows that given the TCV observations of  $q_{recl}$ ,  $f_{mom}$  and  $E_{ion}$ , volumetric momentum losses by itself are insufficient to reduce the target pressure to  $p_{t,crit}$  and in addition to this a saturation or roll-over of the upstream pressure is required – *consistent* with the notion from [9, 12, 13] that a lack of volumetric momentum loss may influence the upstream pressure. Although upstream pressure loss is a clear observation on TCV and needs to be accounted for, this *consistency* does not indicate

*causation*: e.g. it does not show that inadequate momentum loss on a given flux tube *causes* the upstream pressure to drop. For instance, other processes (i.e. cross-field transport (particles and/or momentum)) may be reducing the upstream pressure as well. A commonly held assumption is that the upstream pressure remains constant/unaffected by detachment, resulting in the (mis)understanding that *all* the required  $p_t$  drop *must* be provided by *only* volumetric momentum losses. These TCV results however show that *both* an upstream pressure drop and volumetric momentum losses contribute to the required  $p_t$  drop. Accounting for upstream pressure changes is thus crucial for understanding detachment.

### 5.2.5 The role of momentum loss and upstream pressure loss in target ion current loss

As described in the introduction researchers generally look at detachment with different emphases: power/particle balance and momentum balance, which mostly focusses on volumetric momentum losses. Both viewpoints for describing detachment must be consistent with equation 2. As explained earlier, the 2PMR, which combines both points of view, predicts detachment occurs when power limitation starts ( $P_{ion} \sim \frac{1}{2} P_{recl}$ ;  $T_t \sim E_{ion}/\gamma \sim 4-6$  eV), which corresponds to the point where the ion target current increases slower than  $1/T_t^{0.5}$ , hence *requiring* a target pressure loss. Thus, both target pressure loss and power limitation are required for detachment when the divertor is the primary source of ions.

It is striking that the temperatures ( $T_t < E_{ion}/\gamma \sim 4-6$  eV) at which target pressure loss *must* occur (2PMR), according to divertor-physics, corresponds to the temperatures at which volumetric momentum loss *can* occur, according to atomic physics. This seeming coincidence of plasma and atomic physics implies volumetric momentum loss develops when power ‘limitation’ conditions ( $P_{recl} < 2P_{ion}$ ) are reached, implying that power ‘limitation’ is a requirement for detachment for both points of view discussed.

The results of Section 5.2.4 show that the commonly held assumption that the upstream pressure remains constant/unaffected by detachment is not always true. Instead, the upstream target pressure and any volumetric momentum loss must be consistent with each other. This means the role of volumetric momentum loss can only be fully understood if all the processes influencing the upstream pressure are understood. These may be divertor, scrape-off layer and core processes. Examples could include changes in cross-field transport of energy, momentum and particles or volumetric losses within a flux tube, or both. The reality, however, is that we lack a quantitative understanding of how  $p_u$  is influenced by both the core and divertor plasma, which likely requires an integrated core-edge model. Lacking such a model prevents us from fully ascertaining the role momentum loss plays in detachment.

Nevertheless, it is unlikely that momentum losses directly reduces the ion target current during fully power-limited ( $P_{recl} \sim P_{ion}$ ) detachment as  $I_t \sim P_{recl}/E_{ion}$  (section 5.1) for those conditions: momentum losses slow down the fluid velocity in a flux tube, but do not directly reduce the ion flux through the tube. Momentum losses may, however facilitate detachment indirectly by allowing higher upstream pressures, leading to higher divertor densities (for the same  $T_e$ ) and thus higher divertor radiation and higher recombination rates.

## 5.3 Investigating additional ion sources and sinks

Although the ionisation source and the volumetric recombination sink within the divertor are sufficient to explain, within uncertainties, the target ion flux trend (section 4.2), additional ion sources and sinks may remain significant.

### 5.3.1 Contribution due to flows from the SOL into the outer divertor

In this work we have assumed that ion sources outside the divertor, leading to ion flows into the divertor ( $I_{up}$ ), can be neglected. While direct measurements of ion flows into the divertor are unavailable, we can estimate such flows through Eq. 28, in which  $M_u$  is the upstream Mach number and  $r$  the radial distance from the separatrix [74], which includes fluid flows along the magnetic field but ignores several types of drift flows such as ExB flows and ignores ionisation in the SOL outside of the spectroscopic view.

$$I_{up} \approx 2 \pi M_u \frac{B_p}{B_t} \int_{separatrix}^{wall} r n_u(r) \sqrt{\frac{T_u(r)}{m_i}} dr \quad (28)$$

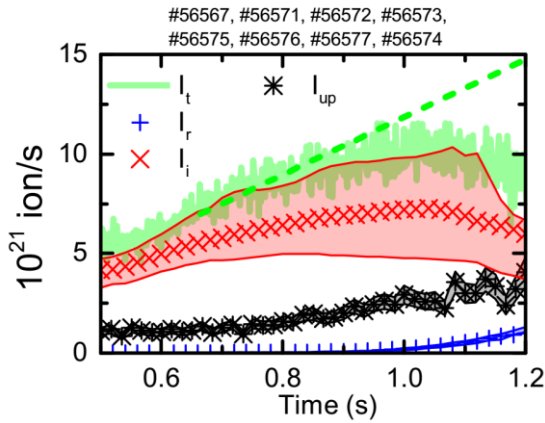


Figure 21: The target ion flux compared to the ion source, inferred ion flow from the SOL and the recombination rate.

~30% of the ion (outer) target flux and ion source.

This overall particle balance (Eq. 29) would be consistent with the addition of our estimated  $I_{up}$  within uncertainties. Even with  $I_{up}$  included, the ion source,  $I_i$ , remains the largest contributor to the target ion flux and its roll-over at the detachment onset. Based on the measurements shown in section 4.1; it is likely that this is the case also for lower current (e.g. lower density) discharges.

$$I_t = I_{up} + I_i - I_r \quad (29)$$

### 5.3.2 Evidence of molecular reactions which may be contributing to ion source or sinks during detachment on TCv

When we inferred the divertor ion sources and sinks from atomic processes, we ignored a second set of sources and sinks involving molecules - MAR (Molecular Activated Recombination) [22] and MAI (Molecular-Activated Ionization). A detailed analysis of the  $D_\alpha$  brightness measured spectroscopically in TCv and comparisons with SOLPS-ITER simulations [27] indicates that atomic processes alone do not explain the  $D_\alpha$  brightness (but do explain the brightness of other Balmer lines) and it is likely that molecular reactions are responsible. The elevated  $D_\alpha$  (with respect to the other Balmer lines) are thought to be due to the occurrence of MAR, following other works [75-77].

We estimate the enhancement of  $D_\alpha$  by comparing the measured value of  $D_\alpha$  with that predicted from higher-n Balmer line brightnesses (n=5,6 Balmer line intensities) using the results of the Balmer line analysis presented previously (section 3). This analysis is performed for each DSS viewing chord. As discussed in section 3.1-3.2 we determine  $F_{rec}$  from the 6->2/5->2 line ratio that is then used to

determine the separate excitation and recombination contributions to the  $n=5$  ( $D_\delta$ ) Balmer line intensity. The Stark density and excitation/recombination temperatures are then utilized to determine the  $D_\alpha/D_\delta$  for the excitation and recombination components separately. Predictions of the  $D_\alpha$  intensity are then finally obtained by multiplying the excitation and recombination parts of  $D_\delta$  with their respective predicted  $D_\alpha/D_\delta$  ratios and summing the excitation and recombination contributions of the  $D_\alpha$  intensity. The statistical approach described in section 3.4 was used to estimate the most probable  $D_\alpha$  and its (68%) uncertainty margin. We note that a similar technique found consistency between the measured and predicted  $n=5-9$  Balmer line intensities.

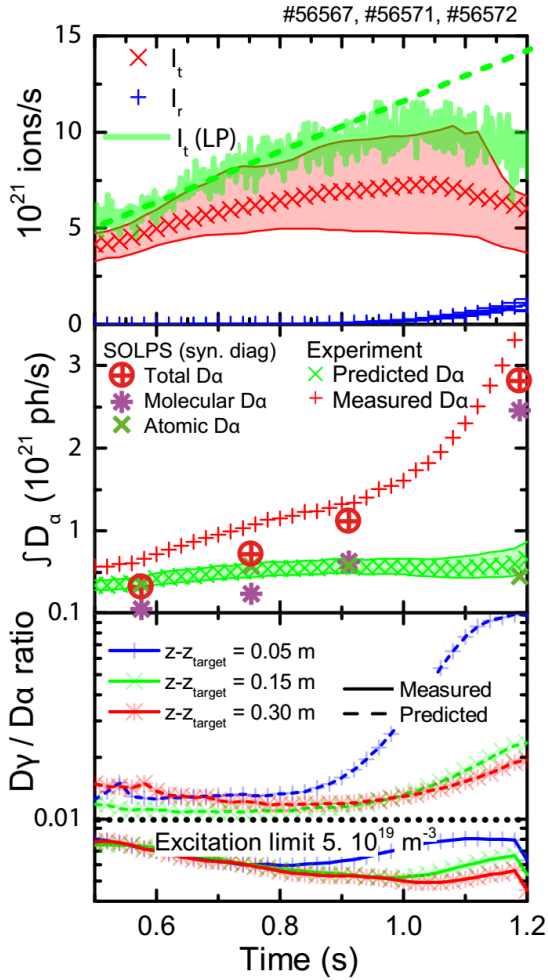


Figure 22: a) Target ion flux, ionisation rate and recombination rate as function of time. b) Measured (summed over all chords)  $D_\alpha$  signal and predicted summed  $D_\alpha$  signal, based on spectroscopic estimates. Equivalent SOLPS results, using the DSS synthetic diagnostic chords, have been added of the total  $D_\alpha$ , molecular part of  $D_\alpha$  and atomic part of  $D_\alpha$ . c) Measured and predicted  $D_\gamma/D_\alpha$  ratio along three different locations. The expected excitation limit, or minimum ratio is shown. The predicted recombination limit is  $\sim 0.1$ .

The measured  $D_\alpha$  brightness is always higher than predicted during a density scan. Figure 22 displays the measured and predicted  $D_\alpha$  brightnesses, integrated over all DSS chords (Figure 22b). The measured  $D_\alpha$  starts  $\sim 50\%$  higher than predicted and, when the core density is increased, the measured and predicted  $D_\alpha$  further diverge up to a factor three at the detachment onset and more than a factor six during the detached phase of the discharge.

We have also compared the measured  $D_\gamma/D_\alpha$  ratios with predictions based on *atomic* collisional radiative modelling alone. As highlighted in section 3.1, such line ratios are predicted to start at the values expected for excitation emission and then, as the plasma cools, increase towards values expected for recombination emission (which is a factor  $\sim 10$  larger than the excitation limit for the  $D_\gamma/D_\alpha$  ratio). The measured  $D_\gamma/D_\alpha$  along 3 DSS lines of sight (covering regions close to the target, middle of the divertor leg and close to the x-point) are shown in Figure 22c. It is striking that *even before detachment* all three measurements are lower than the excitation only limit (which only takes *atomic* excitation into account) as estimated from Open-ADAS [45, 46] PECs; we expect the ratio to be slightly above the excitation limit. As the plasma cools down after detachment onset *the observed  $D_\gamma/D_\alpha$  actually decreases further* – in contrast to the strong increase expected (recombination limit would be  $\sim 0.1$ ).

All these observations indicate that the  $D_\alpha$  line intensity is elevated compared to expectations based on *atomic* collisional radiative modelling alone. In other words, there must be other reactions, such as molecular ones, contributing to the  $D_\alpha$  emission.

We have used SOLPS simulations [27] to further investigate the source of the  $D_\alpha$  enhancement. Using the techniques highlighted earlier of a synthetic divertor diagnostic in SOLPS (section 4.1.2 and appendix A.1), a synthetic  $D_\alpha$  has been obtained and summed over all DSS chords, which is shown in figure 22b. Here the  $D_\alpha$  contributions have been distinguished into a molecular part (obtained through EIRENE [78]) and an atomic part (obtained through ADAS [45, 46]). It is important to note is that the SOLPS simulation uses the default set of molecular reactions (see [79], in particular table 3.2), which do not include reactions involving  $D^-$ . A good qualitative and fair quantitative agreement between both measured  $D_\alpha$ s and between the (atomic) predicted  $D_\alpha$  experimentally and the atomic part of  $D_\alpha$  obtained in the SOLPS simulations is shown. This further supports the idea that the strong rise of  $D_\alpha$  during the detached phase is due to molecular reactions.

MAR [80] has previously been shown to lead to elevated  $D_\alpha$  emission [33, 47, 75]. Generally, there are two MAR chains [80] which occur: 1) DA-MAR, which features a complex chain of reactions involving Dissociative Attachment resulting in  $D^-$ , leading to recombination [80, 81], 2) IC-MAR, which features molecular Ion Conversion (e.g. charge exchange) followed by dissociative recombination of  $H_2^+$  [80]. DA-MAR is thought to be a dominant detachment mechanism on linear devices [47] while calculations suggest they may be important for tokamak plasmas as well [81]. In other studies, IC-MAR is considered important in elevating  $D_\alpha$  in tokamaks [33, 77]. The observation that SOLPS predictions of the total and atomic part of  $D_\alpha$  emission agree with the experiment, implies that the molecular part of  $D_\alpha$  predicted by SOLPS-ITER also agrees to the experiment. As this does not include any reactions with  $D^-$ , this suggests that the observed  $D_\alpha$  emission is not due to DA-MAR, but due to IC-MAR – consistent with findings by [33, 77].

The strong enhancement in the observed  $D_\alpha$  ( $\sim 0.9$  s) over predictions from atomic processes is correlated with reaching  $T_t \sim E_{ion}/\gamma$ , as can be seen when comparing Figure 22 with Figure 16c. This indicates that the strong rise in  $D_\alpha$  is correlated with detachment during these density ramp cases. That rise of  $D_\alpha$ , indicative of MAR which involves molecular charge exchange in the divertor, also indicates that there is a significant molecular density in the TCV divertor. This supports the notion that the formation of  $D_2$  in the divertor leg, including the processes arising from plasma-molecule interaction (momentum losses, energy losses, MAR), is correlated with the onset of detachment [8, 70, 72]. Although the amount of  $D_2$  and the momentum loss originating from it cannot be quantified through our analysis of the experimental data, the SOLPS simulations indicate a rise in  $D_2$  in the divertor during detachment and a rise in momentum losses associated with plasma-molecule interactions, although this remains secondary to momentum loss arising from atomic charge exchange for similar upstream densities as reached in the experiment. Additionally, these molecule-ion collisions may also lead to an additional power sink [14], which is not separated in experimental analysis of the hydrogenic radiation in section 4.3 and thus is counted as impurity radiation (eq. 11). This is however thought to be minor [77].

A fuller experimental understanding of the role of molecular processes in interpreting  $D_\alpha$  emission would require more sophisticated analysis with a full molecular collisional radiative model such as Yacora [82], which is out of the scope of this paper. However, since the ion sources and sinks due to atomic ionization and volumetric match the measured target ion flux within uncertainties, it is likely that the sum of ion sources/sinks due to molecular reactions would not have a strong net effect on the particle source balance.

#### 5.4 Applicability of TCV results to other existing and planned tokamaks

A central focus of this paper is on the development of target ion current loss in detachment which is set in motion when the power flowing into the recycling region drops to twice the level required for



the ion source -  $q_{\text{recl}}/(E_{\text{ion}} \Gamma_t) \sim 2$ , which leads to a ‘power limitation’ of the ion source. This appears to be the main driver of the  $I_t$  roll-over on TCV, while recombination has a much smaller effect and occurs after the roll-over of  $I_t$ . Power limitation can play a role when  $I_t$  is (almost) fully delivered by the ion source (e.g. ‘high recycling’), which is verified in this paper for TCV. We cannot envision any situation in current or future tokamaks where power limitation is not needed for target ion current loss, assuming the ions arriving to the target are primarily ionised in the divertor – which is more likely true for closed divertors as for open divertors such as TCV. We say this because recombination cannot be dominant until after target ion current roll-over when  $T_t$  is significantly lower than  $E_{\text{ion}}/\gamma$ . ‘Power limitation’ ( $q_{\text{recl}}/(E_{\text{ion}} \Gamma_t) < 2$ ) thus appears to be a universal requirement to reach the conditions for both limiting the ion source and for lowering the target temperature to later (in detachment) reach conditions for significant volumetric momentum loss and recombination.

Certainly, the much higher density (and power-density) results from Alcator C-Mod [7,22,25] appear to be consistent with power limiting the ionization source, eventually resulting in the roll-over and then rising recombination. While the recombination/ionization ratio is much higher in C-Mod density ramp detachment than for TCV, recombination is not dominant over ionization until past target ion current roll-over [7]. In addition, C-Mod results with  $N_2$ -seeding to reach detachment show [7], like TCV, that recombination is strongly decreased (x10-100 drop) by the seeding. It thus seems generally true that volumetric recombination is not a requirement for (roll-over) detachment; although it (can) play a stronger role in other tokamaks, leading to larger target ion current drops relative to the peak value. Higher recombination rates at higher density machines could lead to a significant movement of the recombination and density peaks (front) at the deepest detached conditions, which remains small (at most a few cm) at TCV.

We do expect the characteristic gradient scale lengths of various quantities such as ionization, recombination and CX to be shorter (poloidal and along B) in tokamaks with higher densities and parallel power densities than for TCV. Certainly the parallel heat flux would be 100x larger in ITER than TCV leading to smaller parallel-to-B scale lengths in absolute value and relative to the divertor size  $\Delta L_{q_{\parallel}} (\Delta L_{q_{\parallel}} \sim q_{\parallel} / \Delta T$  where  $\Delta T$  is set by the impurity cooling curve,  $\sim 10$ -20 eV for carbon) [83]; this would lead to more localized impurity radiation and ionisation regions. In addition, higher density will lead to shorter CX and ionization mean free paths. The ions and neutrals will be better equilibrated affecting the transfer of momentum. Such higher divertor densities, for the same upstream conditions, may be facilitated by the planned baffle upgrade [84] of TCV.

There is another likely key change in divertor characteristics engendered by larger  $P_{\text{sep}}$  and  $q_{\parallel}$ . Intrinsic carbon radiation in TCV suffices to lower  $q_{\text{recl}}$  so that it limits the ionization source during density ramp discharges. However, as  $q_{\parallel}$  is increased, reaching  $P_{\text{recl}} \sim 2xP_{\text{ion}}$  without additional impurity seeding is correspondingly more difficult to accomplish during density ramps only [85]. That is particularly true for operation with high-Z metallic walls where we expect less intrinsic divertor radiation, adding impetus to needing seeded impurities to detach. However, given that impurity seeded TCV plasmas clearly show lower volumetric recombination (also true for JET [33] and C-Mod [7]) than for density ramp-driven detachment, the connection between seeding and recombination needs to be better understood.

## 6. Summary

Spectroscopic measurements of the TCV outer divertor plasma, combined with novel analysis techniques, has allowed us to infer the magnitude and location of various atomic processes in the divertor, in particular the ionization source. This has enabled us to fully characterize the various

power and particle sources and sinks (impurity radiation, ionisation and recombination) in the divertor plasma. These novel measurements provide an experimental verification that the ion source ( $I_i$ ) matches the ion target flux ( $I_t$ ) both before and during the drop in  $I_t$  during detachment on TCV while the recombination ion sink is relatively small or negligible. Volumetric recombination thus seems not to be a requirement for detachment. That the ion target flux is dominated by divertor ionisation is indicative of a high recycling divertor as opposed to ion flows from upstream dominating the ion sources giving rise to the target ion current.

We define the detachment threshold during density-ramp discharges as when the divertor ion source starts to deviate from its (linear) trend during the attached phase of that discharge. That linear trend has been confirmed using upstream measured parameters in combination with simplified analytic models (under which a Two Point Model which includes Recycling – ‘2PMR’ [4, 8, 9, 13, 62]) which demonstrated that the often-used degree of detachment scaling ( $\Gamma_t \propto \bar{n}_e^{-2}$ ) must be modified to account for changes in upstream parameters ( $n_e$ ,  $T_e$ ) and divertor radiation. During a core density ramp,  $P_{\text{recl}}$  continually drops due to increasing divertor impurity radiation while the power required for ionisation ( $P_{\text{ion}}$ ) rises, both due to a rise in ionisation rate (in the attached phase) and due to a rise in the energy cost of each ionisation ( $E_{\text{ion}}$ ) as the divertor cools. The deviation of the ion target flux with the attached trend is found experimentally to correspond to  $P_{\text{recl}}$  approaching  $P_{\text{ion}}$ : ( $P_{\text{recl}} \sim 2P_{\text{ion}}$ ); while the roll-over occurs closer to  $P_{\text{recl}} \sim P_{\text{ion}}$ . This suggests that  $P_{\text{recl}}$  *limits the ion source* and, through this, the target ion current. The start of detachment at  $P_{\text{recl}} \sim 2P_{\text{ion}}$  occurs before any significant levels of recombination occur. All experimental results for the discharge investigated are shown to be in fair qualitative and quantitative agreement with recent SOLPS simulations [27].

The behaviour of the target ion current,  $I_t$ , before and during detachment was compared to simple analytical models. Accounting for only power and particle balance using measurements of  $P_{\text{recl}}$ ,  $E_{\text{ion}}$ , and the target temperature ( $T_t$ ) leads to an  $I_t$  prediction in quantitative agreement with the measured  $I_t$ . It also shows that the ion source can be written as a trade-off between the maximum possible ion source ( $P_{\text{recl}}/E_{\text{ion}}$ ) and fraction of that power spent on ionisation ( $f_{\text{ion}} = P_{\text{ion}}/P_{\text{recl}}$ ), which increases with decreasing  $T_t/E_{\text{ion}}$  – the only variable of  $f_{\text{ion}}$ . The predicted  $f_{\text{ion}}$  using  $T_t/E_{\text{ion}}$  quantitatively agrees with  $f_{\text{ion}}$  obtained directly from spectroscopic measurements.

However, the ion source prediction from power and particle balance must also be consistent with momentum balance and the sheath conditions ( $p_t \propto \Gamma_t T_t^{1/2}$ ). As  $T_t/E_{\text{ion}}$  drops, a larger fraction of  $P_{\text{recl}}$  is used for ionisation and  $\Gamma_t$  increases.  $f_{\text{ion}}$  ( $T_t/E_{\text{ion}}$ ) is a crucial parameter denoting how fast  $\Gamma_t$  increases as function of  $T_t$ . Accounting for this, below the point  $T_t < E_{\text{ion}}/\gamma \sim 4\text{-}6$  eV (which corresponds also to  $f_{\text{ion}} = P_{\text{ion}}/P_{\text{recl}} \sim 0.5$ ), the ion target flux starts to rise slower than  $1/T_t^{1/2}$ , thus requiring a target pressure reduction (Eq. 2) – which is referred to as a detachment threshold [9, 13]. This threshold represents a maximum achievable target pressure ( $p_{t,\text{crit}}$ ) due to the trade-off between  $\Gamma_t$  and  $T_t$  (e.g.  $p_t \propto \Gamma_t T_t^{1/2}$ ).  $p_{t,\text{crit}}$  depends on the heat flux entering the recycling region ( $q_{\text{recl}}$ ) and  $E_{\text{ion}}$ . It can also be written as a maximum critical threshold for  $p_t/q_{\text{recl}}$  dependent on  $E_{\text{ion}}$  (or  $p_u/q_{\text{recl}}$  – assuming pressure balance [9, 13]). Quantitative agreement between all three equivalent criteria (e.g. for  $T_t$ ,  $f_{\text{ion}}$ ,  $p_u/q_{\text{recl}}$ ) and the experimentally-determined detachment onset (e.g. deviation of  $I_t$  from its linear trend) has been found. As detachment continues, a larger fraction of  $P_{\text{recl}}$  is spent on ionisation ( $f_{\text{ion}}$  increases) and thus less kinetic power is flowing to the target, resulting in a decrease of  $T_t$ . Simultaneously, the ionization source decreases (rolls-over) while the ionization region shifts away from the target, giving rise to an increase in the charge exchange to ionisation ratio near the target allowing charge exchange momentum loss. Later, at lower  $T_t$ , significant volumetric recombination can occur and the  $D_2$  content in the divertor increases (according to

simulations, in accordance with  $D_\alpha$  measurements) thus augmenting momentum loss due to ion-molecule collisions. The above picture of the available power limiting and reducing the divertor ion source and bringing on other processes necessary for detachment appears to be applicable to higher power density, higher density tokamaks; although volumetric recombination will be stronger in such devices which may enable  $I_t$  to drop faster in the deepest detached states (e.g. after the flattening and roll-over of  $I_t$ ).

It is striking that the temperatures ( $T_t < E_{ion}/\gamma \sim 4-7$  eV) at which target pressure loss *must* occur, according to just divertor-physics, corresponds to the temperatures at which volumetric momentum loss *starts to occur*, according to just atomic physics; we have experimentally confirmed both the temperature threshold and the momentum loss that starts at that time. As detachment proceeds, charge-exchange starts to dominate over ionisation (eventually reaching charge exchange to ionization ratios  $\sim 100$  near the target). Using these spectroscopically-inferred charge exchange to ionisation ratios, the amount of volumetric momentum loss ( $f_{mom}$ ) has been quantitatively estimated to start at the detachment onset and reach  $\sim 70\%$  at the deepest detached state, in agreement with direct experimental comparisons of the upstream/target pressure [68]. This is also quantitatively consistent with the observation that  $p_u/q_{recl}$  increases beyond its  $p_t/q_{recl}$  maxima during detachment – which is indicative of a bifurcation between the target/upstream pressures. In addition to charge exchange dominating over ionisation, at ( $T_t < E_{ion}/\gamma \sim 4-7$  eV)  $D_\alpha$  increases rapidly indicative of molecular reactions as opposed to atomic excitation/recombination, as indicated by our analysis and in agreement with SOLPS simulation results. This result has two implications: 1)  $D_\alpha$  (and associated ratios of other Balmer lines to  $D_\alpha$ ) are not appropriate indicators for atomic excitation nor recombination nor the ‘depth of detachment’ in detached conditions; 2) the strong  $D_\alpha$  levels are indicative of molecular activated recombination and indicate a significant presence of  $D_2$  radicals ( $D_2^+$ ), which is also involved in molecular charge exchange and may play a role in momentum loss through molecule-ion collisions.

Our measurements show that both the target (consistent with eq. 2) *and upstream* pressure roll-over concurrent with the  $I_t$  roll-over. Those measurements are consistent with the maximum predicted target pressure ( $p_{t,crit}$  dependent on  $q_{recl}$  and  $E_{ion}$ ) and the estimated  $f_{mom}$ , linking  $p_{t,crit}$  to a maximum possible upstream pressure  $p_{u,crit} = p_{t,crit}$ . A detailed comparison between  $p_u$ ,  $p_{t,crit}$  and  $p_{u,crit}$  shows that *both* the observed upstream pressure ( $p_u$ ) drop *and* the estimated volumetric momentum losses were necessary to obtain consistency with the 2PMR: the target pressure roll-over is thus *partially* facilitated by the upstream pressure roll-over in TCv. Reducing the target pressure can thus be subtler than just having volumetric momentum losses. Nevertheless, these results neither confirm nor reject the idea that the drop in the target pressure could pull down the upstream pressure since the origin of the roll-over of the upstream pressure is unknown.

## Acknowledgments

The authors would like to thank S. Krasheninnikov, D. Moulton and P. Stangeby, for discussions of the physics processes, previous work and spectroscopic techniques relevant to this paper. This work has been carried out within the framework of the EUROfusion Consortium and has received funding from the Euratom research and training programme 2014–2018 under Grant Agreement No. 633053. The views and opinions expressed herein do not necessarily reflect those of the European Commission. This work was supported in part by the Swiss National Science Foundation. The PhD research of K. Verhaegh was supported by funding from the University of York and the Swiss National Science Foundation. B. Lipschultz was funded in part by the Wolfson Foundation and UK

Royal Society through a Royal Society Wolfson Research Merit Award as well as by the RCUK Energy Programme (EPSRC grant number EP/I501045).

## A. Appendix

### A.1 Techniques for applying spectral analysis methods to synthesize diagnostic data from SOLPS simulation solutions

The experimental determination of local (density/temperature) and line-integrated quantities (ionisation rates/recombination rates/charge exchange rates/radiated hydrogenic power) in this work are obtained from the techniques highlighted in section 2, which utilise a 0D plasma slab model. However, in reality, the line of sight in the passive spectroscopy used in this study intersects regions of the plasma with varying temperature, electron density and neutral density; which could influence the Balmer line analysis significantly [76]. In addition to these line integration effects, various other assumptions (highlighted in section 2) were employed in the analysis, regarding the neutral fraction, path length and plasma purity ( $Z_{\text{eff}} = 1$ ). It was also assumed for the Stark fitting [26] that  $T_i$  (through Doppler broadening) and  $T_e$  have negligible influence on the line shape and are hence fixed at 5 eV in the Stark fit model. In this section we investigate the sensitivity of the techniques presented in section 2 to these assumptions by applying the analysis technique to synthetic diagnostic's data obtained from plasma solutions determined through SOLPS-ITER simulations [27]; SOLPS-ITER includes the use of the Eirene Monte Carlo model of neutral transport. The SOLPS simulations used here mimics a TCV L-mode density ramp [27] and include chemical sputtering of the carbon tiles to reach realistic carbon concentrations in the divertor (which have been verified with the experiment using the absolute CIII (465 nm) brightness). The upstream density in the simulations is reached through a gas puff.

#### A.1.2 Methodology

The Balmer line emission and line shape is modelled at every grid cell of the simulation. We utilise the simulated hydrogen ion density, hydrogen neutral density, electron density, electron temperature and ion temperature to obtain both the Balmer line emission and the various reaction rates (e.g. ionisation, recombination, etc.). Open-ADAS [45, 46] tables are used to utilise the same atomic data as in the analysis of experimental data and avoid any discrepancy between the atomic tables used in the synthetic analysis and the simulation. Molecular components to the Balmer line emission are neglected. The Balmer line shape is modelled using the experimentally measured instrumental function convolved with a Doppler broadening component, using the local SOLPS-simulated ion temperature, and a Stark line shape ([26] and section 2), using the local SOLPS-simulated electron densities and temperatures. The viewing cone corresponding to each synthetic DSS line of sight is discretised as multiple lines of sight whose amplitudes are governed by a spatial Gaussian function whose full-width-half-maxima correspond to the spot size's diameter. Each line of sight is discretised into multiple points. The emissivity spectra ( $\text{ph m}^{-3} \text{s}^{-1} \text{pix}^{-1}$ ) corresponding to the SOLPS-ITER grid cell in which each point is located is copied to these points. The synthetic Balmer line spectra is then obtained by integrating along the line of sight, yielding a brightness spectrum in terms of brightness ( $\text{ph m}^{-2} \text{s}^{-1} \text{pixel}^{-1}$ ). This synthetic spectrum is fitted using the same routine as the experimental data [26], yielding both the Stark broadening electron density estimate and the Balmer line intensity. For simplicity, the SOLPS-Eirene grid cells corresponding to the inner strike point have been omitted to prevent pollution in the synthetic spectra originating from the inner strike point. We note that the SOLPS solution at the inner divertor is detached while in the experiment it is attached – thus another reason not to include such emission.

In this analysis, the  $n=7$  Balmer line is used for the Stark density and the  $n=5,6$  Balmer line brightness and line ratio are used, similar to the technique used for #56567 highlighted in sections 4-5. An estimate for the path length is obtained analogous to the experiment from the simulation's target ion flux and flux surfaces (section 3.2). After employing the techniques in section 3 (including the statistical analysis and the uncertainties/assumptions listed in section A.2), estimates of  $I_L$ ,  $P_{rad,L}^{H-exc}$ ,  $CX_L$ ,  $T_e^E$ ,  $R_L$ ,  $P_{rad,L}^{H-rec}$  with 68% uncertainty margins are obtained along the outer divertor leg as shown in Figure A.1. The  $I_L$  and  $R_L$  profiles are then used to obtain  $I_i$  and  $I_r$  which are compared with the SOLPS output by summing the ionisation/recombination rates of every divertor grid cell caught in between the two outer spectroscopic lines of sight.

### A.1.2 Results

In Figure A.1 A & B, first the evolution of  $I_i$  and  $I_r$  are shown as function of upstream density for five SOLPS simulations whose data is stored as SOLPS-MDS+ data (the corresponding MDS+ shot numbers are shown in Figure A.1). As there are only five separate SOLPS runs, the techniques highlighted in section A.3 (based on the assumption of a continuous  $T_e$  decrease in the divertor) to improve the  $F_{rec}$  determination in limiting regimes ( $F_{rec}(F_{exc}) < 0.1$  – section 3.1) have not been used; as this requires a smooth evolution of the temperature in the divertor such that it can be assumed that the divertor temperatures are continuously decreasing (or at least not increasing). The obtained  $I_i$  and  $I_r$  from the synthetic diagnostic are in good agreement with the direct result from SOLPS (<5% deviation). The large rise in uncertainty in the synthetic diagnostic result for  $I_i$  in cold divertor conditions is due to  $F_{exc}$  being in a limiting regime ( $F_{exc} < 0.1$ ).

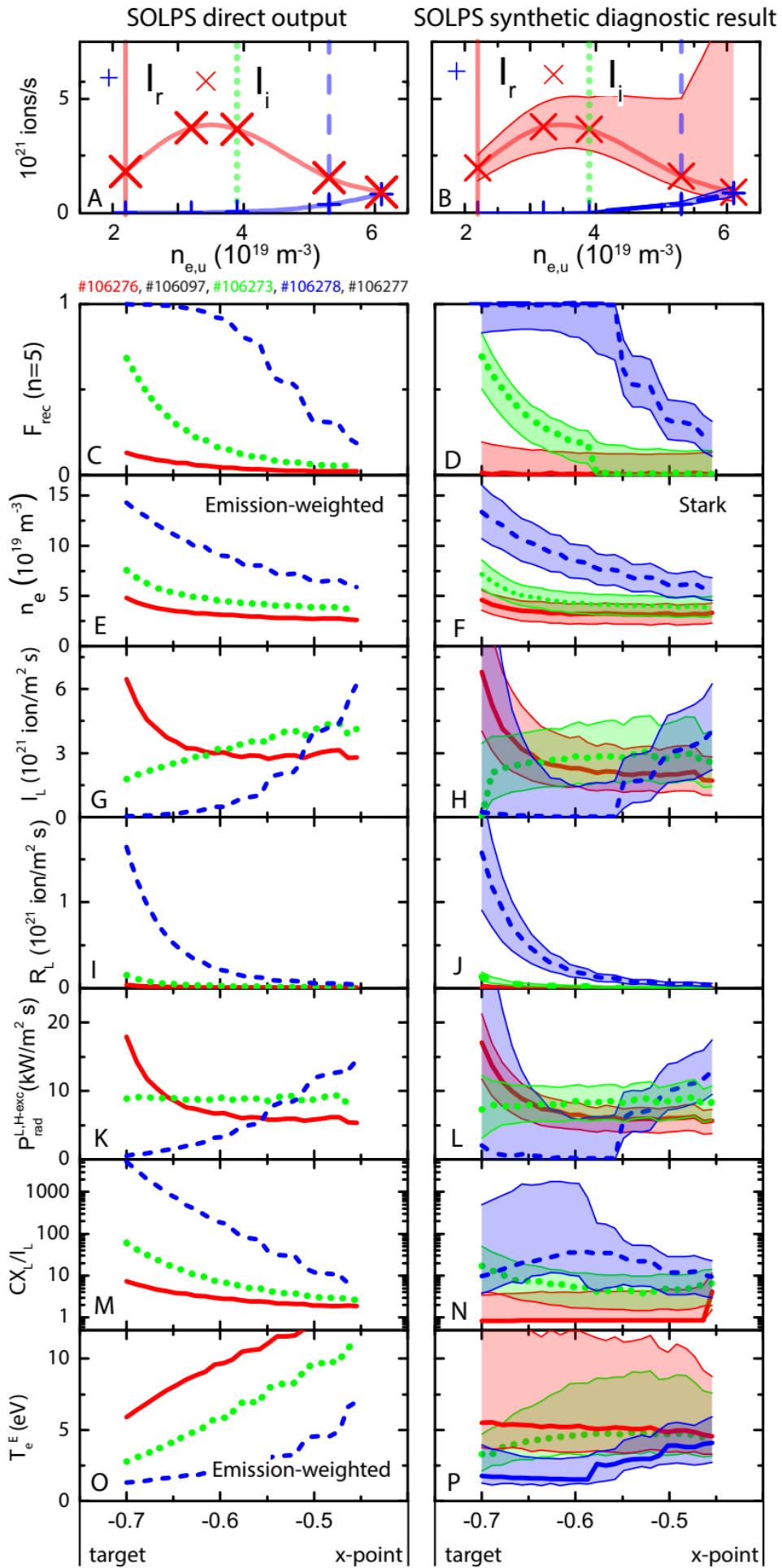
Below Figure A.1 a and b are profiles (Figure A.1 c-p) of various analysis output parameters ( $F_{rec}$  ( $n=5$ );  $n_e$ ;  $I_i$ ;  $R_L$ ;  $P_{rad,L}^{H-exc}$ ,  $CX_L/I_L$  and  $T_e^E$ ) for three different simulations whose upstream densities are indicated by the vertical lines in Figure A.1a, b). Good agreement between the synthetic diagnostic with direct SOLPS results is found for all line-integrated parameters ( $F_{rec}$  ( $n=5$ ) Figure A.1c, d;  $I_L$  Figure A.1g, h;  $R_L$  Figure A.1i, j; Figure A.1k, l) except the charge exchange to ionisation ratio ( $CX_L / I_L$  Figure A.1m, n). The deviation of the  $CX_L/I_L$  ratio and the strong increase in the  $I_L$  uncertainty near the target at the highest upstream densities occur when  $F_{exc}$  is in its limiting regime ( $F_{exc}$  ( $n=5$ )  $< 0.1$ ). As mentioned, the correction techniques for this limiting regime (A.4) could not be applied, and thus such uncertainties (which are larger than the uncertainties during the experiment) in the parameters estimated from the excitation emission can be expected. In that light, it should also be noted that the SOLPS simulations investigated (the two highest upstream density simulations) are more strongly detached than the experiment with higher recombination and lower  $F_{exc}$ .

We have also used the SOLPS model of TCV plasmas to examine whether the interpretation of local quantities (e.g. density; temperature) from chordal integrated emissivities through passive spectroscopy is reasonable; the local ('slab') quantities inferred from DSS chordal measurements are compared to the emission-weighted averaged quantities over the path length of the chord through the SOLPS grid. A good agreement between the Stark density (from the synthetic diagnostic) and the emission-weighted  $n_e$  (SOLPS) is shown (Figure A.1e, f), indicating that the Stark density from the synthetic diagnostic (or, by implication, the direct analysis of DSS data) can be interpreted as the 'characteristic density' of the emission region, which depends on the Balmer line used to obtain Stark density. There is qualitative agreement (variation with core conditions) between the inferred  $T_e^E$  from the synthetic diagnostic and the  $T_e$  respective of the excitation emission region of the 5->2 Balmer line. The reason for poor quantitative agreement is the reduced sensitivity of the  $T_e^E$  inference at larger  $T_e$ ; the magnitude of the excitation emission becomes relatively more insensitive to the electron temperature. That is also evident from examination of the PDFs obtained and presented in Figure A.2, showing a wide PDF for  $T_e^E$  at higher temperatures.

Although the local inferred quantities, based on the *total* Balmer line emission, depend on which Balmer line is used, local quantities inferred from the excitation and recombination emission *separately* are nearly identical across Balmer lines. This is because, depending on the upper quantum level, Balmer lines are either more sensitive or less sensitive to recombination. It also means that separating the excitation and recombinative emission through  $F_{rec}$  makes the analysis less sensitive to line integration effects.

In summary, we find that although several assumptions are made in the analysis; the deviation of the analysis results due to these assumptions is negligible compared to the uncertainty of the analysis. Hence, the analysis, particularly the line-integrated (such as  $I_L$ ,  $R_L$ ) and divertor-integrated (such as  $I_i$  and  $I_r$ ) ones, appears to be robust against line integration effects and assumptions regarding  $Z_{eff}$ .

*Figure A.1: Comparison between results from a synthetic diagnostic (right) on SOLPS-Eirene discharges and the direct SOLPS results (left). a, b) Volumetrically integrated ionisation and recombination rates as function of upstream density. c-p) Profiles of local and line-integrated quantities along the outer divertor leg. Line-integrated profiles: c, d)  $F_{rec}$  ( $n=5$ ). g, h) ionisation rate. i, j) recombination rate. k, l) hydrogenic radiation (excitation). m, n) charge exchange to ionisation ratio. Local quantities (note that the left-hand column are line-averaged weighted by the respective ( $n_e^{Stark} - n=7$ ;  $T_e^E - n=5$ ) Balmer line local emissivity): e, f)  $n_e$  (direct result) and Stark inference (synthetic diagnostic). o, p) excitation emission-weighted temperature (direct result) and  $T_e^E$  obtained from synthetic diagnostic analysis.*



## A.2 Details on probabilistic analysis and their output PDFs

In this section, additional technical details are provided on the probabilistic techniques presented in section 3.4.

As opposed to changing the randomisation for every different time/profile point, the randomisation is kept the same for all lines of sight and time steps. This means that, for instance, if the randomly sampled input values indicate a brightness 10% below the measured brightness, this 10% is used for all time steps and all lines of sight. Keeping the randomisation the same enables utilising the techniques from section A.3, which are employed *to each individual randomisation* in order to utilise the analysis chain in limit conditions ( $F_{rec} > 0.9$ ). This is also realistic as most of the uncertainties (such as uncertainties in the brightness and line ratio) are expected to be of a systematic nature than a random nature. At least 5000 points are used in the randomization. For each randomization separately, the toroidally integrated quantities, such as  $I_i$ ,  $I_r$ , are determined. The techniques of section 3.4 are then applied to local parameters ( $T_e^E$ ,  $T_e^R$ ), line-integrated parameters ( $I_L$ ,  $R_L$ ,  $CX_L$ ,  $CX_L/I_L$ ,  $P_{rad,L}^{H-exc}$ ,  $P_{rad,L}^{H-rec}$ ,  $F_{rec}$ ) and toroidally integrated parameters ( $I_t$ ,  $I_r$ ,  $I_{CX}$ ,  $I_{CX}/I_t$ ,  $P_{rad}^{H-exc}$ ,  $P_{rad}^{H-rec}$ ). The assumed probability density functions for each input parameter in the analysis chain is shown in Table A.1.

Table A.1: Table of used input parameters and how their input PDFs are obtained.

Input parameter	PDF	Remark
Brightness	Gaussian Peak: measured brightness Uncertainty ( $1 \sigma$ ): 17.5 %	Estimated uncertainty absolute calibration in near-UV conditions.
Line ratio	Gaussian Peak measured ratio Uncertainty ( $1 \sigma$ ): 12.5%	Estimated uncertainty relative calibration in near-UV conditions.
Electron density	Gaussian with lower cut-off through rejection-based sampling Peak: measured Stark density Uncertainty ( $1 \sigma$ ): 20% Minimum uncertainty ( $1 \sigma$ ): $1 \cdot 10^{19} \text{ m}^{-3}$ Lower cut-off: $1-5 \cdot 10^{18} \text{ m}^{-3}$	Estimated uncertainty based on: - Comparing fit results from n=6,7,9 Balmer lines - Fitting synthetic spectra with experimental-like S/N and with a randomization in $T_i$ [1-30 eV] and $T_e$ [1 – 30 eV].
Path length	Asymmetric gaussian: Peak: obtained path length Lower $\sigma$ : 50% Upper $\sigma$ : 25%	The estimated path length is determined at the target which is likely an overestimate for the pathlength higher up the divertor leg as the target measurement also picks up spreading by the divertor spreading factor varies [42, 52].
Neutral fraction	Uniform 0.001 – 0.05	Neutral fraction from modelling predictions, which have been compared with experimental data through a synthetic baratron.

Figure A.2 represents an overview of the output probability density functions (for several output parameters) obtained for #56567, which can be regarded as characteristic PDFs of the output analysis. As indicated, the magnitude of the uncertainty and its asymmetry of various analysis results can vary strongly during a density-ramp discharge. Nevertheless, the PDF of the output parameters remains unimodal, except for  $F_{rec}$  (most likely due to the techniques highlighted in section A.4). However,  $F_{rec}$  is only an intermediate result. In this work, the estimate and its uncertainty are respectively obtained from the PDF using the Maximum Likelihood Estimate (MLE) [57] and its Highest Density Interval (HDI) [57], but there are also other techniques to extract information from PDF. For example, we have compared the above techniques to taking the median value for the



estimate and the ‘equal-tail’ [57] interval (68% probability) for the uncertainty and found essentially the same result. It should also be noted that the output results will depend on the assumed input PDFs. For instance, if instead of a uniform distribution for  $n_o$  (each value within the range has equal probability) a log-uniform distribution for  $n_o$  is assumed (e.g. the probability of a value being between  $10^{-3} - 10^{-2}$  is the same as the probability of a value being between  $10^{-2} - 10^{-1}$ ), the resultant ionisation rate increases by  $\sim 20\%$ .

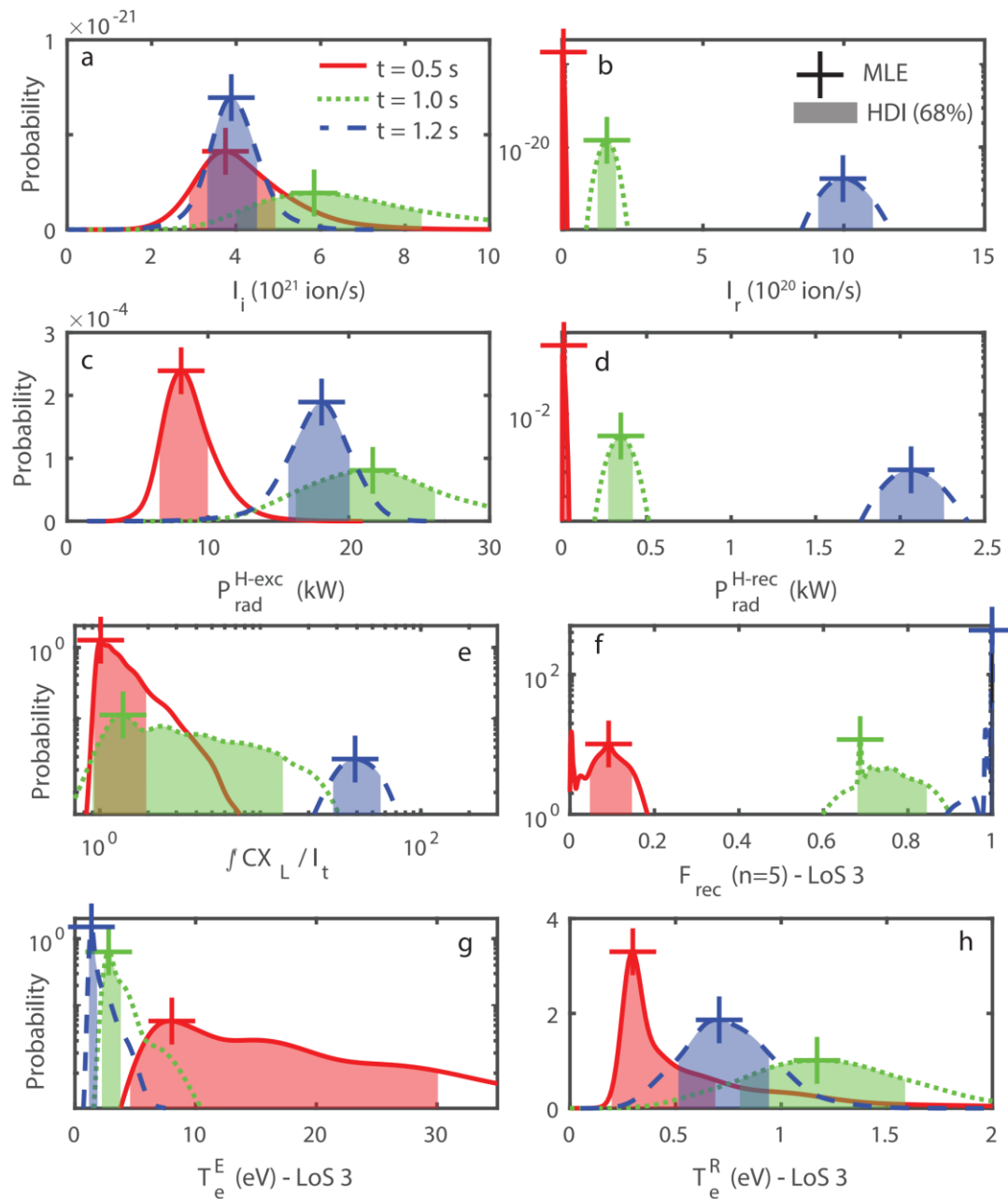


Figure A.2: Characteristic Probability Density Functions from DSS output parameters ( $I_i$ ,  $I_r$ ,  $P_{rad}^{H-exc}$ ,  $P_{rad}^{H-rec}$ ,  $F_{rec}(n=5)$ ,  $T_e^E$  and  $T_e^R$ ) taken from the analysis of #56567, together with the maximum likelihood estimate (MLE) and the highest density interval (HDI – 68%) corresponding to the  $1\sigma$  confidence interval. The results shown in figure a-e correspond to outer-divertor integrated results while the results shown in f-h (e.g. ( $F_{rec}(n=5)$ ,  $T_e^E$  and  $T_e^R$ )) correspond to inferences from the third chord closest to the target (LoS 3 – see Figure 9). The results are shown at  $t=0.5$ , 1.0 and 1.2 s.

### A.3 Further details on the $F_{rec}$ analysis

It is often experimentally observed that TCV divertor conditions can be reached where  $F_{rec}(n \geq 5)$  does reach and go beyond the quoted 0.9 limit. As  $F_{rec}$  approaches 1 the upper uncertainty bound is reduced given the limit of 1, potentially leading to an underestimation of  $F_{rec}$ . Naturally, if  $F_{rec} > 0.9$ ; even small underestimates of  $F_{rec}(n)$  can lead to a large overestimation of  $B_{n \rightarrow 2}^{exc}$ . This effect is amplified by the strong increase in the Balmer line emission (factor  $\sim 50$  [26] ( $n=6,7$ )) at detachment. In practice, the above effects can lead to unphysical results of a rapidly increasing ionisation rate if  $F_{rec} > 0.9$  during detachment.

The overestimation of  $B_{n \rightarrow 2}^{exc}$  and, through this, the ionisation rate can be addressed by utilising additional information about the electron temperature. During experiments where the divertor is continuously cooled (density/impurity ramps), one can assume that the temperature in the divertor should at least not be increasing. However, if  $B_{n \rightarrow 2}^{exc}$  is significantly overestimated in the analysis, a rising (in time) excitation temperature ( $T_e^E$ ), for a given pathlength, electron density and neutral fraction, is required for the modelled Balmer line emission (Eq. 5) to reach the experimental level. Such, unphysical behaviour of  $B_{n \rightarrow 2}^{exc}$  with corresponding increases in excitation temperature during a density/seeding ramp are unphysical. To address this, we assume that this “effective” excitation temperature is a proxy for the local electron temperatures along the line of sight integral and that  $T_e^E$  should be dropping as the divertor is continuously cooled (divertor/impurity ramps). By using smoothing and fitting techniques, the trend of each  $T_e^E$  determination as function of time for every Monte Carlo point and for every ROI is analysed and any significant  $T_e^E$  increases in the detached regime are detected. When this occurs, the corresponding Monte Carlo analysis points are removed from the analysis. From a Bayesian perspective, this is equivalent to assuming the prior that the electron temperature must be dropping during the detached regime. It is important to note is that only the *trend* of  $T_e^E$  matters for this correction procedure – not the magnitude. As the correction is applied to every Monte Carlo randomisation individually, it is not influenced by the wide PDF of  $T_e^E$  (figure A.2 g), as this wide PDF is due to systematic uncertainties – which are all fixed for the particular randomisation and chord.

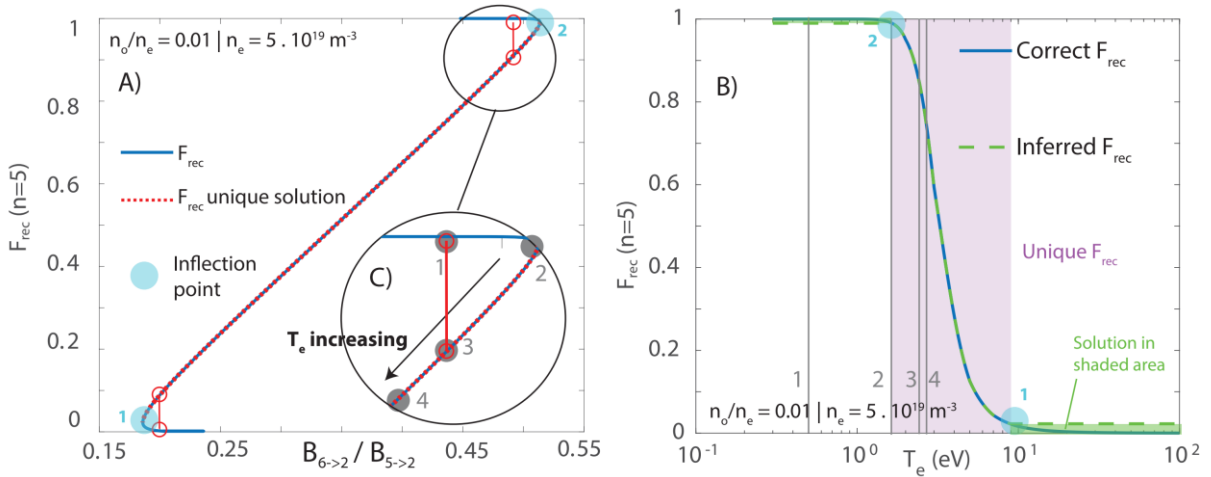


Figure A.3: An illustration of the technique for obtaining a unique  $F_{rec}$ : a) We first show the actual  $F_{rec}(n=5)$  as function of the  $B_{6 \rightarrow 2} / B_{5 \rightarrow 2}$  line ratio (labelled ‘ $F_{rec}$ ’). A second version is shown (‘ $F_{rec}$  unique solution’) which prevents non-unique solutions by limiting the used  $T_e$  window. The red line with connecting circles indicates the obtained double-valued  $F_{rec}$  of a measured line ratio outside the unique solution region. b) Comparison of the inferred  $F_{rec}$ , given a measured line ratio, as function of  $T_e$  for the 2 cases shown in Figure A.3a. c) Magnification of Figure A.3a in the  $F_{rec} \sim 1$  non-unique region where four points of  $T_e$  are highlighted, which are represented by the numbered vertical lines in Figure A.3b to link figure A.3a and A.3b.

A second issue that occurs as  $F_{rec}$  or  $F_{exc}$  approach 1 is properly determining their values from the Balmer line ratio. As illustrated in Figure 3, with accompanying discussion,  $F_{rec}$  and  $F_{exc}$ , when determined from the Balmer line ratio, are double-valued (e.g. not unique) in certain ranges of  $F_{rec}$ . These double-valued solutions correspond to a single  $B_{6\rightarrow2}/B_{5\rightarrow2}$ , but two different  $T_e$  and  $F_{rec}$ . A particular case is shown in Figure A.3a along with the corresponding  $F_{rec}$  dependence on  $T_e$  in Figure A.3b. Figure A.3c provides a magnification of the  $F_{rec} \sim 1$  region in Figure A.3a. Four points are illustrated in Figure A.3c corresponding to four values of  $T_e$  highlighted by vertical lines in Figure A.3b for the reader to help connect Figure A.3a to Figure A.3b. As the Balmer line ratio (for fixed density and neutral fraction) changes as function of dropping temperature, it transitions from being dominated by excitation (large  $F_{exc}$ , low  $F_{rec}$ ) to being dominated by recombination (large  $F_{rec}$ , low  $F_{exc}$ ). At the extremes of this temperature and  $F_{rec}$  range there is a loss of uniqueness in determining  $F_{rec}$  and  $F_{exc}$ . Two inflection points of the Balmer line ratio (e.g. a minimum and a maximum) can be identified, between which a unique solution can be obtained as indicated in figure A.3. These two points are detected experimentally. In between these two extremes, a unique value of  $F_{rec}$  is obtained. It is assumed that the temperature is continuously dropping, which means that one goes chronologically through three phases: 1) before reaching the nr. 1 inflection point (figure A.3),  $F_{rec}$  is between 0 and the value corresponding to the inflection point and is randomly chosen in this range; 2) between the nr. 1 and nr. 2 inflection points the obtained  $F_{rec}$  is unique; 3) after reaching the nr. 2 inflection point (figure A.3),  $F_{rec}$  is between the value corresponding to the inflection point and 1 and is randomly chosen in this range. This is performed for every Monte Carlo randomisation and every line of sight separately. See [62] for more details.

The techniques highlighted above have been utilised for the treatment of #56567 (since it has high recombination rates hence reaching  $F_{rec}$  ( $n=5$ ) $>0.9$ ). However, for the other discharges discussed in section 5.2, such techniques have not been used as the resulting  $F_{rec}$  values were sufficiently low.

#### A.4 Two point model with recycling energy losses

In literature [4, 9], the effect of recycling losses has been added to the Two Point model [4], which we refer to as the “2PMR”. In this section, a more explicit derivation of adding the effect of recycling energy losses to the Two Point model is provided; which has been utilised for several predictions in section 5.2.

Recycling energy losses have been included in the Two Point model by assuming that the target ion flux ( $\Gamma_t$ ), on a single flux tube, is fully determined by the ionisation source on that particular flux tube ( $\Gamma_i$ ) (Eq. A.1). As such, it is assumed that both ion flows from outside of the ionisation region towards the target and recombination in the divertor are negligible.

$$\Gamma_t = \Gamma_i \quad (\text{A.1})$$

It is further assumed that the power flux entering the recycling region ( $q_{recl}$ ) equals the kinetic part of the heat flux reaching the target  $q_t = \gamma\Gamma_i T_t$  plus the power flux spent on ionisation  $E_{ion}\Gamma_i$ , yielding a relation relating  $q_{recl}$  to  $q_t$ , where  $T_t^*$  is the ratio between energy spent on ionisation and kinetic energy reaching the target  $T_t^* = \frac{\gamma T_t}{E_{ion}}$ , as explained in section 5.1.

$$\begin{aligned} q_{recl} &= E_{ion}\Gamma_i + q_t = \gamma\Gamma_i T_t \left(1 + \frac{E_{ion}}{\gamma T_t}\right) \\ \rightarrow q_t &= q_{recl} \frac{T_t^*}{1+T_t^*} = q_{recl} f_{kin} \end{aligned} \quad (\text{A.2})$$

Using the sheath target ion flux (Eq. A.3), a relation for the target temperature as function of the heat flux reaching the target and the target pressure  $p_t$  can be established (note that  $p_t$  is the total target pressure); which is similar to the “basic” two point model result [4]. Here it is assumed that the Mach velocity near the target is 1.

$$q_t = \gamma n_t k T_t \sqrt{\frac{2T_t}{m_i}}$$

$$\rightarrow T_t = \frac{2 m_i}{\gamma^2} \left( \frac{q_t}{p_t} \right)^2 \quad (\text{A.3})$$

By combining Eq. A.3 with Eq. A.2 an implicit equation for  $T_t$  is obtained (Eq. A.4), which can be rewritten as a quadratic equation. This is valid when  $p_t$  is assumed to be a ‘static’ parameter without a specific  $T_t$  dependence, which would alter the fundamental solution structure of equation A.4. This is assumed throughout this section until further notice.

$$T_t = \frac{2 m_i}{\gamma^2} \left( \frac{q_{recl}}{p_t} \right)^2 \left( \frac{\gamma T_t}{\gamma T_t + E_{ion}} \right)^2 \quad (\text{A.4})$$

Equation A.4 forms the basis of the 2PMR and before discussing the solution of it, first we will

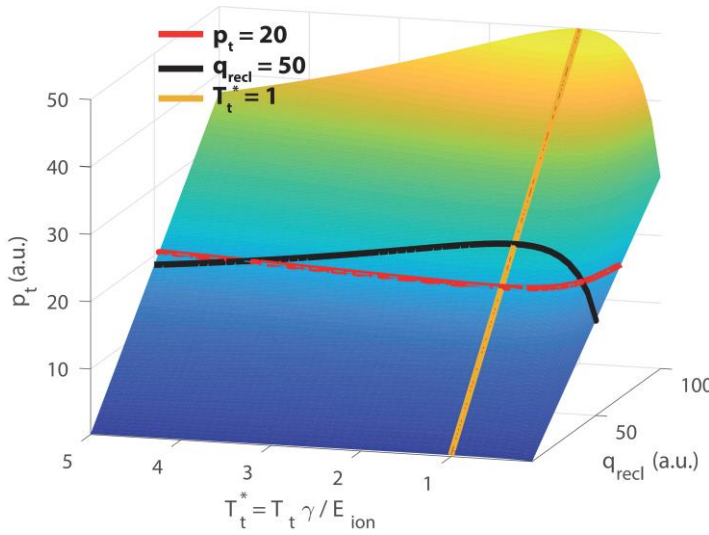


Figure A.4 Visualisation of equation A.4 as a surface plot where contour lines of the three visualised parameters are shown.

visualise (Figure A.4) how this equation relates  $p_t$ ,  $q_{recl}$  and  $T_t$  by simplifying eq. A.4 into the form  $p_t \propto \frac{q_{recl}}{T_t^{*1/2}} \frac{T_t^*}{1+T_t^*}$  where  $T_t^* = \frac{T_t \gamma}{E_{ion}}$  (here it has been assumed that  $E_{ion}$  is a fixed ‘static’ value). This shows that decreasing the temperature below  $T_t^* = 1$  (e.g.  $T_t < \frac{E_{ion}}{\gamma}$ ) requires reducing the target pressure. At that point, the target pressure (for a fixed  $q_{recl}$ ,  $E_{ion}$  –  $p_{t,crit} = q_{recl} \sqrt{\frac{m_i}{2 \gamma E_{ion}}}$ ) is maximised. Increasing  $p_t$  with a constant  $q_{recl}$  leads to a lower  $T_t$  until the maximum target pressure is reached at  $T_t = \frac{E_{ion}}{\gamma}$ . Reducing  $q_{recl}$  with a fixed  $p_t$  reduces  $T_t$  until  $T_t = \frac{E_{ion}}{\gamma}$  is reached. Here, the maximum target pressure  $p_{t,crit}$  decreases with  $q_{recl}$  until it reaches  $p_t$  at  $T_t = \frac{E_{ion}}{\gamma}$ . It is not surprising that  $p_t$  needs to drop at lower temperatures. Equation 2 dictates that  $p_t \propto \Gamma_t T_t^{1/2}$  while the speed at which  $\Gamma_t$  increases as function of  $T_t$  is dictated by  $f_{ion}$  through power/particle balance (section 5.1). Due to that specific relation, at  $T_t < \frac{E_{ion}}{\gamma}$ ,  $\Gamma_t$  increases increasingly slower as function of  $T_t$  than  $T_t^{-1/2}$  at lower – necessitating a target pressure drop, or more specifically an increasingly larger target pressure drop with  $T_t$ , as is also shown in figure A.4.

After having discussed the solution structure of A.4, we will solve this quadratic equation, resulting in a relation for  $T_t$  as function of  $\frac{q_{recl}}{p_u}$ ,  $E_{ion}$  and physical constants (Eq. A.5).

$$T_t^2 + \left( \frac{2E_{ion}}{\gamma} - \frac{2m_i}{\gamma^2} \left( \frac{q_{recl}}{p_t} \right)^2 \right) T_t + \frac{E_{ion}^2}{\gamma^2} = 0$$

$$T_t = \left( \frac{m_i}{\gamma^2} \left( \frac{q_{recl}}{p_t} \right)^2 - \frac{E_{ion}}{\gamma} \right) \pm \sqrt{\frac{m_i}{\gamma^2} \left( \frac{q_{recl}}{p_t} \right)^2 - \frac{2E_{ion}}{\gamma}} \quad (A.5)$$

Only the positive branch ( $T_t \geq \frac{E_{ion}}{\gamma}$ ) of the quadratic solution is stable (Eq. A.8) as has been explained in literature [4, 8, 9]. Hence, we assume that the negative branch  $T_t \leq \frac{E_{ion}}{\gamma}$  of Eq. A.5 cannot occur. This is however under the assumption that  $p_t$  is not a specific function of  $T_t$ . If  $p_t$  would be such a function the fundamental solution structure of A.4 would be changed, which could allow  $T_t \leq \frac{E_{ion}}{\gamma}$  if  $p_t$  decreases increasingly more as function of  $T_t$  as will be discussed later.

Using a series expansion for  $\frac{m_i}{\gamma^2} \left( \frac{q_{recl}}{p_t} \right)^2 \gg \frac{2E_{ion}}{\gamma}$  on the square root term in Eq. A.5 leads to  $T_t \approx \frac{m_i}{\gamma^2} \left( \frac{q_{recl}}{p_t} \right)^2 - 2 \frac{E_{ion}}{\gamma}$ . This indicates that the target temperature decreases for increasing  $\frac{p_t}{q_{recl}}$  until the critical point  $\frac{m_i}{\gamma^2} \left( \frac{q_{recl}}{p_t} \right)^2 - \frac{2E_{ion}}{\gamma} = 0$  is reached after which the square root term in Eq. A.5 becomes imaginary.

This implies that there is a lowest possible target temperature limit to the validity of the 2PMR, (section 5.1.2, 5.3.2). According to the used model (Eq. A.2); this limit corresponds to  $f_{ion} = f_{kin} = 0.5$ ; e.g. 50% of the power flux going into the recycling region is being used for ionisation. This limitation of the 2PMR is both highlighted by Stangeby ([4] p. 238, [8]) and Krasheninnikov [9] and corresponds to the  $p_{t,crit}$  at  $T_t^* = 1$  shown in figure A.4.

$$T_{t,crit} = \left( \frac{E_{ion}}{\gamma} \right) \quad (A.6)$$

As this critical point is related to the target pressure, it can also be written in terms of  $p_t$  (or  $p_t/q_{recl}$ ) [9], which can be written in terms of the target sound speed at the target temperature (equation A.7).

$$\frac{m_i}{e\gamma^2} \left( \frac{q_{recl}}{p_t} \right)^2 - \frac{2E_{ion}}{\gamma} = 0$$

$$\left( \frac{p_t}{q_{recl}} \right)_{crit} = \sqrt{\frac{m_i}{2E_{ion}\gamma}}$$

$$\left( \frac{p_t}{q_{recl}} \right)_{crit} = \frac{1}{\gamma c_{st}(T_t = \frac{E_{ion}}{\gamma})} \quad (A.7)^3$$

Combining Eq. A.2 and Eq. A.5 enables obtaining a relation for the target ion flux in terms of  $p_u$ ,  $q_{recl}$ ,  $E_{ion}$  and physical constants, which holds until the threshold in Eq. A.6-A.7 is reached.

$$q_{recl} = E_{ion}\Gamma_i + q_t = \gamma\Gamma_t T_t \left( 1 + \frac{E_{ion}}{\gamma T_t} \right)$$

<sup>3</sup> This critical threshold (in the form  $p_u/q_{recl}$  – this will be explained later) is twice larger than in [6]. However, the calculated threshold (Figure 20C) is  $\sim 2$  x smaller than the quoted 15 N/MW [6] likely due to different values used for  $E_{ion}$ ,  $\gamma$ . However, this point is identical to the  $p_u^2 / q_{||}$  reached in [4,8], using equations 5.37, 5.39 on p. 237, 238 with  $T_t = E_{ion} / \gamma$ .

$$\Gamma_t = \frac{q_{recl}}{\gamma T_t + E_{ion}} = \frac{q_{recl}}{\gamma \frac{2 m_i}{\gamma^2} \left(\frac{q_{recl}}{p_t}\right)^2 \left(\frac{\gamma T_t}{\gamma T_t + E_{ion}}\right)^2 E_{ion} + \gamma T_t}$$

$$\Gamma_t = \frac{\gamma p_t^2}{2 m_i q_{recl} f_{kin}(T_t)} \quad (A.8)$$

It should be noted that equation A.8 is identical to equation A.9 which is essentially the flux surface's equivalent of Eq. 18 where the 2PMR provides the  $f_{ion}(T_t, E_{ion})$  solution. Therefore, the 2PMR essentially provides a bridge between the model treated in section 5.1, based on only power and particle balance, and the Two Point model for divertor modelling.

$$q_{recl} = E_{ion} \Gamma_t + q_t = \gamma \Gamma_t T_t \left(1 + \frac{E_{ion}}{\gamma T_t}\right)$$

$$\Gamma_t = \frac{q_{recl}}{\gamma T_t + E_{ion}} = \frac{q_{recl}}{E_{ion}} \frac{E_{ion}}{E_{ion} + \gamma T_t}$$

$$\Gamma_t = \frac{q_{recl}}{E_{ion}} f_{ion}(T_t, E_{ion}) \quad (A.9)$$

For convenience, the expressions for  $f_{kin}(T_t, E_{ion})$  and  $f_{ion}(T_t, E_{ion})$  are provided in equation A.10 and A.11 respectively.

$$f_{kin}(T_t) = \frac{\gamma T_t}{E_{ion} + \gamma T_t} = \frac{\frac{m_i}{\gamma} \left(\frac{q_{recl}}{p_t}\right)^2 + \sqrt{m_i} \left(\frac{q_{recl}}{p_t}\right) \sqrt{\frac{m_i}{\gamma^2} \left(\frac{q_{recl}}{p_t}\right)^2 - \frac{2E_{ion}}{\gamma} - E_{ion}}}{\frac{m_i}{\gamma} \left(\frac{q_{recl}}{p_t}\right)^2 + \sqrt{m_i} \left(\frac{q_{recl}}{p_t}\right) \sqrt{\frac{m_i}{\gamma^2} \left(\frac{q_{recl}}{p_t}\right)^2 - \frac{2E_{ion}}{\gamma}}}$$

$$f_{kin}(T_t) = 1 - \frac{E_{ion}}{\frac{m_i}{\gamma} \left(\frac{q_{recl}}{p_t}\right)^2 + \sqrt{m_i} \left(\frac{q_{recl}}{p_t}\right) \sqrt{\frac{m_i}{\gamma^2} \left(\frac{q_{recl}}{p_t}\right)^2 - \frac{2E_{ion}}{\gamma}}} \quad (A.10)$$

$$f_{ion}(T_t) = \frac{E_{ion}}{E_{ion} + \gamma T_t} = \frac{E_{ion}}{\frac{m_i}{\gamma} \left(\frac{q_{recl}}{p_t}\right)^2 + \sqrt{m_i} \left(\frac{q_{recl}}{p_t}\right) \sqrt{\frac{m_i}{\gamma^2} \left(\frac{q_{recl}}{p_t}\right)^2 - \frac{2E_{ion}}{\gamma}}} \quad (A.11)$$

The ion current equations A.8 and A.9 do not support an ion current roll-over when decreasing  $T_t$ , as decreases in  $q_{recl}$  (or increases in  $p_u$ ) will lead to an increase in  $\Gamma_t$  due to the  $f_{ion}(T_t, E_{ion})$  dependency for the applicability regime for these equations  $T_{t,crit} > \left(\frac{E_{ion}}{\gamma}\right)$ . Therefore, the derived 2PMR above only allows attached solutions – detached solutions would require target pressure loss.

Before proceeding it is important to note that in the 2PMR only the trend of the *target pressure counts*: e.g. it does not matter whether this is reduced due to volumetric momentum losses or due to upstream pressure loss. This is a different insight compared to previous discussions in the literature [4, 8] and enables us to be more general.

However, assuming no momentum losses occur, the target pressure  $p_t$  in previous equations A.3 – A.11 can be replaced with the upstream pressure  $p_u$ , as is customary when using the Two Point model. This implies that the  $p_t/q_{recl}$  limit can be written as a  $p_u/q_{recl}$  limit [9, 13]. More generally, momentum losses will cause a bifurcation between  $p_t$  and  $p_u$ , which can be defined using a momentum loss term  $f_{mom} \equiv p_t/p_u$ , which will alter the  $p_t/q_{recl}$  limit into equation A.12. Note that, again, no specific  $T_t$  dependence of  $p_t = p_u f_{mom}$  is assumed. Due to the  $f_{mom}$  connecting  $p_t$  and  $p_u$ , equation A.12 forms a maximum upper limit the upstream pressure can form.

$$\left(\frac{p_u}{q_{recl}}\right)_{crit} = \frac{1}{f_{mom}\gamma c_{st}(T_t = \frac{E_{ion}}{\gamma})} \quad (\text{A.12})$$

Due to these target/upstream maxima a further reduction in  $q_{recl}$  when  $(p_t/q_{recl})_{crit}$  is reached must – at the very least – result in a drop of  $p_t$  to the new  $p_{t,crit} = q_{recl} \sqrt{\frac{m_i}{2\gamma E_{ion}}}$  (e.g. linearly with  $q_{recl}$ ). If *only* this drop is present, then  $T_t^*$  remains ‘stuck’ at 1 (and thus  $f_{ion} = 0.5$ ). The ion current would then reduce linearly with the reduction of  $q_{recl}$ . If the target pressure loss is stronger than the minimum drop required (e.g. stronger than linearly with  $q_{recl}$ ) – according to this model this would give access to  $T_t < \frac{E_{ion}}{\gamma}$  (see figure A.4), which would require  $p_t$  to drop faster than  $T_t^{1/2}$  in this regime. Volumetric momentum losses could possibly play a role in this if they would change the speed at which  $p_t$  drops as function of  $T_t$  [4, 8] – but that would require knowing/assuming how/whether  $p_u$  changes as function of  $T_t$ . More information of the dynamics of the 2PMR in the  $T_t < \frac{E_{ion}}{\gamma}$  regime can be found in [8, 62].

### A.5 Evaluating and applying the 2PMR model with experimental data

First, we aim to predict the *detachment onset for the flux surface corresponding to the separatrix*. This means that  $p_u$ ,  $E_{ion}$  and  $q_{recl}$  should correspond to their separatrix values, which is straightforward for  $p_u$  (obtained by Thomson scattering from the chord closest to the separatrix). However, assumptions must be made to estimate  $E_{ion}$  and  $q_{recl}$  on a particular flux surface.

As explained in sections 5.1.3 and 3.3, an estimate of  $E_{ion}$  is obtained from spectroscopic inferences, which provides an “effective”  $E_{ion}$ , which is divertor averaged over all the different flux surfaces. Such an assumption has a negligible effect on the 2PMR predicted detachment onset.

To estimate  $q_{recycl}$  at the separatrix we divide the power entering the ionisation region ( $P_{recycl}$  – section 5.3), with an effective area,  $A_{eff} = 2\pi R_{target} \frac{B_t}{B_p} \lambda_{SOL}$  [4], where it is assumed that the radial location of the ionisation region is the same as the target radius.  $A_{eff}$  depends on the ratio between the toroidal and poloidal field ( $\frac{B_t}{B_p}$ ) and a scrape-off-layer width  $\lambda_{SOL}$ . The SOL width has been approximated by using  $\lambda_{q,int}$  of the heat flux profile measured through IR imaging at the target, which has been mapped upstream [42]. The choice for a characterisation using  $\lambda_{q,int}$  for the spatial profile of  $q_{recycl}$  across flux surfaces has been made as this parametrisation is more robust during detached regimes than the Eich fit [42]. It is assumed that the spatial profile of  $q_{recl}$  is the same as that of the target heat flux, which enables extracting  $q_{recl}$  from  $P_{recl}$  using  $\lambda_{q,int}$ . Uncertainties of the characterization of  $A_{eff}$  have been neglected and could lead to systematic deviations from the portrayed trend of  $q_{recycl}$ .

Instead of estimating the detachment onset, we also wish to apply this technique to model the behaviour of the integrated ion current as function of ‘upstream’ parameters ( $p_u$ ,  $q_{recl}$ ), which can be compared with the experimentally measured integrated ion current. This requires Eq. A.8 (or A.9) to be integrated along the entire divertor floor. For the sake of simplicity, we assume that  $f_{kin}$  at the separatrix is characteristic for the entire divertor – eq. A.19. Such an assumption can be made since we are interested in comparing ion current trends (as opposed to absolute values) and, in addition, the influence of  $f_{kin}$  on Eq. A.8 is limited as  $f_{kin}$  can only vary between 0.5 and 1.

$$I_t = \int \Gamma_t$$

$$I_t \propto \frac{1}{f_{kin}} \int \frac{p_u^2}{q_{recl}} \quad (\text{A.19})$$

To simplify the expression of the integral, the upstream density and temperature profiles are broken up in their separatrix values (e.g.  $n_u^0$ ) times a function describing their profile behaviour (e.g.  $f_{n_u}(r)$ ) as shown in equation A.20.

$$\begin{aligned} n_u(r) &= f_{n_u}(r)n_u^0 \\ T_u(r) &= f_{T_u}(r)T_u^0 \\ q_{recl}(r) &= f_{q_{recl}}(r)q_{recl}^0 \end{aligned} \quad (\text{A.20})$$

To maximize temporal resolution, the upstream separatrix density/temperature are obtained from Thomson scattering, while the normalised upstream density/temperature profiles ( $f_{n_u}(r)$ ,  $f_{T_u}(r)$ ) are obtained by fitting reciprocating probe upstream density/temperature profiles, at the probe plunge times, with a double exponential:  $f_{n_u} = A_1 e^{-\frac{r-r_{sep}}{\lambda_1}} + A_2 e^{-\frac{r-r_{sep}}{\lambda_2}}$  where  $r_{sep}$  is the separatrix radius upstream. A single exponential profile using  $\lambda_{q,int}$  has been used to describe the profile of  $q_{recl}(r)$ , whose integral equals  $P_{recl}$ , again assuming  $q_{recl}$  has the same profile shape as the heat flux.

Using these profile expressions, the target ion flux can be expressed as shown in equation A.14. The modelled integrated target ion current scales as  $\frac{1}{f_{kin}}$  (evaluated at the separatrix – Eq. A.10), times  $\frac{p_u^0{}^2}{P_{recl}}$  (where  $p_u^0$  is evaluated at the separatrix) times  $f_p$ , which is a parameter describing the influence of the evolution of all spatial profiles on  $I_t$  as indicated in equation A.20, which is integrated from the separatrix until five times  $\lambda_{q,int}$  away from the separatrix.

$f_p$  outside of the reciprocating probe plunge times is interpolated by fitting a polynomial to  $f_p$  across all probe plunge times. Uncertainties in  $p_u^0$ ,  $P_{recl}$  and  $f_{kin}$  have been considered, while uncertainties in the profile description are neglected. The separatrix values of the upstream density/temperature/target temperature are referred to as  $n_u$ ,  $T_u$ ,  $T_t$  in the rest of the paper.

$$\begin{aligned} I_t &\propto \frac{1}{f_{kin}} \times f_p \times \frac{p_u^0{}^2}{P_{recl}} \\ f_p &= \int_{r_{sep}}^{\infty} \frac{f_{n_u}^2(r)f_{T_u}^2(r)}{f_{q_{recl}}(r)} dr \end{aligned} \quad (\text{A.21})$$

## References

1. Loarte, A., et al., *Chapter 4: Power and particle control*. Nuclear Fusion, 2007. **47**(6): p. S203-S263.
2. Reimold, F., et al., *Divertor studies in nitrogen induced completely detached H-modes in full tungsten ASDEX Upgrade*. Nuclear Fusion, 2015. **55**(3): p. 033004.
3. Pitcher, C.S. and P.C. Stangeby, *Experimental divertor physics*. Plasma Physics and Controlled Fusion, 1997. **39**(6): p. 779-930.
4. Stangeby, P., *The plasma boundary of magnetic fusion devices*. The Plasma Boundary of Magnetic Fusion Devices. Series: Series in Plasma Physics, ISBN: 978-0-7503-0559-4. Taylor & Francis, Edited by Peter Stangeby, vol. 7, 2000. **7**.
5. Matthews, G.F., *Plasma Detachment from Divertor Targets and Limiters*. Journal of Nuclear Materials, 1995. **220**: p. 104-116.
6. Loarte, A., et al., *Plasma detachment in JET Mark I divertor experiments*. Nuclear Fusion, 1998. **38**(3): p. 331-371.
7. Lipschultz, B., et al., *The role of particle sinks and sources in Alcator C-Mod detached divertor discharges*. Physics of Plasmas, 1999. **6**(5): p. 1907-1916.
8. Stangeby, P.C., *Basic physical processes and reduced models for plasma detachment*. Plasma Physics and Controlled Fusion, 2018. **60**(4): p. 044022.
9. Krasheninnikov, S.I., A.S. Kukushkin, and A.A. Pshenov, *Divertor plasma detachment*. Physics of Plasmas, 2016. **23**(5): p. 055602.
10. Pshenov, A.A., A.S. Kukushkin, and S.I. Krasheninnikov, *Energy balance in plasma detachment*. Nuclear Materials and Energy, 2017. **12**: p. 948-952.



11. Kukushkin, A. and H. Pacher, *The role of "momentum removal" in divertor detachment*. Contributions to Plasma Physics, 2016. **56**(6 - 8): p. 711-716.
12. Kukushkin, A., H. Pacher, and R. Pitts, *Characteristics of divertor detachment for ITER conditions*. Journal of Nuclear Materials, 2015. **463**: p. 586-590.
13. Krasheninnikov, S.I. and A.S. Kukushkin, *Physics of ultimate detachment of a tokamak divertor plasma*. Journal of Plasma Physics, 2017. **83**(5): p. 155830501.
14. Post, D.E., *A Review of Recent Developments in Atomic Processes for Divertors and Edge Plasmas*. Journal of Nuclear Materials, 1995. **220**: p. 143-157.
15. Wising, F., et al., *Simulation of plasma flux detachment in Alcator C-Mod and ITER*. Journal of nuclear materials, 1997. **241**: p. 273-277.
16. Loarte, A., *Understanding the edge physics of divertor experiments by comparison of 2D edge code calculations and experimental measurements*. Journal of Nuclear Materials, 1997. **241-243**: p. 118-134.
17. Krasheninnikov, S., et al., *Plasma recombination and molecular effects in tokamak divertors and divertor simulators*. Physics of Plasmas, 1997. **4**(5): p. 1638-1646.
18. Borrass, K., R. Schneider, and R. Farengo, *A scrape-off layer based model for Hugill-Greenwald type density limits*. Nuclear fusion, 1997. **37**(4): p. 523.
19. Pitts, R.A., et al., *Divertor geometry effects on detachment in TCV*. Journal of Nuclear Materials, 2001. **290**: p. 940-946.
20. McCracken, G.M., et al., *Evidence for volume recombination in jet detached divertor plasmas*. Nuclear Fusion, 1998. **38**(4): p. 619-629.
21. Lumma, D., J.L. Terry, and B. Lipschultz, *Radiative and three-body recombination in the Alcator C-Mod divertor*. Physics of Plasmas, 1997. **4**(7): p. 2555-2566.
22. Terry, J.L., et al., *Volume recombination and opacity in Alcator C-Mod divertor plasmas*. Physics of Plasmas, 1998. **5**(5): p. 1759-1766.
23. Wenzel, U., et al., *Volume recombination in divertor I of ASDEX Upgrade*. Nuclear Fusion, 1999. **39**(7): p. 873.
24. Lipschultz, B., et al., *Ultra-high densities and volume recombination inside the separatrix of the Alcator C-Mod tokamak*. Physical Review Letters, 1998. **81**(5): p. 1007-1010.
25. Terry, J.L., et al., *The experimental determination of the volume recombination rate in tokamak divertors*. Journal of Nuclear Materials, 1999. **266-269**: p. 30-36.
26. Verhaegh, K., et al., *Spectroscopic investigations of divertor detachment in TCV*. Nuclear Materials and Energy, 2017. **12**: p. 1112-1117.
27. Fil, A.M.D., et al., *Identification of the primary processes that lead to the drop in divertor target ion current at detachment in TCV*. Contributions to plasma physics, 2017.
28. Reimold, F., et al., *The high field side high density region in SOLPS-modeling of nitrogen-seeded H-modes in ASDEX Upgrade*. Nuclear Materials and Energy, 2017. **12**: p. 193-199.
29. Wischmeier, M., *Simulating divertor detachment in the TCV and JET tokamaks*. EPFL, 2005.
30. Pitts, R.A., et al., *Experimental investigation of the effects of neon injection in TCV*. Journal of Nuclear Materials, 1999. **266**: p. 648-653.
31. Monk, R.D., et al., *Interpretation of ion flux and electron temperature profiles at the JET divertor target during high recycling and detached discharges*. Journal of Nuclear Materials, 1997. **241-243**: p. 396-401.
32. Verhaegh, K., et al. *Spectroscopic investigation of ion sources/sinks during TCV detachment*. in *44th EPS Conference on Plasma Physics*. 2017. Belfast.
33. Lomanowski, B., et al., *Spectroscopic investigation of N<sub>2</sub> and Ne seeded induced detachment in JET ITER-like wall*. Nuclear Materials and Energy, 2018, to be submitted.
34. Coda, S., et al., *Overview of the TCV tokamak program: scientific progress and facility upgrades*. Nuclear Fusion, 2017. **57**(10): p. 102011.
35. Lomanowski, B.A., et al., *Inferring divertor plasma properties from hydrogen Balmer and Paschen series spectroscopy in JET-ILW*. Nuclear Fusion, 2015. **55**(12): p. 123028.
36. Stehlé, C. and R. Hutcheon, *Extensive tabulations of Stark broadened hydrogen line profiles*. Astronomy and Astrophysics Supplement Series, 1999. **140**(1): p. 93-97.
37. Rosato, J., Y. Marandet, and R. Stamm, *A new table of Balmer line shapes for the diagnostic of magnetic fusion plasmas*. Journal of Quantitative Spectroscopy and Radiative Transfer, 2017. **187**: p. 333-337.
38. Rosato, J., et al., *Stark broadening of Balmer lines with low and moderate quantum number in dense divertor plasmas*. Contrib. Plasma Phys., 2017.
39. Février, O., et al., *Analysis of wall-embedded Langmuir probe signals in different conditions on the Tokamak à Configuration Variable*. Rev Sci Instrum, 2018. **89**(5): p. 053502.
40. Hawke, J., et al., *Improving spatial and spectral resolution of TCV Thomson scattering*. Journal of Instrumentation, 2017. **12**(12): p. C12005.
41. Boedo, J.A., et al., *Fast scanning probe for the NSTX spherical tokamak*. Rev Sci Instrum, 2009. **80**(12): p. 123506.
42. Maurizio, R., et al. *Divertor heat flux characterisation during detachment experiments in TCV*. European Plasma Physics (45th EPS) 2017; Available from: <http://ocs.ciemat.es/EPS2017PAP/pdf/P5.116.pdf>.
43. Bernert, M. *Analysis of the H-mode density limit in the ASDEX Upgrade tokamak using bolometry*. 2013; Available from: [https://edoc.ub.uni-muenchen.de/16262/1/Bernert\\_Matthias.pdf](https://edoc.ub.uni-muenchen.de/16262/1/Bernert_Matthias.pdf).

44. Sheikh, U.A., et al., *A novel carbon coating technique for foil bolometers*. Rev Sci Instrum, 2016. **87**(11): p. 11D431.
45. OPEN-ADAS; *Open - Atomic Data Analysis Structure*. Available from: <http://open.adas.ac.uk/>.
46. Mullane, M.O. *Generalised Collisional Radiative data for hydrogen: ADAS Manual*. 2013; Available from: [http://www.adas.ac.uk/notes/adas\\_c13-01.pdf](http://www.adas.ac.uk/notes/adas_c13-01.pdf).
47. Sakamoto, M., et al., *Molecular activated recombination in divertor simulation plasma on GAMMA 10/PDX*. Nuclear Materials and Energy, 2017. **12**: p. 1004-1009.
48. Potzel, S., et al., *A new experimental classification of divertor detachment in ASDEX Upgrade*. Nuclear Fusion, 2014. **54**(1): p. 013001.
49. Ramasubramanian, N., et al., *Characterization of the island divertor plasma of W7-AS stellarator in the deeply detached state with volume recombination*. Nuclear Fusion, 2004. **44**(9): p. 992.
50. Terry, J.L. and M.L. Reinke, *Diagnostic tools for studying divertor detachment: bolometry, spectroscopy, and thermography for surface heat-flux*. Plasma Physics and Controlled Fusion, 2017. **59**(4): p. 044004.
51. Harrison, J.R., et al., *Detachment evolution on the TCV tokamak*. Nuclear Materials and Energy, 2017. **12**: p. 1071-1076.
52. Maurizio, R., et al., *Divertor power load studies for attached L-mode single-null plasmas in TCV*. Nuclear Fusion, 2017. **58**(1): p. 016052.
53. Reiter, D. and others, *The EIRENE code user manual*, in *Jülich KFA Report*. 2008, Forschungszentrum Jülich GmbH.
54. Wesson, J., *Tokamaks*. Vol. 149. 2011: Oxford University Press.
55. Botev, Z.I., J.F. Grotowski, and D.P. Kroese, *Kernel density estimation via diffusion*. The Annals of Statistics, 2010. **38**(5): p. 2916-2957.
56. Bowman, C. *Applications of Bayesian Probability Theory in Fusion Data Analysis*. 2016; Available from: <http://etheses.whiterose.ac.uk/16978/>.
57. Cowles, M.K., *Applied Bayesian statistics: with R and OpenBUGS examples*. Vol. 98. 2013: Springer Science & Business Media.
58. Theiler, C., et al., *Results from recent detachment experiments in alternative divertor configurations on TCV*. Nuclear Fusion, 2017. **57**(7): p. 072008.
59. Reimerdes, H., et al., *TCV experiments towards the development of a plasma exhaust solution*. Nuclear Fusion, 2017. **57**(12): p. 126007.
60. Batishchev, O., et al., *Kinetic effects on particle and heat fluxes in detached plasmas*. Physics of Plasmas, 1996. **3**(9): p. 3386-3396.
61. Batishchev, O., et al., *Kinetic effects in tokamak scrape-off layer plasmas*. Physics of Plasmas, 1997. **4**(5): p. 1672-1680.
62. Verhaegh, K., *Spectroscopic Investigations of detachment on TCV*, in *Physics*. 2018, submitted, University of York: York.
63. Henderson, S.S., et al., *Determination of volumetric plasma parameters from spectroscopic N II and N III line ratio measurements in the ASDEX Upgrade divertor*. Nuclear Fusion, 2018. **58**(1): p. 016047.
64. Post, D., et al., *Calculations of energy losses due to atomic processes in tokamaks with applications to the International Thermonuclear Experimental Reactor divertor*. Physics of Plasmas, 1995. **2**(6): p. 2328-2336.
65. Togo, S., et al., *Effects of neutral particles on the stability of the detachment fronts in divertor plasmas*. Plasma and Fusion Research, 2013. **8**: p. 2403096-2403096.
66. Lipschultz, B., et al., *Divertor physics research on Alcator C-Mod*. Fusion Science and Technology, 2007. **51**(3): p. 369-389.
67. Niemczewski, A., et al., *Neutral particle dynamics in the Alcator C-Mod tokamak*. Nuclear Fusion, 1997. **37**(2): p. 151.
68. Février, O., et al. *Evolution of pressure drop during detachment in the TCV tokamak*. in *APS Conference Plasma Physics*. 2017. Milwaukee.
69. Pérez, I.P., et al., *SOL parallel momentum loss in ASDEX Upgrade and comparison with SOLPS*. Nuclear Materials and Energy, 2017. **12**: p. 181-186.
70. Moulton, D., et al., *Using SOLPS to confirm the importance of total flux expansion in Super-X divertors*. Plasma Physics and Controlled Fusion, 2017. **59**(6): p. 065011.
71. Pitcher, C., et al., *The role of friction in SOL pressure balance in Alcator C-Mod*. Journal of nuclear materials, 1999. **266**: p. 1009-1014.
72. Kotov, V. and D. Reiter, *Two-point analysis of the numerical modelling of detached divertor plasmas*. Plasma physics and controlled fusion, 2009. **51**(11): p. 115002.
73. Krasheninnikov, S.I., et al., *Stability of the detachment front in a tokamak divertor*. Journal of Nuclear Materials, 1999. **266-269**(Supplement C): p. 251-257.
74. Lipschultz, B., D. Whyte, and B. LaBombard, *Comparison of particle transport in the scrape-off layer plasmas of Alcator C-Mod and DIII-D*. Plasma Physics and Controlled Fusion, 2005. **47**(10): p. 1559-1578.
75. Kubo, H., et al., *Spectroscopic study of hydrogen particle behavior in attached and detached divertor plasmas of JT-60U*. Journal of Nuclear Materials, 2005. **337**(1-3): p. 161-165.
76. Hollmann, E.M., et al., *Spectroscopic measurement of atomic and molecular deuterium fluxes in the DIII-D plasma edge*. Plasma Physics and Controlled Fusion, 2006. **48**(8): p. 1165.

77. Groth, M., et al., *EDGE2D-EIRENE predictions of molecular emission in DIII-D high-recycling divertor plasmas*. Nuclear Materials and Energy, 2018, to be submitted.
78. Reiter, D., M. Baelmans, and P. Börner, *The EIRENE and B2-EIRENE Codes*. Fusion Science and Technology, 2005. **47**(2): p. 172-186.
79. Kotov, V., D. Reiter, and A.S. Kukushkin, *Numerical study of the ITER divertor plasma with the B2-EIRENE code package*. 2007.
80. Fantz, U., et al., *Hydrogen molecules in the divertor of ASDEX Upgrade*. Journal of Nuclear Materials, 2001. **290**: p. 367-373.
81. Kukushkin, A.S., et al., *Role of molecular effects in divertor plasma recombination*. Nuclear Materials and Energy, 2017. **12**: p. 984-988.
82. Wunderlich, D. and U. Fantz, *Evaluation of State-Resolved Reaction Probabilities and Their Application in Population Models for He, H, and H<sub>2</sub>*. Atoms, 2016. **4**(4).
83. Bruce, L., I.P. Felix, and H.H. Ian, *Sensitivity of detachment extent to magnetic configuration and external parameters*. Nuclear Fusion, 2016. **56**(5): p. 056007.
84. Reimerdes, H., et al., *TCV divertor upgrade for alternative magnetic configurations*. **12**: p. 1106-1111-1106-1111.
85. Bernert, M., et al., *Power exhaust by SOL and pedestal radiation at ASDEX Upgrade and JET*. Nuclear Materials and Energy, 2017. **12**: p. 111-118.